REVIEW ARTICLE OPEN

Check for updates

Low-dimensional non-metal catalysts: principles for regulating *p*-orbital-dominated reactivity

Si Zhou[1], Wei Pei[1], Yanyan Zhao[1], Xiaowei Yang[1], Nanshu Liu[1] and Jijun Zhao [1]✉

Activation of *p*-block elements to replace the rare and precious transition metals for renewable energy applications is highly desirable. In this review, we go over recent experimental and theoretical progress on the low-dimensional non-metal materials for clean energy production, including carbon, silicon, oxide, boron, and phosphorus-based nanostructures, with the *p*-block elements serving as active sites. We aim to elucidate the mechanism for triggering activity in different kinds of non-metal systems, and extract general principles for controlling the *p*-orbital-mediated reactivity from a theoretical point of view. The perspectives and challenges for developing high-efficiency non-metal catalysts are provided in the end.

INTRODUCTION

Catalysts play a pivotal role in human society and daily life. To solve the energy and environmental crisis, a series of sustainable energy strategies have been proposed, among which the hydrogen economy is most promising and being pursued worldwide. In this energy landscape, hydrogen serves as the medium for energy production, storage, transport, and utilization, which can be implemented by converting the feedstock of water, carbon dioxide, and nitrogen from the earth's atmosphere into hydrogen fuels and valuable products via photo-/electro-chemical processes coupled to renewable energy[1]. To make this vision a reality, stable, high-efficiency, and inexpensive catalysts are indispensable. Conventional catalysts are mainly based on the transition metal elements, which have the combination of empty and filled *d* orbitals with flexible oxidation states and coordination patterns, and thus are suited to bind and activate molecules and chemical species. Subject to the Sabatier principle, moderate binding strength between catalyst and adsorbate is required for an efficient catalytic cycle[2]. Quite often, such optimal adsorption properties can only be provided by noble metals, which are scarce and expensive for commercial uses. This prompts great interest in exploiting the main group elements to replace transition metal elements in catalytic applications[3].

The light *p*-block elements with natural abundance and low toxicity are attractive candidates for catalysts design. Organic molecules, consisting of main-group elements such as carbon, oxygen, nitrogen, sulfur, or phosphorus, form a large category of metal-free catalysts. Multitudes of cheap and stable organocatalysts have been designed to drive a huge variety of chemical reactions and even to produce asymmetric molecules, rendering these main group species with a significant impact on the pharmaceutical research[4,5]. Two pioneer scientists in organocatalysis, Benjamin List and David MacMillan, are awarded the Nobel Prize in Chemistry 2021 for their development of asymmetric organocatalysis (https://www.nobelprize.org/prizes/chemistry/).

The *p*-block elements can also form a myriad of elementary and compound forms of inorganic materials with diverse composi- tions, structures, and physicochemical properties. Compared with transition metal elements, the *p*-block elements lack electronic

flexibility and are more addicted to certain oxidation states, which may endow the *p*-block materials with outstanding stability but high inertness. Strategies such as heteroatom doping, defect engineering, chemical functionalization, material hybridization, and nanostructuring offer a wealth of opportunities for activating *p*-block materials[6–8]. In particular, lowering the material's dimen- sionality can give rise to exotic electronic structures, together with large surface areas and high atom utilization efficiency, which are advantageous for energy conversion and storage. Zero- dimensional (0D) clusters, one-dimensional (1D) nanotubes and nanowires, and two-dimensional (2D) materials composed of *p*- block elements have been widely obtained in the laboratory[9–12]. With definite structures, these *p*-block nanomaterials provide an ideal platform to explore new reaction mechanisms associated with *p* orbitals, understand the relationship between geometrical structure, bonding character, electronic structure, and reactivity of non-metals, as well as perform the proof-of-concept studies.

During the past decade, breakthroughs have been made in the development of non-metal catalysts for renewable energy applications[13]. Among them, carbon-based materials, such as defective or heteroatom-doped graphene and carbon nanotubes, are mostly adopted for water electrolysis, fuel cells, and metal–air batteries[8]. Two-dimensional semiconductors like g-C_3N_4 and phosphorene are suitable photocatalysts for solar energy conver- sion[13–15]. Non-metal single-atom catalysts exhibiting unique activity for certain reactions, such as dispersed B atoms on substrates, have also been reported in the experiment[16]. Transition metal chalcogenides in diverse nanostructured forms as well as 2D transition metal dichalcogenides (TMDs) are among the most promising electrocatalysts, in which the chalcogen atoms have been shown to exhibit intrinsic bifunctional activity for hydrogen evolution reaction and oxygen evolution reaction[17–19]. In addition, Sn, In, and Bi-based electrocatalysts with unique selectivity are obtained in laboratory[20,21]. Such success demonstrates the great promise of *p*-block nanomaterials as substitutes of noble metal catalysts for green energy production. In the meantime, extensive theoretical efforts have been devoted to identifying the active sites and reaction pathways in these new catalysts and to find the descriptors of activity. However, compared with transition metal- based materials, for which the *d* band theory is widely utilized for

---

[1]Key Laboratory of Materials Modification by Laser, Ion and Electron Beams (Dalian University of Technology), Ministry of Education, Dalian 116024, China. ✉email: zhaojj@dlut.edu.cn

explaining their trend of activity[22–24], the regulatory rule of non-metals' activity is much less understood. The large discrepancies among different p-block elements make it challenging to establish a general picture for the design principles of non-metal catalysts for various reactions.

In this article, we present an overview of the latest advances in the experimental and theoretical explorations of non-metal catalysts for energy conversion—the clean energy reactions pivot in hydrogen economy, such as oxygen evolution reaction (OER), oxygen reduction reaction (ORR), hydrogen evolution reaction (HER), carbon dioxide reduction (CO_2RR), and nitrogen reduction reaction (NRR) driven by sustainable energies. Water splitting is the most effective route to produce hydrogen fuels via:

$$2H_2O \rightarrow O_2 + 2H_2 \tag{1}$$

For the electro(photo)chemically driven processes in the aqueous condition, water splitting comprises two half-reactions—HER at the cathode and OER at the anode following the formulas below:

$$2H^+ + 2e \rightarrow H_2 \tag{2}$$

$$2H_2O \rightarrow O_2 + 4H^+ + 4e \tag{3}$$
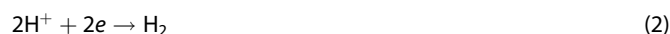
where the acidic reaction condition is considered as an example, while water splitting in the alkaline media and even neutral water is also possible[25]. The reverse of OER is ORR, which is a central reaction in fuel cells and rechargeable metal–air batteries[26]. With the hydrogen sources, CO_2 and N_2 reduction can proceed through

$$xCO_2 + y(H^+ + e) \rightarrow product + zH_2O \tag{4}$$

$$N_2 + 6H^+ + 6e \rightarrow 2NH_3 \tag{5}$$
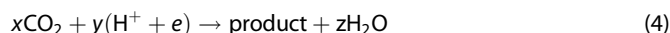
in which hydrocarbon fuels and alcohols with high energy density can be directly produced by CO_2RR. Value-added chemicals, such as ethylene and propylene as the most important chemicals for petrochemical industry, ammonia (NH_3) as the essential source of fertilizers, can also be obtained by selective reduction of CO_2 and N_2 gases, respectively.

Theoretical characterization of an electro(photo)catalyst's activity is mainly based on the free energy curves calculated within the standard hydrogen electrode model[27,28]. The overpotential or limiting potential (sometimes also defined as onset potential) is the key parameter for evaluating the activity of electro(photo) catalysts in aqueous solution from the thermodynamic point of view, which can be calculated from the maximum Gibbs free energy of formation among the reaction steps[27,29,30]. As thermal catalysis is mostly adopted for industrial CO_2 conversion and ammonia synthesis[31,32], some essential works involving thermal-driven CO_2 and N_2 hydrogenation by non-metal catalysts are also discussed in this article. The mechanisms of the above chemical reactions as well as the experimental and theoretical methods for characterizing the performance of different types of catalysts have been introduced by many literature[1,33–35], and thus will not be described in details here.

Herein we mainly focus on carbon, silicon, oxide, boron, and phosphorous-based catalysts in various structural forms from single atoms, clusters, nanotubes, 2D nanosheets, bulk crystals, to their heterostructures. We are interested in the situations where C, Si, O, B, and P atoms serve as the active sites, and the mechanisms and feasible strategies for activating these p-block elements in different nanostructures and bonding environments are discussed. Since there are many reviews on these material systems from the experimental aspect[36–38], in this article we will emphasize the role of first-principles calculations on the atomistic understanding of the p-orbital-dominated catalysis and the underlying structure-activity relationships, and disclose the cooperation between theory and experiment to advance the precise design of new catalysts with ultrahigh efficiency. Particularly, a simple and

physical framework named as the "p band model" is proposed to illuminate the principles for modulating the activity of non-metal-based catalysts akin to the d band theory for transition metals. This model picture is found to be valid for various low-dimensional materials, such as graphene, silicene, 2D metal oxides, boron nitride nanotubes and nanocages, and phosphorene by proper modification. There are also other materials with the p-block elements playing an important role in catalysis, such as transition metal chalcogenides and carbides, and 2D TMDs and MXenes. The governing rules for their activity have been discussed in somewhere else[39–43], and thus will not be covered by this article. We end this review by providing the prospects in the challenges and research directions for future development of renewable energy materials using the abundant p-block elements.

CARBON-BASED CATALYSTS

With advantages of extensive source and low price, diverse and controllable architectures, superior chemical and thermal stabilities, excellent electrical conductivity, carbon materials form a major category of non-metal catalysts for many chemical reactions. However, pure carbon materials are usually non-active or exhibit much inferior catalytic performance in comparison with transition metal-based materials. Fortunately, heteroatom doping and defect engineering can trigger activity in the graphitic carbon materials, such as carbon fullerenes and nanocages, carbon nanotubes, and graphene, which have been widely adopted for electrocatalysis of oxygen and hydrogen reactions[44,45]. For reduction of the highly stable molecules like CO_2 and N_2, doping transition metal atoms or decorating with dispersed metal atoms or nanoparticles in the carbon materials would be necessary. The transition metal–nitrogen–carbon (M–N–C) materials and metal-organic frameworks (MOFs) are demonstrated with superior activity for electrochemical CO_2RR, which have been described in many literature[46–49]. Besides, 2D porous carbon nitride and boron carbon nitrides are potential photocatalysts owing to their suitable band gap and outstanding light harvesting capability. Howbeit, modification of these semiconductors or adding co-catalyst is required to create the active sites[50]. Since we are interested in the p-orbital-dominated catalysis, in this section we will focus on those carbon systems with C atoms as the active sites.

Heteroatom-doped graphitic carbon materials

The explosive exploration of high-performance electrocatalysts based on carbon materials can date back to Dai's pioneering work on nitrogen-doped carbon nanotubes (NCNTs) in 2009[51]. Dai et al. synthesized vertically aligned NCNTs for electrocatalysis of ORR in alkaline media, which exhibit a much better electrocatalytic activity, long-term operation stability, and tolerance to crossover effect than the commercial Pt/C catalyst. Density functional theory (DFT) calculations using the B3LYP hybrid functional revealed a substantially high positive charge density on the C atoms adjacent to N dopants that have strong electronic affinity. The O_2 molecule chemisorbs on such C active sites in a side-on configuration, which effectively weakens the O–O bonding and thus facilitates ORR at the NCNTs electrode. Sooner later, N-doped graphene materials have also been demonstrated as metal-free electrocatalysts for ORR in both acid and alkaline medium[52,53].

Theoretical efforts have been devoted to unveiling the origin of activity of heteroatom-doped graphene for electrochemical ORR. Zhang et al. suggested that the active sites in N-doped graphene depend on not only charge distribution but also spin density distribution[54]. Based on cluster models of graphene terminated by H atoms, they showed that N doping introduces unpaired electrons to the graphene sheet, resulting in asymmetry spin density and charge density. The OOH* species strongly binds with

the C atoms having either high spin density or high positive charge density, while it cannot adsorb on pure graphene sheet. Yu et al. investigated the full reaction path of ORR on graphene doped by graphitic N atoms by considering the solvent effect and coverage of oxygen intermediates on the surface[55]. Their DFT calculations showed that O_2 adsorption is significantly enhanced in the aqueous environment due to hydrogen bonding with water. ORR occurs via a four-electron pathway in alkaline medium, which involves protonation of the chemisorbed O_2^* species, while dissociation of O_2 molecule is unlikely and requires a large kinetic barrier of 1.56 eV. The rate-determining step of ORR is the removal of OH* intermediates from the graphitic sheet involving a kinetic barrier of 0.78 eV. A comparison between the activities of B, N, and P doped graphene for ORR in the acid condition was carried out by Del Cueto et al.[56]. Their DFT calculations demonstrated that P-doping endows the neighboring C sites with stronger binding capability with OOH* species and the reduction reaction is energetically more favorable than that on N- or B-doped graphene.

Bifunctional electrochemical activity for both ORR and OER was achieved by a mesoporous carbon foam co-doped with N and P atoms synthesized by Zhang et al.[57]. The samples comprise a large number of edge-like graphitic structures, which play a crucial role in the catalytic activity. Theoretical analysis further revealed that for both ORR and OER, the reaction centers are located near the edges of graphitic sheet, but at different distances from the edges. Under the four-electron pathway, the singly N-doped graphene yields the lowest overpotential of 0.44 V for ORR, with formation of OOH* species being the rate-determining step. For OER, the edge C sites in the N, P co-doped graphene have the lowest overpotential of 0.39 V. These two values are even lower than those of the benchmark catalysts ~0.45 V for ORR on Pt and ~0.42 V for OER on RuO_2 calculated using the same method. Li et al. performed a DFT study to gain deeper insights into the bifunctional activity of N-doped graphene modeled by nanoribbons[58]. They found the lowest overpotentials of 0.40 V and 0.44 V for electrochemical OER and ORR in the armchair nanoribbons, respectively. The active site for OER is the C atom adjacent to N dopant and in the interior of graphene nanoribbon, while ORR occurs at the edge C atom adjacent to N atoms. Bader charge analysis revealed the redistribution of surface charge in graphene lattice induced by N doping and edge effect. The positively charged C atoms would facilitate the adsorption of reaction intermediates with negative charges; on the other hand, moderate adsorption strength is required to achieve high electrocatalytic activity.

In the synthetic N-doped graphitic carbon materials, N dopants are present in different configurations, such as graphitic, pyridinic, and pyrrolic N atoms in the carbon lattice. It is interesting to ask where is the active site and whether the N doped configuration has any effect on the catalytic activity of graphitic surface. Qiao et al. reported a B, N co-doped graphene for electrocatalytic ORR in an alkaline medium with synergistic enhancement of activity compared with singly B- or N-doped graphene[59]. Their DFT calculations identified a B–C–N heteroring, in which N plays the role of electron-withdrawing group to indirectly activate B atom through electron transfer with the C atom between them. The B atom near a pyridinic N atom gains more extra electrons than that near a graphitic N atom, and generally shows higher reactivity with OOH* intermediate. For a more direct comparison, Nakamura et al. prepared four model catalysts for electrocatalytic ORR in acid condition based on pyridinic N-dominated, graphitic N-dominated, edge-patterned, and clean highly oriented pyrolytic graphite (HOPG)[60]. They showed that the ORR active sites are created by pyridinic N atoms. After examining CO_2 adsorption behavior, they found that acidic CO_2 molecule adsorbs only on the pyridinic N-dominated HOPG catalyst, demonstrating that

pyridinic N endows the neighboring C atoms with Lewis basicity and thus the activity for O_2 chemisorption.

Furthermore, Jiao et al. proposed a molecular orbital concept to understand the trend of activity of graphene materials doped by various heteroatoms for electrocatalytic ORR[61]. They prepared a series of singly doped graphene samples with different non-metal elements (B, N, P, O, S). The ORR performance was evaluated in terms of exchange current density, onset potential, reaction pathway selectivity, and kinetic current density. These four descriptors measured by experiment are in good agreement with DFT calculations, both revealing that the trend of activity follows B > N > P > O > S for different heteroatom-doped graphene samples (Fig. 1a, b). Their DFT calculations showed that the four descriptors for electrocatalytic activity are well related to the binding strength of oxygenated intermediates on the graphitic surface. To further explore the relationship between oxygen binding strength and the electronic structure of doped graphene catalysts, the authors examined the valence orbital level of the active sites (either heteroatoms or adjacent C atoms) by natural bond order analysis of the cluster models of graphene. They defined a parameter E_{diff} as the difference between the lowest valence orbital energy of the active center and the highest valence orbital energy of the entire graphene cluster to quantitatively represent the valence orbital level. It turns out that the free adsorption energy of reaction intermediates follows a linear relationship with E_{diff} for various active sites of the doped graphene sheets. Such behavior is similar to the transition metal catalysts, whose activity is correlated to the d-band center. The underlying principle can be understood as that the valence orbital (v) of active sites hybridizes with the bonding (σ) orbital of adsorbates to form bonding (v-σ) and antibonding (v-σ)* states (Fig. 1c). As the (v-σ) state is fully occupied for the doped graphene sheets, the filling degree of (v-σ)* state depends on the valence orbital levels of the active sites. A higher valence orbital level leads to decreased filling of the antibonding (v-σ)* state, thereby stabilizing adsorbates on the graphitic surface. In this manner, this theoretical model helps disclose the fundamental rule for regulating the binding strength of reaction intermediates on heteroatom-doped graphene electrocatalysts at the level of molecular orbitals.

The linear relationship between activity and the valence orbital level of reaction centers has also been validated for HER electrocatalysis in heteroatom-doped graphene[62]. Zheng et al. carried out DFT calculations on the free adsorption energy for H* species (ΔG_{H^*}) on graphene doped by non-metal heteroatoms. They focused on N and P doped graphene, as N and P have different electron negativities and result in contrast differences in charge population at the adjacent C atom, which is the active site for HER electrocatalysis. The co-doping of N and P atoms into graphene matrix may enable maximal activation of the adjacent C atom by tailoring its electron donor–acceptor property and consequently optimize its HER activity. The ΔG_{H^*} values of the singly and co-doped graphene sheets show a linear trend with E_{diff}. In particular, H* binding is notably strengthened on graphene upon N and/or P incorporation. Pyridinic N and P co-doping yields the highest value of E_{diff}, corresponding to the lowest value of $\Delta G_{H^*} = -0.08$ eV, signifying its highest HER activity with the most favorable H* adsorption–desorption property. These theoretical predictions were then verified by synthetic N and/or P doped graphene samples, among which the co-doped system indeed exhibits enhanced HER activity compared with the singly doped samples. More encouragingly, these graphene-based catalysts show favorable HER activity in a wide range of pH values, in contrast to traditional metallic and nanostructured MoS_2 electrocatalysts, which are active under either acidic or basic conditions.

To design high-performance electrocatalysts for HER, Jiao et al. elucidated the principle for electronic structure engineering of graphene by dual heteroatom doping to optimize its HER
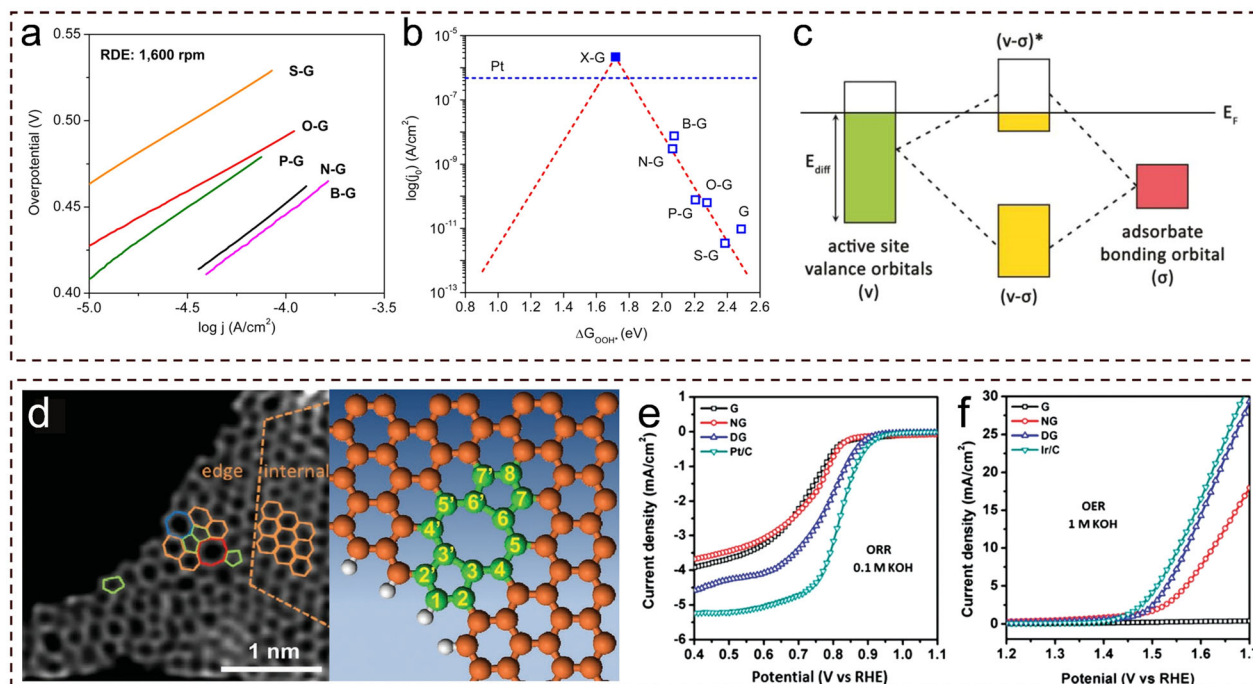
Fig. 1 HER, ORR, and OER performance of graphene-based materials. a Tafel plots and b volcano plot between $j_{\text{theory } 0}$ and $\Delta G_{\text{OOH*}}$ for different heteroatom-doped graphene catalysts. c Scheme of orbital hybridization of valence band from active sites and adsorbates bonding orbital. E_F refers to highest valence orbital energy of the entire graphene cluster (a–c are reproduced with permission from ref. [61], Copyright© American Chemical Society 2014). d HAADF image (left) and simulation model (right) of defective graphene. Linear sweeping voltammetry curves of the pristine, N-doped, and defective graphene for e ORR and f OER (d–f are reproduced with permission from ref. [68], Copyright© WILEY-VCH 2016).

performance[63]. They considered five kinds of heteroatoms (B, N, O, P, S) to substitute either edge or central C atoms in the graphene matrix. DFT calculations unveiled that the H* binding strength generally follows the sequence of B > N > O > S > P for the doped graphene, and the most active sites are the non-edge C sites. The $\Delta G_{\text{H*}}$ values are linearly correlated to the highest peak of density of states (DOS) of the active center (E_p). Similar to the relation between activity and valence orbital level described above, a higher location of E_p corresponds to higher level of antibonding states with a lower occupancy, and thus results in stronger interaction between adsorbate and catalyst surface. To further optimize $\Delta G_{\text{H*}}$, the authors considered dual doping of graphene by N and another element (B, P, S) in various doping patterns. Dual doping indeed leads to the change of DOS of active C atoms and thus modulates the binding strength of H* species. In particular, N and S co-doped graphene exhibits the highest activity with $\Delta G_{\text{H*}} = 0.23$ eV, in comparison with $\Delta G_{\text{H*}} = 0.81$, 0.53, and 1.10 eV for singly N-doped, N and P co-doped, N and B co-doped graphene systems, respectively. Following these theoretical results, proof-of-concept experiment was carried out by preparing various dual doped graphene samples. The measured trend of HER activity agrees well with the prediction that S or P co-doping with N endows graphene with enhanced activity relative to singly N doping, while N and B co-doping yields lowest HER activity for the graphene-based sample. The success of developing high-performance graphene-based electrocatalysts with the guidance of DFT modeling demonstrates the predictive capability of first-principles calculations. The proposed descriptors and electronic structure-activity relationship would allow precise design of doped carbon materials for various energy conversion processes.

Defective graphitic carbon materials

Since the activity of heteroatom-doped graphitic carbon materials originates from the charge redistribution and modification of local electronic structure, it is natural to ask whether defects can trigger any activity. Point and line defects, such as vacancies, dislocations, and grain boundaries, are inevitable in the synthetic graphitic carbon materials. They can also be created by post-synthesis treatment such as plasma or chemical etching, and removing heteroatom dopants from carbon matrix by thermal treatment. In principle, C atoms at the defective regions have unsaturated bonding configurations and thus may become reactive.

To clarify this issue, Zhao et al. considered a divacancy in graphene comprising two pentagons and one octagonal (denoted as "585 defect") for ORR electrocatalysis using DFT calculations[64]. The limiting step of ORR was found to be the protonation of O_2 to OOH* intermediates, involving a Gibbs free energy of formation $\Delta G = 0.41$ eV, much lower than that of pristine graphene ($\Delta G = 0.88$ eV) and N-doped graphene ($\Delta G = 1.03$ eV). As a proof of concept, the authors synthesized N-doped and defective graphitic carbon materials by heat treatment of an N-enriched porous organic framework material (PAF-40). By heating at different temperatures, N atoms would be released, leaving vacancies in the carbon lattice. It was shown that the carbon sample with extremely low N content (0.21 at.%) has excellent ORR activity (comparable to benchmark Pt/C catalyst) and better durability as well as methanol tolerance. Therefore, it is reasonable to hypothesize that defects play an important role in the observed high performance of such graphitic carbon-based electrocatalysts.

The ORR activity of various point and line defects in graphene has also been theoretically explored by Zhang et al.[65]. Based on the cluster models of defective graphene, the pentagon ring at the zigzag edge was found to have the activity for electrochemical ORR, while single vacancy and Stone-Wale defect are inactive. The line defects containing an odd number of heptagon or octagon carbon rings can also catalyze ORR. The activity is related to the spin density or high charge density at the C atoms in the defective regions. Later, there are more experimental reports on the high

electrochemical activity of defective carbon materials. For instance, Jiang et al. fabricated defective carbon nanocages using in situ MgO template method with benzene as the precursor, which present abundant holes, edges, and positive topological disclinations[66]. These defective carbon nanocages exhibit good ORR performance with a high onset potential of ~0.11 V versus the normal hydrogen electrode (NHE) in the alkaline medium. Tang et al. observed high bifunctional activity for ORR and OER in the N-doped and edge-rich graphene materials by direct carbonization of sticky rice as carbon precursor[67]. In both studies, DFT calculations demonstrated that the pentagon rings and edges in graphene have unique activity for oxygen reactions.

To directly identify the defect type, Jia et al. adopted high-resolution transmission electron microscopy (HRTEM) and observed a variety of defects including pentagons, heptagons, and octagons in the graphene samples obtained via a facile N removal procedure from a N-doped precursor (Fig. 1d)[68]. The defective graphene exhibits trifunctional activity for ORR, OER, and HER electrocatalysis, and the corresponding activities are all much better than those of N-doped graphene (Fig. 1e, f). Then DFT calculations were performed by considering the observed defect rings, i.e., edge pentagon, 585, 7557, and 5775 defects. The edge pentagon was predicted to be the most active site for ORR and OER with Gibbs free energy of formation $\Delta G = 0.47$ and 0.94 eV, respectively, while 7557 defect exhibits the highest activity for HER with $\Delta G_{H*} = -0.19$ eV. These combined experimental and theoretical results manifest that defects in the graphitic carbon materials can induce electrocatalytic activity for oxygen and hydrogen reactions.

The unique activity of pentagon defect has been confirmed by Jia et al., who synthesized HOPG with specific edged pentagon defects by controllable doping and removal of pyridinic N atoms from the HOPG sample[69]. The specific pentagon defects are directly identified by the high-angle annular dark-field scanning transmission electron microscopy (HAADF-STEM). It was observed that N dopants at the edge sites are in the form of pyridinic configuration. After high-temperature treatment, N atoms are removed from the graphene edges, and the remaining dangling bonds of C atoms are reconstructed to form pentagon ring at the edges. Work-function analyses coupled with macro and micro-electrochemical performance measurements suggested that the pentagon defects in HOPG are the major active sites for ORR in the acidic condition, which are much superior to the pyridinic N sites in N-doped HOPG. Consistent results were also given by DFT calculations, which predicted higher ORR activity for the graphene model with edge pentagon defect than that of the N-doped model.

More evidence on the electrochemical activity of pentagon defect was provided by the experiment performed by Zhu et al.[70]. They cut C_{60} fullerene into fragments with in situ alkaline etching strategy and obtained a pentagon-defect-rich carbon nanomaterial. The aberration-corrected scanning transmission electron microscopy (ac-STEM) showed the resulting sample has a three-dimensional porous carbon structure with vast structural defects. Pentagons as well as common hexagons in the carbon framework are evident in the ac-STEM images. Such unique structure results in enormous promotion of ORR activity and supercapacitor performance with excellent long-term stability. Combined with N doping, the ORR activity can be further enhanced to compete with the commercial Pt/C catalysts. The dominant role of pentagon defects on the profound electrochemical properties was confirmed by comparing with the defective graphene sample containing only holes, edges, and pore structure.

The above experimental results demonstrate the possibility of defect engineering of graphitic carbon materials for improving their electrochemical performance. These studies also arouse the attention for reconsidering the relative importance of heteroatom doping and structural defects to the activity, and shed light on

synergizing both factors for designing high-efficiency electro-catalysts for various energy conversion processes.

Besides the clarification of active sites in defective carbon materials, Tao et al. explored the relationship between surface charge and activity in defective HOPG[71]. Argon plasma was applied to irradiate the HOPG surface to create defects, inducing localization of surface charge onto defective active sites as characterized by scanning ion conductance microscopy (SICM) and Kelvin probe force microscopy (KPFM). The electrocatalytic activities for ORR, OER and HER can be enhanced by the increased defects and surface charge. DFT calculations showed a typical volcano plot curve between the onset potential (exchange current) and the charge of active C atoms. No doubt, these results provide a new perspective to tailor the activity of graphitic carbon materials by charging active sites via defect engineering.

Hybrid catalysts of graphitic carbon and transition metal-based materials

The graphitic carbon-based materials by proper modification can possess high activity; however, they usually work in the alkaline condition. More often, these metal-free electrocatalysts suffer from low activity and/or poor stability in the acidic medium. For some energy conversion processes such as water electrolysis and fuel cells, electrocatalysts under the acidic environment is more desirable owing to their better performance and fewer unfavorable reactions[72,73].

Regarding this issue, Deng et al. raised a concept of encapsulating nonprecious metals by carbon shell to resist the harsh condition. They synthesized a peapod-like structure consisting of carbon nanotubes shelling Fe nanoparticles, in which each compartment of carbon nanotubes (CNTs) containing one or two Fe particles and the graphitic wall ranges between 1 and 8 layers[74]. Such chainmail nanostructures exhibit high resistance to oxidation and corrosion by the acidic medium. Intriguingly, the protection by CNTs does not suppress the activity; instead, this hybrid electrocatalyst exhibits a high activity for ORR with long-term stability in the acidic environment. According to the DFT calculations, electrons penetrate through the carbon shell from the encapsulated metals to promote ORR on the outmost CNTs surfaces. Due to the interaction from the encapsulated Fe particles, the DOS from the p orbitals of C atoms near the Fermi level is increased and the work function of carbon surface is decreased by about 0.5 eV, which are expected to enhance the surface reactivity. Consistently, O_2 molecule can readily adsorb on the chainmail structure with an adsorption free energy of 0.03 eV, which is much less than that on pristine CNTs (1.43 eV). Doping N atoms in CNTs leads to further increase of the DOS at the Fermi level and the adsorption free energy of O_2 is lowered to -0.44 eV, suggesting the strengthened binding of O_2 on nanotube surface and thus higher ORR activity upon N doping and Fe particle encapsulation.

In the successive series of studies, Deng and co-workers fabricated various chainmail electrocatalysts for oxygen and hydrogen reactions using carbon nanotubes or graphene sheets to encapsulate transition metal or alloyed nanoparticles, and aimed to clarify how the type of metal element, N doping in the graphitic lattice, and number of carbon layers affect the electrocatalytic activity[75–77]. In particular, they prepared a hierarchical architecture consisting of ultrathin graphene shells (with only 1 to 3 layers) encapsulating a uniform CoNi nanoalloy, and achieved outstanding HER performance in the acidic medium[78]. DFT calculations revealed that increasing the amount of N dopants and reducing the number of graphene layers can significantly increase the electron density on graphene surface and enhance the H* binding as well as HER activity. Specifically, enclosing a metal cluster by monolayer graphene lowers ΔG_{H*} by 0.8 eV, whereas the change in ΔG_{H*} significantly drops to about

0.1 eV when the cluster is covered by three graphene layers. Thus, the carbon layer thickness has substantial impact on the activity of such chainmail catalysts, i.e., thinner graphitic shell yields higher activity. Besides, Deng and co-workers also synthesized single-layer graphene encapsulating various 3d transition metals, including Fe, Co, Ni, and their alloys. The FeNi alloy embedded in graphene was found to have the best activity and high durability for OER in the acidic medium, even superior to the commercial IrO$_2$ catalyst[79].

Later, vast core-shell structures have been developed in the experiment, and the embedded materials in the carbon shells included transition metals, transition metal carbides, nitrides to phosphides. For instance, encapsulated Co, NiCu, CoP, Ni$_2$P, and MoN nanoparticles have been reported for HER electrocatalysis[80–85]. The encapsulated noble metal nanoparticles (Pd, Pt, Ru, and Au) and Fe$_3$C-Fe hybrids were adopted for OER and ORR, respectively[86,87]. Bifunctional and multifunctional electrocatalysts have also been achieved, such as encapsulated Fe$_3$C-Co hybrids for ORR, OER, and HER[88], and encapsulated FeCoNi ternary alloy for overall water splitting[89]. Relevant theoretical modeling revealed the occurrence of electron transfer between the metal core and carbon shell, which enables modulation of activity of the carbon surface.

Despite of the aforementioned success, a deeper understanding of the interplay between metal filler, N dopant, and carbon shell is still lacking. The basic rules for choosing proper metal element and heteroatom dopant to precisely tune the catalytic performance of these core-shell nanostructures are highly desirable. To address these issues, Zhou et al. carried out a series of theoretical studies on the heterostructures of N-doped graphene covering various transition metals and transition metal compounds for electrocatalysis (Fig. 2a). They predicted that N-doped graphene on Co(111) and Fe(110) surfaces exhibit bifunctional activity for ORR and OER with overpotentials as low as 0.37 V, even better than the benchmark Pt and RuO$_2$ catalysts (Fig. 2c)[90]. The surface C atoms have different activities, depending on their relative positions to the underlying metal surface as well as the N dopant in graphene. For instance, the most active sites for ORR on N-doped graphene supported on Co(111) are the C atoms next to the pyridinic N dopant, and those for OER are the C atoms in the hollow site with respect to Co surface and meanwhile near the N dopants. A simple theoretical picture was proposed to understand the synergistic effect in such heterostructures: the interlayer charge transfer from transition metal surfaces and intralayer charge redistribution in the graphitic sheet induced by N dopants break the π conjugation of carbon network. As a consequence, the p$_z$ orbitals of C atoms are partially occupied and thus become reactive, with activity correlated to the local charge density, which are in turn mediated by the interlayer and intralayer charge transfer (Fig. 2b).

On the experimental aspect, Co and Fe metals encapsulated by carbon shells have been demonstrated to be highly active for ORR and OER electrocatalysis. Liu et al. prepared hybrid carbon nanocages with inner shell of N-doped microporous carbon, and the outer shell dominating the activity is N-doped mesoporous graphitic carbon encapsulating Co nanoparticles[91]. As an electrocatalyst, such double-shell nanocages exhibit superior activity and durability for both ORR and OER in comparison with Pt and RuO$_2$ catalysts, and hold potential as a bifunctional electrode for rechargeable Zn–air batteries. Yu et al. fabricated N-doped carbon nanotubes embedding Fe nanorods as cathode catalyst for rechargeable Li–O$_2$ batteries[92]. They showed that incorporation of Fe nanorods inside CNTs greatly enhances the reversibility and activity toward Li–O$_2$ reaction, which indicates their suitable reactivity with O$_2$ molecule. The experimental results corroborate the theoretical model considered for the core-shell structures of transition metals and graphitic carbon materials, and verify the computational scheme for describing the electrocatalytic properties of these hybrid nanostructures.

To unveil the principles for precisely tailoring the electrochemical activity of core-shell structures of graphitic carbon materials and transition metal-based materials, Zhou and co-workers systematically explored the HER activity of N-doped graphene on various material surfaces, including transition metals Co and Fe, transition metal oxides Co$_3$O$_4$ and Fe$_3$O$_4$, and transition metal carbides TiC, WC, and VC[93]. The graphitic sheets on Co, Fe, WC, and VC substrates exhibited suitable ΔG$_{H^*}$ values of –0.02–0.13 eV for HER, quite competitive to Pt(111) (ΔG$_{H^*}$ = –0.10 eV). The impact of different transition metals or compounds on the electronic structures of carbon shell lies in the modification of the energy levels and occupancies of p$_z$ orbitals of the C atoms, which can be reflected by the p$_z$ band center (ε$_{pz}$) defined as

$$\varepsilon_{pz} = \int ED(E)dE \Big/ \int D(E)dE \tag{6}$$

where D(E) is the density of states from p$_z$ orbitals of the surface C atoms at a given energy E; the integral is taken for all occupied states (Fig. 2d). As displayed by Fig. 2f, ΔG$_{H^*}$ follows a linear relationship with ε$_{pz}$ for all the considered graphene-based heterostructures, with lower ε$_{pz}$ (relative to the Fermi level) corresponding to stronger H* binding. This trend of activity is opposite to the d band theory for transition metal catalysts[23] as well as the valence orbital theory proposed for heteroatom-doped graphene[61] discussed in the section "Heteroatom-doped graphitic carbon materials". Such discrepancy can be ascribed to the fact that for the present graphene-based heterostructures, the antibonding states are almost fully occupied, as evident from the few electron states available in the conduction bands (Fig. 2e). In this case, the stability of bond formation can be understood by the extended Hückel theory[94]. The valence orbital levels of the graphitic sheet (referred to the vacuum level) determine the off-diagonal Hamiltonian matrix element H$_{\mu\nu}$ that is correlated to the bonding strength with adsorbate. The deeper center of the C p$_z$ bands, the lower H$_{\mu\nu}$ and thus stronger binding with the reaction intermediates. This established electronic structure-activity relationship, namely "p band model", explains the trend of activity for the graphitic carbon hybrid electrocatalysts from the level of electronic band structures.

The "p band model" has also been verified for the heterostructures of N-doped graphene and MXenes[95]. Zhou et al. predicted that the bare surfaces of V$_2$C and Mo$_2$C MXenes coupling with N-doped graphene can endow bifunctional activity for ORR and HER electrocatalysis on the graphitic sheet. MXenes with distinct work functions exhibit different coupling strengths with the graphitic sheet, resulting in differences in the band shift of the graphitic sheet. Consequently, the binding energies of adsorbates on the graphene/MXene heterostructures follow a linear relationship with not only ε$_{pz}$ but also the work function of MXene (Fig. 2i). N-doped graphene supported by MXene with a larger work function has a lower ε$_{pz}$ and stronger binding capability with adsorbates. This provides a new descriptor, which can be directly measured and modulated in the experiment to tune the C p$_z$ band center and ultimately optimize the surface reactivity for the graphitic carbon-based hybrid electrocatalysts. Moreover, oxygen reduction can proceed via dual pathways of O$_2$ → OOH* and O$_2$ → 2 O* involving kinetic barriers as low as 0.20 eV (Fig. 2g, h), demonstrating both favorable thermodynamics and fast kinetics of ORR on the graphene/MXene heterostructures.

The above theoretical picture has been supported by experiment. Wu et al. designed a HER electrocatalyst in full pH range by few graphitic carbon layers wrapping Co$_x$Mo$_{2−x}$C particles supported on MXene 2D sheets[96]. With proper Co substitution (x = 0.31) in Mo$_2$C, HER performance of the hybrid system is greatly enhanced. DFT calculations suggested that Co doping increases the work function of Mo$_2$C and leads to more optimal H* binding strength on the carbon shell, which is consistent with the
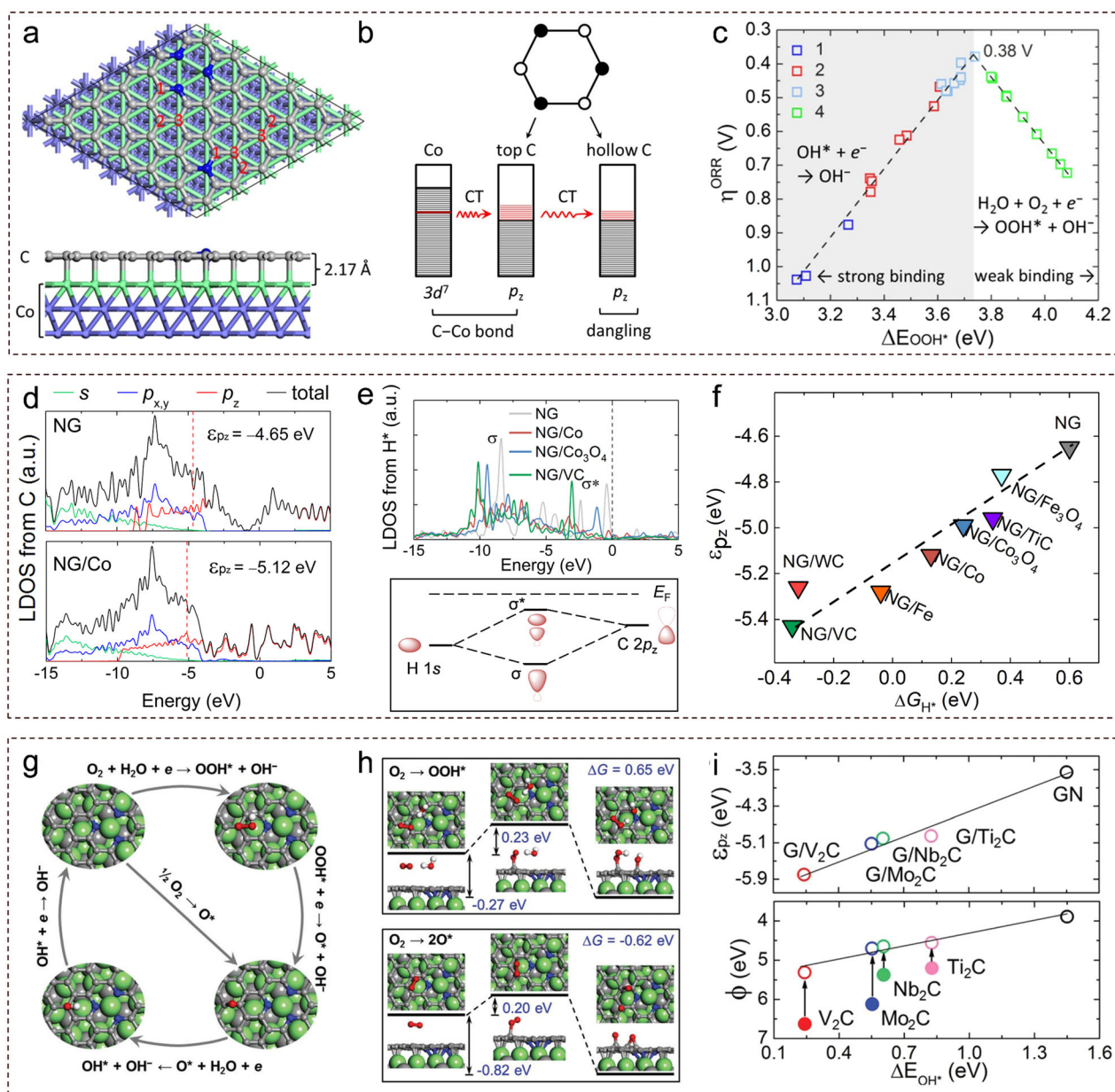
Fig. 2 Active origins of N-doped graphitic carbon/transition metal hybrid materials. a Model structures and **b** schematic illustration of charge transfer of N-doped graphene (NG) on Co(111) substrate. **c** Volcano plots of ORR overpotential vs binding energy of OOH* on various sites of NG on Fe(110) substrate in alkaline media (**a–c** are reproduced with permission from ref. [90], Copyright© American Chemical Society 2017). **d** Local density of states (LDOS) of C atoms in freestanding NG, and the NG/Co hybrid system. **e** LDOS of a H atom adsorbed on the most active site of NG and the NG/metal hybrid system (upper panel). Schematic illustration of formation of H–C bonds for the NG/metal hybrid system (bottom panel). **f** The C p_z band center as a function of the lowest ΔG_{H^*} value (**d–f** are reproduced with permission from ref. [93], Copyright© Elsevier Ltd. 2018). **g** Dual reaction pathways of ORR on NG supported on the V_2C MXene monolayer. **h** Kinetic barriers and transition states (middle panel) for O_2 dissociation via two reaction pathways. **i** The p_z band center (top panel) and work function (bottom panel) as a function of the lowest binding energies of OH* species for various graphene/MXene heterostructures (**g–i** are reproduced with permission from ref. [95], Copyright© The Royal Society of Chemistry 2018).

experimental ultraviolet photoelectron spectrometer (UPS) measurement.

To summarize this section, encouraging progress has been made in utilizing graphitic carbon-based materials as electro-catalysts for water electrolysis, fuel cells, and metal–air batteries with outstanding stabilities. The C atoms can be activated by proper heteroatom doping, defect engineering, or charge transfer with transition metals or transition metal compounds through interfacial coupling. Analogous to the d orbitals of transition metals catalysts, the p_z orbitals of the activated C atoms with broken π conjugation are partially filled, whose energy levels and

occupancy govern the activity. The established electronic structure-activity relationships provide useful guidance to tailor the catalytic performance of not only graphitic carbon-based materials, but also other non-metal materials, as will be discussed in the following sections.

SILICON-BASED CATALYSTS

Silicon as a naturally abundant semiconducting material has long been pursued for solar energy conversion owing to its superior electronic and optical properties. Crystalline silicon remains the

material of choice for solar cells. Moreover, silicon nanostructures in various forms, such as nanosheets, nanowires, and quantum dots, are commonly adopted as photoelectrode in the photoelectrochemical cells for energy and environmental applications[97]. However, silicon itself usually lacks catalytic activity, such that elemental doping or addition of co-catalysts is necessary to achieve high efficiency for the photo- or electro-chemical processes. Nevertheless, direct usage of silicon-based nanomaterials for catalytic reactions is possible by proper modification. The underlying mechanism for activation of silicon and the principle for tuning its activity may be distinct from those of carbon-based materials. In this section, we will focus on silicon nanowires (SiNWs), silicon hydrides, and 2D elementary and compound forms of silicon, which have been demonstrated or proposed to possess intrinsic activity for water splitting and CO_2 reduction with the p states of surface Si atoms governing the activity.

Silicon nanostructures for water splitting

Silicon nanowires have been widely used for solar energy conversion, owing to their outstanding photoelectronic properties, easy synthesis, and morphology control[98]. They can absorb a large portion of sunlight from ultraviolet to visible (UV-vis) and near infrared (IR) regimes, and exhibit a broad visible emission centered near the red-infrared wavelength, indicating the sufficient energy of excitons generated in SiNWs to drive many photoelectrochemical reactions[99]. The vertically aligned SiNWs arrays, which can be facilely obtained in laboratory, are favorable configuration for photoelectrodes, as they not only allow for enhanced light absorption through multiple scattering, but also enable radial charge carrier collection[100]. So far, H_2 production by water splitting and CO_2 reduction to certain products through photo(electro)catalysis on SiNWs has been realized in the experiment; however, the performance is either unsatisfactory or degrades rapidly[101–104]. More often, transition metal dopants or co-catalysts are required to enhance the photoelectrochemical performance of SiNWs[105–109]. Compared with carbon-based nanomaterials, the intrinsic activity of SiNWs is seldom addressed due to their more complex surface chemistry. As a result, the catalytic mechanism for various chemical reactions and the regulatory rule for controlling the chemical reactivity of SiNWs remain largely elusive.

Using DFT calculations, Zhang et al. investigated the electronic band structures of SiNWs[110]. They considered SiNWs with (100), (111), and (112) surfaces terminated by H or Cl atoms, and showed that these systems have suitable band gap of about 2.0 eV and proper band edge positions with respect to the redox potentials for photocatalysis of water splitting. Moreover, the top valence band mainly distributes on the nanowire surface especially for those with increasing coverage of Cl atoms; meanwhile the bottom conduction band resides in the interior of SiNWs, which is beneficial for electron-hole separation.

An experimental exploration of the mechanism of water splitting on SiNWs was carried out by Liu and co-workers[111]. They fabricated SiNWs from Si wafers by metal-assisted etching. During the synthesis process, hydrofluoric acid (HF) was used to remove the oxide layer to ensure clean Si surface, which inevitably leads to the formation of Si−H bonds on the nanowire surface. Fourier transform infrared (FTIR) spectroscopy confirmed the presence of both Si−H and Si−OH bonds during photocatalysis. The experimental characterization revealed that the photocatalytic activity of SiNWs dramatically decays as the reaction proceeds to the third cycle. Both Si−H and Si−OH bonds facilitate charge separation to ensure long carrier lifetime. But Si−H bonds offer high activity for H_2 production, while Si−OH bonds do not. The bare Si surface does not contribute to photocarrier separation or H_2 generation. Combining the experimental results with DFT calculations, the mechanism of water splitting on SiNWs has been decoded. The Si−OH bonds are

generated by H_2O dissociation, with the remaining H proton reacts with Si−H bonds to form H_2. The authors also used HF to treat the SiNWs surface after photocatalysis, and found that the Si−H bonds are recovered and the photocatalytic performance is significantly improved, which supports the proposed mechanism for water splitting on SiNWs.

Porous Si nanomaterials have been reported as promising photocatalysts for H_2 production[112–117]. For instance, Dai et al. developed a bottom-up synthesis strategy of mesoporous Si materials for photocatalytic H_2 production, with tunable structural characters such as surface area, pore size, and primary particle size[113]. They showed that the surface area, crystallinity, and content of surface oxides jointly affect the H_2 evolution performance of the mesoporous Si materials. By removing their surface oxide and improving crystallites at heat treatment of 600 °C, the H_2 generation rate largely increases from 191 to 882 μmol H_2 h^{-1} g^{-1} Si. Meanwhile, the small particle sizes shorten the migration distance of photogenerated carriers to the surface active sites, which is also beneficial for the photocatalytic efficiency. Ryu et al. prepared high-purity porous Si nanosheets with thickness of ~5 nm, whose morphology and activity closely depend on the reaction temperature[114]. Ultrathin Si nanosheets have a higher activity with 486 μmol H_2 h^{-1} g^{-1} Si at 650 °C, compared with 233 and 160 μmol H_2 h^{-1} g^{-1} Si at 550 and 700 °C, respectively. The high catalytic ability is attributed to the ultrathin thickness, high specific surface area, and high crystallinity, which allow easy access to the reactants and offer more active sites for effective utilization of the photo-generated charge carriers. The enlarged band gap (~1.9 eV) of the ultrathin Si nanosheets endows it with higher reduction potential for photo-reduction of H_2O molecules. Song et al. fabricated highly-crystalline mesoporous Si spheres, whose band gap is also increased (~1.84 eV) in comparison with bulk Si, thus yielding high reduction capability under visible light[116]. Moreover, the mesoporous structure enhances the multiple scattering effect and leads to strong light absorption. An excellent photocatalytic activity with H_2 evolution rate of 1785 μmol H_2 h^{-1} g^{-1} was achieved, significantly higher than that of Si nanoparticles (61 μmol H_2 h^{-1} g^{-1}). Martell et al. investigated the influence of HF etching on the photocatalytic H_2 evolution by mesoporous Si nanoparticles[117]. They showed that a lower volume (0.2 mL) of HF does not remove enough oxide contents in the porous Si nanoparticles, whereas higher volumes (>1.0 mL) introduce reaction byproducts and morphological changes, both resulting in reduced H_2 evolution rates. The highest H_2 evolution rate of ~1398 μmol h^{-1} g^{-1} was observed when 0.5 mL per 0.010 g of Si was used. All these experimental results reveal the key factors for achieving optimal photocatalytic efficiency in these silicon nanostructures.

Silicon hydrides for CO_2RR

Nanoscale silicon with surface hydrides exhibits intriguing activity for CO_2 photo(thermal)-reduction. A series of studies have been carried out by Ozin's group to explore the underlying reduction mechanism and pursue strategies to improve the activity and durability of these abundant and low-cost materials[118]. Sun et al. reported photo-conversion of CO_2 to CO by using the hydride-terminated Si nanocrystals at a rate of hundreds of μmol h^{-1} g^{-1}[119]. The Si nanocrystals were synthesized by thermal treatment of SiO in the H_2/Ar environment followed by HF treatment. The obtained Si nanocrystals have an average diameter of about 3.5 nm, and exhibit strong broad-band optical absorption with increasing absorptivity from near infrared to ultraviolet wavelength range (Fig. 3a). The FTIR spectroscopy showed plenty of Si−H bonds on the Si nanocrystals surfaces (Fig. 3b). Intriguingly, a CO production rate as high as 4.5 μmol h^{-1} g^{-1} was observed on these samples in the absence of H_2 and under an incident solar intensity of 1 sun at 150 °C, with the rate decreasing in the
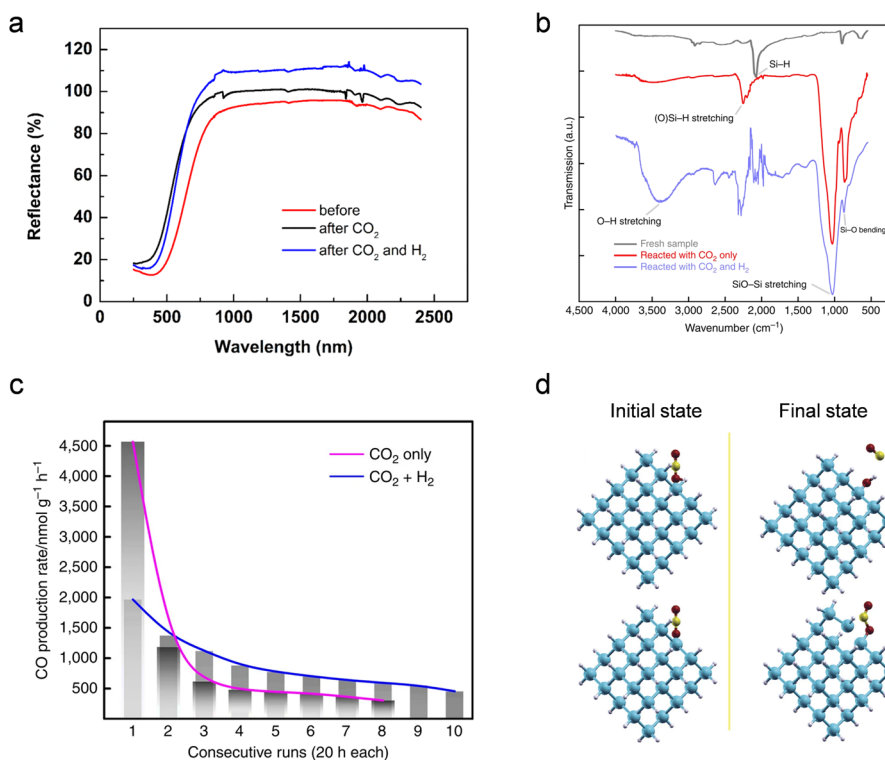
Fig. 3 Catalytic CO₂ reduction by silicon nanocrystal. a UV-vis diffuse reflectance spectra of Si nanocrystals deposited on the glass fiber filter. **b** FTIR spectra of fresh powder of hydride-terminated silicon nanocrystals before and after the reaction. **c** CO production rates (pure $^{13}CO_2$ in the batch reactor at 150 °C) for eight cycles, and CO production rates ($^{13}CO_2$ and H_2 with 1:1 ratio in the batch reactor at 150 °C) for 10 cycles, both under light (one sun). **d** The initial and final optimized models of CO_2 adsorption on SiH (top panel) and Si surface sites (bottom panel) (**a**–**d** are reproduced with permission from ref. [119], Copyright© Springer Nature 2016).

following cycles (Fig. 3c). In contrast, an increased CO production rate was observed when H_2 was introduced into the reactor. In most cases, the samples showed higher CO production rate under the light at the same heating temperature, and higher rate at increasing temperature. By DFT modeling of a $Si_{35}H_{36}$ cluster, the authors revealed that the dangling bonds at the Si sites can adsorb and activate CO_2 molecule with a binding energy of 0.63 eV (Fig. 3d). The Si−H site dissociates CO_2 into CO, leading to endothermic formation of Si−OH bonds. Recovery of Si−H bond by reaction between H_2 and Si−OH is kinetically difficult, resulting in degraded activity over time. Nevertheless, the presence of H_2 is believed to suppress the oxidation of Si nanoparticle surface, as the formation of Si−O−Si bonds is much reduced compared with the situation without H_2 according to the FTIR spectrum and ultraviolet-vis diffuse reflectance spectrum.

Selective CO_2 conversion to methanol (CH_3OH) by porous Si nanoparticles with hydride surfaces was reported by Dasog and co-workers[120]. These nanoparticles were synthesized via magnesiothermic reduction method and etching with HNO_3/HF. The thermal reduction of CO_2 on the hydride surfaces of Si nanoparticles, which was monitored by in situ IR spectroscopy, occurs at minimum temperature and pressure of 100 °C and 10 bars, respectively. The IR spectrum showed an increase in Si−O−Si, Si−O−H, and Si−O−CH_3 vibrations during the reaction process. The yield of CH_3OH did not change significantly with the reaction temperature. The porous Si nanoparticles were recyclable up to four reaction cycles without significant loss of CH_3OH yield (~0.2 mmol), and after that, aggregation of the nanoparticles was observed. In another study, doping effect on the activity of Si hydride nanocrystals for CO_2 photo-reduction was investigated by Wong and co-workers[121]. They found that P-doping endows the Si nanocrystals with the highest activity for CO_2RR to form CO compared with B-doping or B and P co-doping, exhibiting a

maximum CO production rate of 275 nmol $m^{-2} h^{-1}$ (corresponding to 71 µmol $g^{-1} h^{-1}$) and excellent long-term stability in air. The rate drastically decreases in the second run for all samples, as most of the Si−H bonds have been converted to Si−O−Si and Si−OH groups upon CO_2 reduction. The enhanced activity is attributed to the addition of electronegative dopants, which create surface polar bonds and render the Si atom more positively charged, and thus increase the CO_2 adsorption capability and capacity.

As silicon hydrides react stoichiometrically with CO_2 but cannot achieve catalytic conversion, Qian et al. decorated silicon hydride nanosheets with Pd nanoparticles (Pd@SiNS), which enable the reverse water-gas shift reaction in a catalytic cycle under light irradiation and a temperature of 170 °C[122]. The scanning transmission electron microscopy (STEM) image showed that the Pd nanoparticles with size of about 5 nm are highly dispersed on the silicon hydride nanosheets, and meanwhile the Pd nanoparticles as separators result in less stacked nanosheets with higher surface area. Thanks to that, a CO production rate of 10,000 nmol (g cat)$^{-1} h^{-1}$ was achieved, and the rate remains at this level during long cycles up to 50 h. For comparison, pristine silicon hydrides nanosheets have lower CO production rates that drop more rapidly and are unstable. The controlled experiment also demonstrated negligible contribution of Pd nanoparticles for CO_2 reduction, as Pd nanoparticles loaded on fully oxidized Si nanosheets have no activity. Furthermore, with Pd decoration, the surface oxides and hydroxides of Si nanosheets are largely reduced by H_2 to reinstate surface hydrides, according to in situ diffuse reflectance infrared Fourier transform spectroscopy (DRIFTS) with isotope labeling. DFT calculations were then performed to unveil the role of Pd nanoparticles. The mechanism for recovery of the hydrides surface involves the reaction of H_2 with Si−O−Si bonds to the formation of Si−OH and Si−H, and

then the reaction of H_2 with Si−OH to produce Si−H and H_2O, with the latter step being endothermic. Due to the favorable interaction between Pd nanoparticles and H_2, the reduction of Si−OH to H_2O becomes much less endothermic compared with that of the pristine Si nanosheets, and thus help reinstate the surface hydrides for catalytic reaction.

To gain deeper insights into the above intriguing experimental results, Ji et al. modeled the possible reaction pathway of CO_2RR on H-terminated Si(111) surface by DFT calculations[123]. For fully H-terminated Si(111) surface, direct reaction of CO_2 with the adsorbed H* species to form COOH* intermediates requires an effective barrier of 2.96 eV, which is much lower than that for inserting CO_2 into Si−H bond to form CO and Si−OH. Higher activity can be achieved on the surface Si atom without H termination, which may be produced during light illumination, heat, and loading of the metal nanoparticles. On an isolated exposed Si atom or two neighboring exposed Si atoms, CO_2 molecule can be chemisorbed on the Si sites, and the most efficient pathway for the reduction reaction is direct decomposition of CO_2 into a CO gas molecule and an O adatom. The isolated exposed Si site has higher activity with an effective barrier of 1.49 eV. Then, the remaining O* species can combine with an adjacent H atom on the Si surface to generate an OH* species, which may be further reduced to H_2O in presence of Pd nanoparticles as a beneficial H_2 decomposer.

Besides the H-modified silicon nanostructures, SiC quantum dots functionalized by hydroxyl groups were reported to have remarkable activity for CO_2 hydrogenation. Peng et al. synthesized SiC quantum dots by etching the commercial SiC powders in cubic (3C) polytype by nitric acid and hydrofluoric acid[124]. The quantum dots with an average diameter of 3.2 nm are highly dispersed, and the Si−O and O−H bonds are observed by FTIR measurements, indicating the presence of OH groups on the SiC surfaces. Under 32 bar of CO_2/H_2 mixed gas (CO_2:H_2 = 1:3) at 150 °C, the SiC quantum dots selectively produce methanol with mass activity of 169.5 mmol g^{-1} h^{-1}, about three orders of magnitude higher than that of commercial SiC (0.1 mmol g^{-1} h^{-1}). To confirm the role of OH groups on the activity, the authors removed the surface OH groups from SiC quantum dots by heating at 280 °C under a flow of N_2 and used water with DMF as the solvent for CO_2 hydrogenation to avoid the recovery of OH groups. As a result, the mass activity is reduced to only 9.5 mmol g^{-1} h^{-1}. Further thermal treatment in water can activate the SiC quantum dots or the commercial SiC surface via the formation of OH species. In addition, the isotope experiments and in situ DRIFTS measurements proved that the surface OH groups of SiC quantum dots are directly involved in the hydrogenation of CO_2 into HCOO* species. By DFT calculations, the authors disclosed that the SiC(111) surface with exposed Si sites strongly binds CO_2 molecule with an adsorption energy of 3.2 eV and can spontaneously dissociate H_2. Hydrogenation of CO_2 to HCOO* intermediate by reaction with an adsorbed H atom on SiC(111) requires a kinetic barrier of 2.10 eV, while reaction with the H atom in the surface OH groups of SiC (111) involves a barrier of 1.36 eV, leaving an O atom at the bridge site. This O adatom can further react with a dissociated H atom to reinstate an OH group on the SiC(111) surface. These experiments shed light on utilizing silicon for photo- and thermal-catalysis of CO_2 conversion by proper surface functionalization, provide the essential insights into the underlying mechanism, and offer feasible strategies to improve their performance.

2D silicon-based materials

Stimulated by the rise of graphene, 2D silicon-based materials have attracted tremendous attentions[125]. The elementary form as well as several compound forms of 2D Si have been predicted and synthesized[126–129]. Their well-defined structures, large area, and unique electronic band structures render them as ideal platforms for exploring the catalytic mechanism and unveiling the fundamental principle for manipulating the activity of silicon-based nanostructures. Silicene, the Si analog of graphene, is a single layer of Si atoms arranged in low-buckled honeycomb lattice. Same as graphene, silicene also exhibits Dirac cones at the Fermi level. Therefore, the low-energy charge carriers in silicene behave as massless Dirac fermions, which is a great advantage for many device applications. Theoretical efforts have been devoted to understanding the intrinsic reactivity and environmental stability of freestanding silicene[130–135]. It was shown that silicene is a potential gas sensor for detecting pollutant gases, such as NO, NO_2, NH_3, and SO_2. These gas molecules can even dissociate on silicene by overcoming relatively low kinetic barriers, indicating the appreciable activity of silicene surface. In particular, silicene was predicted to be hydrophilic and strongly interact with H_2O molecule.

DFT calculations showed that H_2O dissociation on freestanding silicene is easy with a moderate barrier of 0.85 eV, and becomes almost barrierless on silicene with presence of single or double vacancies[134]. Monomer, dimer, and trimer of H_2O molecules were found to exhibit distinct adsorption behavior on silicene[136]. A single H_2O molecule physisorbs on freestanding silicene through weak vdW interaction with an adsorption energy of −0.17 eV. Dimeric and trimeric H_2O molecules are chemically adsorbed on silicene by forming Si−O bonds, with adsorption energies of −0.67 and −1.19 eV, respectively. Ab initio molecular dynamics (AIMD) simulations further demonstrated that H_2O molecules at room temperature change from physical adsorption to chemical adsorption on silicene, and finally dissociate after 1 ps. Electronic structure analysis revealed that hydrogen bonding has significant effect on the proton transfer between H_2O molecules and charge transfer between silicene and H_2O. Specifically, the hydrogen bonding between dimeric or trimeric H_2O molecules induces a weakened O–H bond of the donor H_2O molecule (signified by the elongated O–H bond length), which in turn activates the corresponding O atom on top of silicene and leads to the formation of Si–O bond. In consistency, the frontier molecular orbital levels of the donor molecule become closer to the Fermi level of silicene; thus their interaction is stronger than that of H_2O monomer. Moreover, silicene supported on Ag(111) substrate exhibits even higher activity, with the enhanced adsorption energy of H_2O dimer and trimer (−0.93 and −1.64 eV, respectively), due to electron transfer from Ag substrate to silicene, while a single H_2O molecule still physisorbs on silicene. The hydrophilicity would endow silicene with broad applications in metal-free electrocatalysis of ORR and water splitting.

Experimentally, silicene has been grown on various substrates, such as Ag, Ir, Al_2O_3, ZrB_2, ZrC, and MoS_2[125]. The substrate interaction not only stabilizes the atomic Si layer, but also provides an opportunity for modulating the electronic band structure and surface reactivity of silicene. In this regard, Zhou et al. proposed to use monolayer and few-layer silicene on Ag(111) substrate for catalysis of CO_2 hydrogenation, with product selectivity controlled by the number of silicene layers[137]. They considered mono- and few-layer silicene on Ag(111) substrate with Si($\sqrt{7} \times \sqrt{7}$)/Ag ($\sqrt{13} \times \sqrt{13}$) reconstruction, which has been well identified in laboratory. Using DFT calculations, the authors showed that the supported monolayer and bilayer silicene sheets exhibit reconstruction with notable distortion from the perfect honeycomb lattice, while trilayer and tetralayer silicene start to become ordered, similar as that of bulk Si(111) structure. The silicene surface presents dangling bonds as revealed by the prominent electronic states near the Fermi level, mainly arising from the p_z orbitals of the surface Si atoms and indicating their chemical reactivity (Fig. 4a). As the number of silicene layers increases, the dangling bond states are more restricted to a narrow energy range and shift to a higher energy level in the DOS, signifying the enhanced activity (Fig. 4b). Accordingly, these silicene
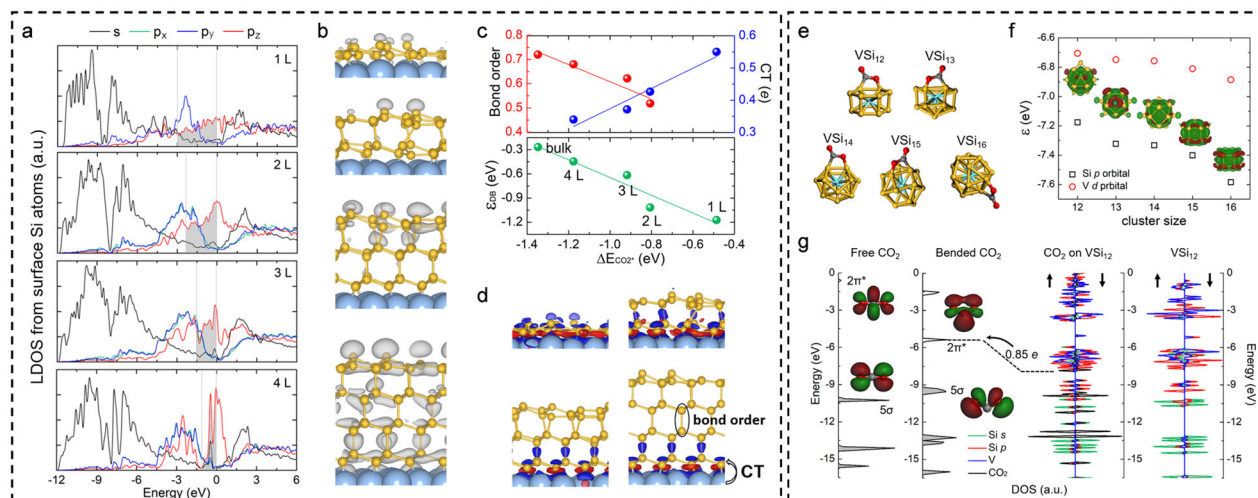
Fig. 4   Silicene on Ag(111) substrate for CO₂ hydrogenation. a LDOS from surface Si atoms in monolayer and few-layer silicene on Ag(111) projected onto various atomic orbitals. **b** Partial charge density distributions (gray colors) of the surface dangling bonds at Fermi energy. **c** Top panel: Si–Si bond order between neighboring silicene layers (red symbol) and electron transfer (CT) from the Ag substrate to silicene (blue symbol); bottom panel: energy levels of surface dangling bonds states (ε_{DB}) as a function of CO_2 adsorption energy (ΔE_{CO_2*}). **d** Differential charge density distributions between the silicene sheet and Ag(111) substrate (**a–d** are reproduced with permission from ref. [137], Copyright© The Royal Society of Chemistry 2019). **e** Structures of VSi_n clusters chemisorbed with a CO_2 molecule. **f** The p-orbital center (ε_p, black symbols) and coordination number (CN, red symbols) of Si atoms as a function of the cluster size. **g** From left to right: DOS of a free CO_2 molecule, bended CO_2 molecule, CO_2 chemisorbed on the VSi_{12} cluster, and a standalone VSi_{12} cluster, respectively (**e–g** are reproduced with permission from ref. [140], Copyright© American Chemical Society 2019).

superstructures can chemisorb CO_2 molecule with adsorption energy enhancing from −0.49 to −1.18 eV as the thickness increases from monolayer to tetralayer (Fig. 4c). The adsorbed CO_2 molecule is bent with one O atom and one C atom bonded to Si atoms having an O–C–O angle of about 120°, demonstrating the activation of CO_2 molecule. Meanwhile, the silicene superstructures can also dissociate H_2 into two H atoms with kinetic barriers of 0.06–0.49 eV, and thus are suitable for catalyzing CO_2 hydrogenation. The monolayer to tetralayer silicene on Ag substrate exhibit distinct free energy diagrams for CO_2 reduction toward C_1 products due to their different binding capability with the reaction intermediates. Monolayer silicene on Ag(111) provides relatively weak binding strength, such that CO and HCOOH molecules as the main reduction products can desorb easily from silicene surface. Tetralayer silicene on Ag(111) has stronger binding capability and may be able to promote CO_2 reduction toward CH_3OH and CH_4 products. The activity is related to the energy levels of the surface dangling bond states (ε_{DB}), which in turn is mediated by the covalent interaction between silicene layers and suffers from the screening effect from Ag substrate (Fig. 4d). Specifically, ε_{DB} is defined as

$$\varepsilon_{DB} = \int ED(E)dE / \int D(E)dE \qquad (7)$$

where $D(E)$ is the density of states from p_z orbitals of surface Si atoms at a given energy E; the integral is taken for the occupied states of surface dangling bond, with this energy range determined by the partial charge density distribution (Fig. 4b). As the number of silicene layers increases, ε_{DB} shifts to higher position that may interact with the $2\pi^*$ orbital of CO_2 more favorably, thus leading to stronger binding strength with CO_2 molecule. This electronic structure-activity relationship can be regarded as another version of the aforementioned "p band model" in the section "Hybrid catalysts of graphitic carbon and transition metal-based materials", and illuminates the basic rule for precisely modulating the catalytic behavior of silicon-based nanostructures.

The above catalytic mechanism based on surface dangling bonds can also be extended to Si clusters, which have high atomic

utilization. In the intermediate size range, pure Si clusters usually have irregular shapes and do not favor hollow cage structures as that of carbon fullerene[138]. By encapsulating a transition metal atom into the Si cluster, it is possible to form cage-like structure of Si. A variety of endohedrally doped Si clusters have been theoretical predicted and produced in laboratory, which have relatively high stability and sizeable HOMO-LUMO gap[139]. Among them, Ti- and V-doped Si clusters (MSi_n, M = Ti or V, n = 12–16) were predicted to have high activity for CO_2 hydrogenation, with the product selectivity determined by cluster size[140,141]. All these clusters have cage-like structures with the endohedral transition metal atom accepting electrons from the surrounding Si atoms (Fig. 4e). The dangling states of surface Si atoms are not fully saturated, since electron accumulation is evident on the Si cage (Fig. 4f). CO_2 chemisorption and hydrogenation are possible on these MSi_n clusters, leading to the formation of various C_1 products with low kinetic barriers. The correlation between CO_2 adsorption energy and the p orbital center of Si atoms is also observed for these endohedrally doped Si clusters, i.e., the smaller-size Si cluster has a higher p orbital center, and provides stronger binding with CO_2 (Fig. 4f, g).

Siloxene, with the chemical formula of $Si_6H_3(OH)_3$, is H- and OH-modified silicene, and can be prepared by topochemical deintercalation of Zintl phase $CaSi_2$[142]. Siloxene possesses a 2D structure featured by an array of Si chains interconnected with O bridges and terminated by H atoms. It is a direct semiconductor with band gap of 2.50 eV, and it effectively absorbs visible light and has sufficient reduction capacity. Li et al. proposed that the HOMO and LUMO of siloxene are delocalized over the p-conjugated skeletons, which is helpful for the molecular charge-transfer transition under light irradiation and beneficial for photocatalysis[143]. They fabricated siloxene nanosheets for photocatalysis of overall water splitting, and achieved a maximum H_2 production rate of 11.4 mol g⁻¹ h⁻¹. The UV-vis spectrum revealed the generation of H_2O_2, suggesting that photocatalytic water splitting on siloxene undergoes a two-electron pathway. Siloxene has also been reported to possess activity for electrocatalysis of ORR and HER[144] as well as photocatalysis of NO removal[145].

Besides siloxene, nanosilica has also been exploited as a catalyst. Mishra et al. prepared amorphous defective nanosilica and achieved excellent stability, activity and selectivity for thermal conversion of CO_2 to methane[146]. Three types of defects with controllable concentrations were introduced in nanosilica, which synergistically contribute to the high activity with maximum methane production rate of 9569 $\mu mol\, g^{-1}\, h^{-1}$ at 550 °C. DFT calculations revealed that the CO_2 molecule chemisorbs on silica surface in a bidentated configuration with an adsorption energy of −0.77 eV. The C atom interacts with the non-bridging O hole center and one O atom of CO_2 interacts weakly with neighboring Si site. At these defect sites, CO_2 hydrogenation to CH_4 is energetically and kinetically more favorable than that of CO production. Therefore, defect engineering is also a potential strategy for tailoring the abundant silicon-based nanomaterials for selective CO_2 conversion.

Some other 2D compound forms of silicon have been predicted in theory. Monolayer SiX_n (X = P, As; n = 1, 2) have moderate band gap ranging from 1.89 to 2.65 eV and are regarded as potential photocatalysts[147,148]. For instance, monolayer SiP_2 and $SiAs_2$ can exist in the tetragonal and orthorhombic phases, and have good mechanical, dynamical and thermal stabilities. With small cleavage energies comparable to that of graphene, these new 2D materials may be exfoliated from their bulk counterparts. Moreover, they have high carrier mobility, strong optical absorption in the visible region, and suitable band edge positions, which are eligible for photocatalytic water splitting[149,150].

In summary, silicon-based nanomaterials, with the advantages of natural abundance and excellent capability of solar energy harvesting, can be utilized for many renewable energy applications. Silicon nanowires, compound nanocrystals or nanoscale derivatives of silicon, 2D elementary and compound forms of silicon, and 0D endohedrally doped silicon clusters are reported to possess unique catalytic properties. The surface Si atoms with dangling bonds usually exhibit high activity for water dissociation and CO_2 activation, providing the opportunity for efficient water splitting and CO_2 conversion. The activity can be correlated to the p orbital energy level of the Si atoms. More mechanistic studies are still required to disclose the catalytic behavior of various silicon-based nanostructures from the atomic level, and prescribe the principles for manipulating their performance for energy conversion.

OXIDE-BASED CATALYSTS

Metal oxides provide a large family of non-precise catalysts with the advantages of natural oxidation resistance, relatively high stability, easy synthesis and control, myriad compositions and structures, and diverse electronic properties. These oxide materials have been widely used for industrial catalysis, photo- and electro-chemical processes. For example, the composites of metals (e.g., Cu, Fe, Co, Ni) and metal oxides (e.g., Al_2O_3, ZnO, ZrO_2) are commercial catalysts for CO_2 hydrogenation to selectively generate value-added chemicals or fuels[151]. Transition metal oxides and perovskite oxides are commonly adopted for oxygen-related electrochemical reactions[152,153]. Photocatalysis of CO_2 reduction and N_2 reduction largely relies on metal oxides, such as TiO_2, WO_3, ZrO_2, CdS that have suitable band gap and outstanding light harvesting ability[154]. Sculpturing metal oxides into 2D nanosheets or 0D nanoclusters results in large surface area and abundant active sites, which may trigger peculiar catalytic behavior for challenging reactions[155].

For many reported metal oxides, the reaction centers are considered to be surface or interface metal atoms, oxygen vacancies, or defects[156]. Actually, the O atoms in metal oxides can also play an important role in the catalysis. Oxide metal hybrid nanostructures, either metal nanoparticles loaded on metal oxide substrates, or oxides supported on metals (the so-called inverse catalysts), exhibit remarkable synergistic effects to enable challenging reactions[157,158]. They provide diverse binding sites for the reaction intermediates, i.e., on the metal domains, on the oxide surface or overlayer, or at the metal oxide interface, which afford complementary chemical properties and lead to special reaction pathways. The cooperation between metal and O sites in such hybrid catalysts has been largely addressed in literature[159,160]. A common example is the tuning of product selectivity for CO_2 hydrogenation on transition metal nanoparticles by simply changing the oxide substrate, due to the variation of binding strength of some key reaction intermediates on the oxide surfaces[161].

The lattice O atoms in metal oxides can even dominate the catalytic reactions. Early studies on metal clusters have shown that the oxygen-centered radicals ($O^{-\bullet}$) may present in some transition metal clusters, and they play a key role in the oxidation or oxidative transformation of very stable molecules at low temperature, such as CO oxidation and CH_4 activation. Mass spectrometric studies combined with DFT calculations have been performed to unveil the chemical compositions of the transition metal oxide clusters that carry such $O^{-\bullet}$ radicals, as well as the dependency of their activity on the cluster size, structure, and charge state. It was found that the mono-nuclear $O^{-\bullet}$ radicals generally exist over the oxide clusters of groups 3–7 metals (except Cr and Mn). For C–H activation of alkanes like CH_4, the reactivity of $O^{-\bullet}$ radicals depends on the charge state of oxide cluster and the degree of spin density localization. The transfer of O atom usually occurs during the reactions from the oxide clusters to CO and alkenes molecules. The structure-activity relationships of metal oxide clusters with both mono-nuclear and hetero-nuclear $O^{-\bullet}$ radicals are well understood. As this category of low-dimensional catalysts has been comprehensively addressed in literature[162,163], we will not discuss this topic in details in the present review.

In this section, we will focus on the solid-state metal oxides with the lattice O atoms as the active sites for energy conversion. We aim to disclose the origin of activity of lattice O atoms, their catalytic mechanism, and the key factors governing the activity, and discuss the strategies to trigger and manipulate the activity of surface O atoms in various metal oxides.

Lattice O atoms for OER

Transition metal oxides and perovskite oxides are mostly adopted for OER electro- and photo-catalysis. Conventionally, surface metal atoms are considered as the active sites, where the oxygenate intermediates are adsorbed. The reaction occurs on a single metal site via either four-electron pathway or two-electron pathway, both belonging to the so-called adsorbate evolution mechanism (AEM) (Fig. 5a). The intrinsic activity based on the AEM is limited by the scaling relations between different reaction intermediates (O*, OH*, and OOH*), yielding a minimum OER overpotential of about 0.37 V[164]. Experiments found that the surface O atoms in perovskite oxides can have redox activity and participate in the bonding and charge transfer with the reaction adsorbate species[165]. The lattice oxygen mechanism (LOM) was proposed by Kolpak and co-workers for $LaNiO_3$, a perovskite oxide with high activity but low stability for OER electrocatalysis[166]. The LOM initiates from the adsorption of OH^- on a metal site, followed by the deprotonation of OH* to generate O* species, which then couples with a lattice O atom to form O–O*. The release of O_2 leaves two vacant metal centers, where adsorption and deprotonation of OH* occur to restore the lattice O atom. As OOH* is not an intermediate in the LOM catalytic cycle, the OER activity is no longer restricted to the scaling law, and higher activity may be achieved. By DFT calculations, the authors predicted that LOM overwhelms AEM in $LaNiO_3$ under certain pH values and applied electrode potentials, yielding a low overpotential of 0.31 V
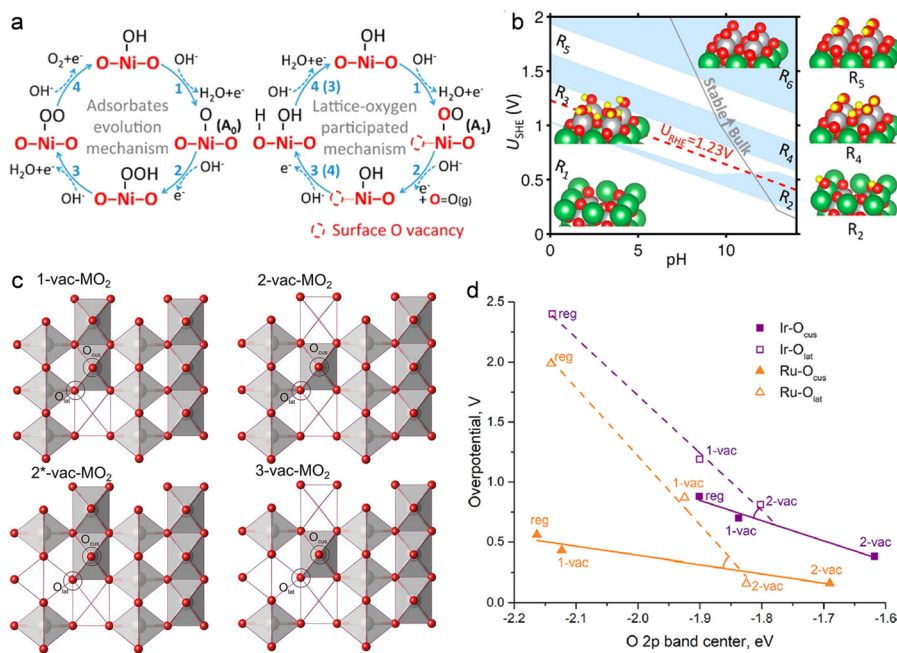
Fig. 5 **Types of OER and relation between OER activity and O *p*-band center. a** Schematics of AEM and LOM. **b** Computed surface phase diagram relevant to AEM for LNO in aqueous solution. Surface structures are labeled in each colored region (**a** and **b** are reproduced with permission from ref. [166], Copyright© American Chemical Society 2016). **c** Top view of the structural models for MO$_2$(110) (M = Ru, Ir) containing one, two, and three M vacancies. White polyhedra depict the positions of vacancies. **d** Correlation between the computed OER overpotential and O 2*p*-band center for AEM (solid line) and LOM (dashed line) for MO$_2$(110) (M = Ru, Ir) surface (**c** and **d** are reproduced with permission from ref. [174], Copyright© American Chemical Society 2020).

(Fig. 5b). For a range of perovskites ABO$_3$ (A = La, La$_{0.5}$Sr$_{0.5}$, Sr, and B = Mn, Fe, Co, Ni), OER prefers LOM for decreasing catalysts stability, i.e., LOM would be dominant on the perovskites that are less stable than La$_{0.5}$Sr$_{0.5}$CoO$_3$.

In the successive studies, Kolpak and co-workers showed that the adsorbed O* species diffuses from the surface metal site to O site to form O–O* and an O vacancy[167]. Therefore, diffusion of O* is crucial for LOM, which is more favorable for the weakly binding perovskites like LaCuO$_3$. The origin of LOM is related to the surface metal atoms recovering from the highly oxidized state to the electronically more stable and lower oxidation state throughout the reaction. The different thermodynamic driving forces of lattice O participation on different perovskites can be understood by the differences in the transition metals' tolerance toward high oxidation states. They also established the volcano plots for AEM and LOM on a variety of perovskite oxides[168]. The higher peak of the LOM volcano successfully explains the experimental observation that some perovskites such as Pr$_{0.5}$Ba$_{0.5}$CoO$_{3-\delta}$ and SrCoO$_{3-\delta}$ have higher OER activity than the conventionally predicted optimum compounds such as LaNiO$_3$ and SrCoO$_3$. By reversing LOM, ORR electrocatalysts can be computationally screened, and some bifunctional electrocatalysts for both OER and ORR may even be designed[169].

On the experimental aspect, LOM has been demonstrated in various kinds of material systems, such as perovskite oxides, transition metal oxides, and transition metal-based layered double hydroxides (LDHs)[170,171]. Based on in situ ^{18}O isotope labeling mass spectrometry, Grimaud et al. provided direct experimental evidence that the O$_2$ generated during OER electrocatalysis on some highly active oxides come from the lattice O atoms[172]. Specifically, electrochemical OER in LaCoO$_3$, La$_{0.5}$Sr$_{0.5}$CoO$_{3-\delta}$, Pr$_{0.5}$Ba$_{0.5}$CoO$_{3-\delta}$, and SrCoO$_{3-\delta}$ was examined, and the release of ^{16}O^{16}O, ^{16}O^{18}O, and ^{18}O^{18}O was observed in the latter three systems. In consistency, OER activities on the reversible hydrogen electrode (RHE) scale for these three perovskites become higher with increasing pH value, indicating that the non-concerted

proton–electron transfer steps are coupled to the activation of lattice oxygen redox reactions. In contrast, the activity of LaCoO$_3$ is independent on the pH value, as expected from the conventional OER mechanism. The electronic structure analysis suggested that the metal–O covalency plays a key role in both activity and OER mechanism. For La$_{0.5}$Sr$_{0.5}$CoO$_{3-\delta}$, Pr$_{0.5}$Ba$_{0.5}$CoO$_{3-\delta}$, and SrCoO$_{3-\delta}$, the presence of divalent ions on the A-site shifts the Fermi level closer to the O 2*p*-band center, accompanied by a reduced energy gap between the metal 3*d* and O 2*p*-band centers, and signifying greater covalency of the metal–O bond. As the O 2*p* states at the Fermi level lie above the redox potential of O$_2$/H$_2$O, holes are created in the O band, allowing the oxidized O ions to form (O$_2$)$^{n-}$ species. Thus, oxidation of lattice O in the perovskites with strong metal–O covalency is thermodynamically more favorable. Furthermore, it was observed that the more O$_2$ generated during OER, the greater value for ^{18}O/^{16}O, indicating that the amount of lattice O atoms detected during the OER process indeed depends on the position of the O *p* states relative to the Fermi level and correlates with the OER activity.

The reaction mechanism in the benchmark OER electrocatalysts RuO$_2$ and IrO$_2$ has also been re-visited from both experimental and theoretical aspects[173]. DFT calculations suggested that structural defects or heteroatom doping can make the LOM competitive to AEM for rutile RuO$_2$ (Fig. 5c)[174]. In particular, the (110), (211), and (121) double-kink surfaces of RuO$_2$ with metal vacancies or substitutional dopants (Ni and Co) prefer LOM and the overpotentials are much lower than that of AEM. The simultaneous presence of both metal vacancy and elemental doping can synergistically promote LOM, which well interprets the experimentally observed involvement of lattice O atoms in the nanocrystalline RuO$_2$, but not for the ideal RuO$_2$ films. The projected DOS reveals a clear correlation between the O 2*p*-band center and OER overpotential as shown in Fig. 5d, i.e., the closer of O 2*p*-band center to the Fermi level, the higher OER activity. These plots also suggest that the LOM in RuO$_2$ is more sensitive to the formation of metal vacancies than that of IrO$_2$, as reflected by their

different angles between the lines for LOM and AEM. The less preferential LOM in IrO_2 explains its higher stability under the OER conditions than that of RuO_2. In another study, the authors explored the OER mechanism and electrochemical activity for various Ir oxides[175]. Some of them, such as the pyrite $IrO_2(100)$, favor LOM rather than AEM and exhibit enhanced OER activity with lower kinetic barriers than that of the rutile IrO_2. The higher activity of these Ir-based oxides comes at the expense of their electrochemical stability since lattice O atoms are involved in the reaction.

On the experimental side, Grimaud et al. designed a model catalyst La_2LiIrO_6 to understand the correlation between surface activity and stability of Ir-based oxides for OER electrocatalysis[176]. By changing pH from acidic to alkaline condition, La_2LiIrO_6 undergoes oxidation and delithiation, accompanied by the drastic surface reconstruction as revealed by the transmission electron microscopy (TEM). The results showed that the metallic t_{2g}-like π^* states are inactive and the $Ir^{5+}-O$ bond is not active for OER. Instead, formation of the oxidized surface at $pH = 1$ leads to an enhanced OER activity as the Fermi level enters the non-bonding pure oxygen states, creating oxygen radicals on the surface that behave as electrophilic centers for reaction with H_2O. The enhanced reactivity of surface oxygen species is at the expense of surface stability, as the consumption of lattice O atoms eventually leads to the Ir migration from the bulk interior to the catalyst surface. Zhang et al. fabricated Ru–Ir binary oxides for OER electrocatalysis in the neutral electrolyte[177]. By incorporating hydrated metal cations (Ca^{2+}), the surface oxygen environments of binary oxides can be modulated to generate either lattice O or adsorbed O species. The synthetic $RuIrCaO_x$ catalysts exhibit 2, 7, and 45 times higher turnover frequency (TOF) compared to $RuIrO_x$, benchmark RuO_2, and IrO_2 catalysts, respectively. According to in situ X-ray absorption spectroscopy (XAS), in situ ^{18}O isotope-labeling differential electrochemical mass spectrometry, and ^{18}O isotope-labeling secondary ion mass spectroscopy measurements, the incorporation of Ca^{2+} shortens the Ru–O and Ir–O bonds to endow them greater covalency. As a result, the surface metal-bonded O species exhibits enhanced electrophilic nature, which accelerates H_2O adsorption and lattice O-involved reaction and thus improves the overall OER performance of $RuIrCaO_x$.

The lattice O-dominated OER has also been demonstrated in the transition metal oxyhydroxides. Huang et al. incorporated catalytically inactive Zn^{2+} cations into CoOOH to induce oxygen non-bonding states with different local configurations[178]. Their DFT calculations suggested that the OER mechanism can be switched from AEM to LOM only if two neighboring oxidized O atoms can hybridize their oxygen holes without sacrificing metal–O hybridization significantly. As a proof of concept, they designed $Zn_{0.2}Co_{0.8}OOH$ electrocatalyst with the $Zn–O_2–Co–O_2–Zn$ configuration that manifests the optimal activity. Raman spectra further identified the negative peroxo-like species from LOM of OER. Zhang et al. fabricated oxyhydroxides of multicomponent FeCoCrNi alloy to engineer the oxidation state of Ni atom[179]. During the OER electrocatalysis, the alloyed oxyhydroxides undergo irreversible surface reconstruction and form highly oxidized metal species. The spectroscopic measurements and theoretical modeling revealed that interatomically electronic interplay plays a key role in the engineering of oxidation state of Ni and its preferential OER mechanism. Specifically, Fe atoms induce electron depletion at Ni sites to form high oxidized Ni^{4+} species that favor the LOM pathway. The pre-adsorbed bridging OH* species at the Ni–Co sites allows a multistep evolution of $Ni^{2+} \rightarrow Ni^{3+} \rightarrow Ni^{4+}$ with lowered energy barriers. The Ni^{4+} species drives holes into O ligands to facilitate intramolecular oxygen coupling, and triggers the lattice O activation. The coupled peroxo-like oxygen species forms at the Fe–Ni dual-site, which serves as the catalytic center for LOM with high intrinsic activity. Besides, LOM was also

reported in transition metal oxyhydroxides composited with perovskites. Zhao et al. deposited FeOOH clusters on the surface of $LaNiO_3$, which exhibit increased activity for electrocatalytic OER by up to a factor of five relative to pristine $LaNiO_3$[180]. The decoration of FeOOH enhances OH* adsorption, weakens the Ni–O bonds in $LaNiO_3$, and meanwhile shifts the O $2p$ bands closer to the Fermi level; all of these effects promote the lattice O participation in OER.

Regarding the active O atoms on various metal oxides surfaces, a more general picture based on chemical bonding theory has been proposed to establish a direct correlation between the electronic structure and binding properties of oxide catalysts akin to the d band theory for transition metals[181]. Dickens et al. examined the reactivity of adsorbed O atoms on transition metal and transition metal oxide surfaces. Specifically, they were interested in the energy required to deprotonate adsorbed OH* species to create O* species ($\Delta E_O - \Delta E_{OH}$). A universal linear relationship was found between ($\Delta E_O - \Delta E_{OH}$) and the average O $2p$-state energy (ε_{2p}), which is applicable for a wide range of material systems, including FCC metal (111) surfaces, rutile metal oxide (110) surfaces, and cubic perovskite (100) surfaces. Here the definition of ε_{2p} has the same form of Eq. (6), with the integral taken from -10 to 2 eV relative to the Fermi level, in order to include all the occupied and unoccupied O $2p$ states that are chemically relevant for the transformation between adsorbed O* and OH* species. The bound O atoms with higher-lying $2p$-states have higher ($\Delta E_O - \Delta E_{OH}$), namely, stronger affinities for binding H atom. Such correlation can be understood as that the variation of O $2p$-states actually manifests the changes in M–O bond strength and metal d-band center, while ($\Delta E_O - \Delta E_{OH}$) is a good proxy for the M–O hybridization energy. As the reactivity of surface O atoms is important for many reactions such as OER and methane activation, ε_{2p} can be used as a descriptor to identify the active sites on complex metal oxide surfaces for various reactions.

In short, the above experimental and theoretical studies highlight the key role of lattice O atoms in catalysis, and demonstrate the importance for considering new reaction mechanisms when optimizing or designing catalysts. By illuminating the electronic structure-activity relationship for the surface O atoms, several feasible strategies have been provided to precisely tune the OER activity of metal oxides and design new electrocatalysts with ultrahigh efficiency.

2D metal oxides with active O atoms

Two-dimensional metal oxides hold many advantages for energy conversion and storage, such as outstanding stability and resistance to oxidation, large surface area and abundant active sites, tunable electronic band gap and optical properties, fast charge transport due to the ultrathin thickness. In laboratory, there are a variety of synthesis methods to produce 2D metal oxides or their ultrathin films, including the "top-down" and "bottom-up" approaches. Numerous kinds of 2D metal oxides have been fabricated, such as MnO_2, Co_3O_4, Cr_2O_3, HfO_2, Al_2O_3, Gd_2O_3, as well as 2D perovskites[182]. Only some of 2D metal oxides have intrinsic layered structures (such as MoO_3, WO_3, Ga_2O_3, and V_2O_5) and can be exfoliated from their bulk crystals[183]. Those with non-layered geometries may comprise a large number of defects or dangling bonds on the surface, whose atomic structures are not well defined[184]. Some oxide monolayers, such as 2D FeO, may have to be stabilized on substrates[185], while some mono- or few-layer metal oxides like 2D ZnO may collapse to stable 2D arrangements during the transformation from 3D to 2D structures[186].

Although there are many experimental reports on the utilization of 2D metal oxides for energy conversion and storage[184,187], the material systems definitely having O atoms as the active sites are very limited. It is known that wurtzite ZnO sheet transforms into a
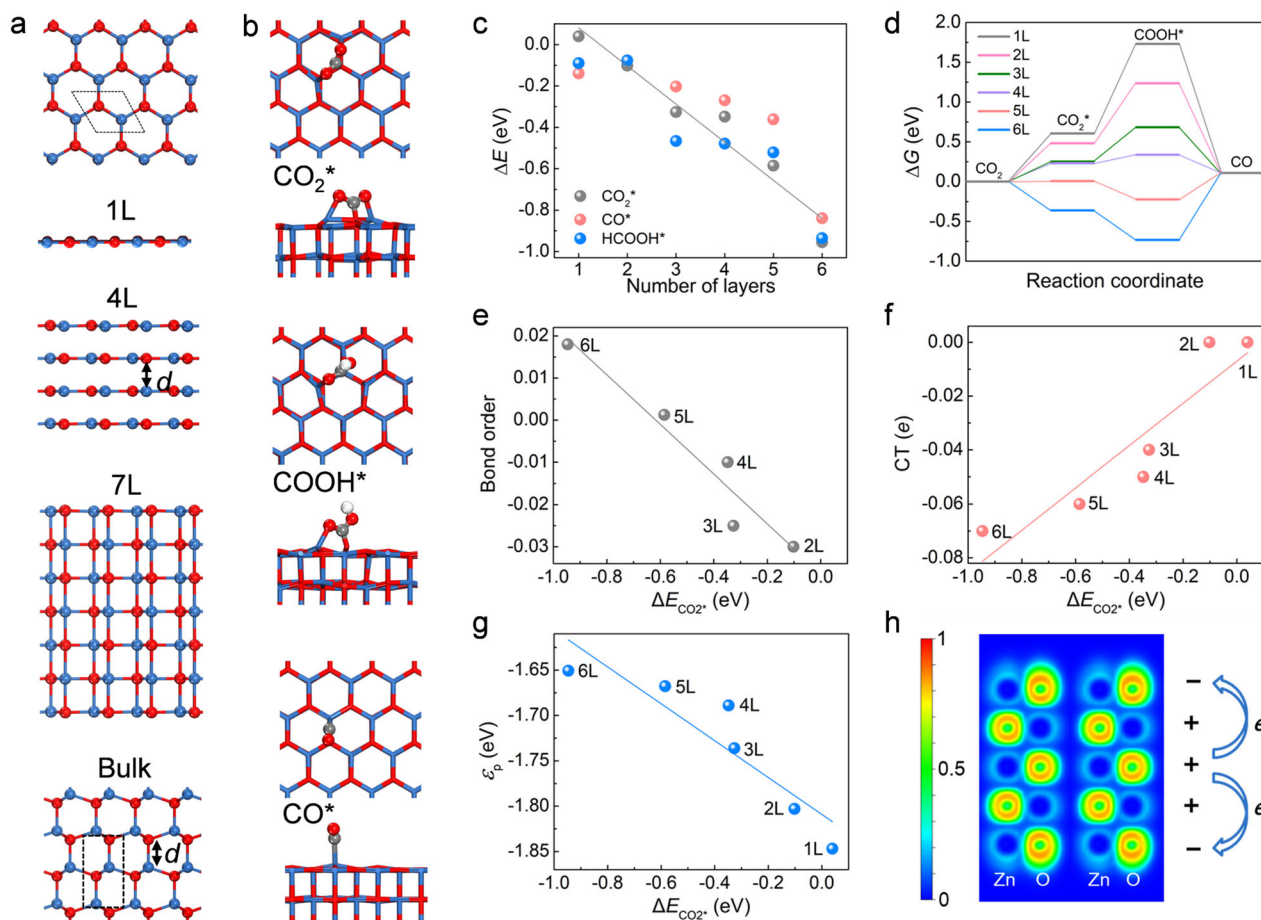
Fig. 6   2D ZnO sheets for CO$_2$ reduction. a Atomic structures of 2D ZnO (top panel: top view; bottom panels: side views of 1L, 4L, 7L, and bulk ZnO). **b** Atomic structures of CO$_2$, COOH*, and CO* intermediates adsorbed on 2D ZnO. **c** Adsorption energies of CO$_2$, CO, and HCOOH on 2D ZnO as a function of the number of layers. **d** Free energy diagram of CO$_2$ reduction to CO on 2D ZnO. **e** Mulliken bond order of Zn–O bonds from adjacent layers. **f** Mulliken charge per formula unit, and **g** 2p band center of the surface O atoms of 2D ZnO as a function of CO$_2$ adsorption energy. **h** Electron localization function of 5 L ZnO with red (blue) color showing maxima (minima), and schematic plot of electron distribution on the surface and in the interior of 2D ZnO (images are adapted from ref. [192], Copyright$^©$ The Royal Society of Chemistry 2019).

non-polar graphene-like structure when it is reduced to atomic thickness (1–7 layers). As the number of layers reaches 8, ZnO sheet starts to recover the wurtzite structure with buckled layers in the vertical direction[186]. So far, monolayer and few-layer ZnO sheets have been obtained in laboratory both in the freestanding form and deposited on various substrates. A number of experimental reports demonstrated their catalytic activity for certain reactions[188–190], and the intrinsic activity of the lattice O atoms in 2D ZnO has been predicted by DFT calculations[191].

Zhao et al. computationally explored the photocatalytic properties of 2D ZnO sheets with different numbers of layers for CO$_2$ reduction (Fig. 6a)[192]. They showed that CO$_2$ molecule can be chemisorbed on the ZnO sheets, with adsorption energies enhancing from 0.04 to −0.95 eV as the number of ZnO layers increases from 1 to 6 (Fig. 6c). Upon adsorption, the CO$_2$ molecule is bent having the C atom bonded with the O site of ZnO sheet, and the two O atoms of CO$_2$ weakly interact with the two underneath Zn atoms (Fig. 6b). Further reduction of CO$_2$ on 2D ZnO is possible, leading to the formation of CO. The 4-layer ZnO sheet provides optimal binding strength with CO$_2$ and COOH* intermediate, such that it exhibits the minimum limiting potential of 0.23 V for CO production (Fig. 6d). Meanwhile, the band gap at HSE06 level of theory decreases from 3.13 to 2.66 eV when the number of ZnO layers increases from 1 to 6, all of which show strong optical absorption in the ultraviolet regime. Their conduction band minimum (CBM) and valence band maximum (VBM)

positions straddle the redox potentials, rendering monolayer and multilayer ZnO suitable for photocatalysis of CO$_2$ reduction. The intrinsic activity of 2D ZnO is attributed to the electron accumulation on the surfaces, i.e., 0.04–0.07e per formula unit carried by the O atoms, while the interior layers are positively charged to give a zero net dipole moment (Fig. 6h). As the thickness of ZnO sheet increases, the covalency of Zn−O bonds is greater (as indicated by the larger Zn−O bond order shown in Fig. 6e) and the activity of O atoms is enhanced, consistent with the regulation found for the active O atoms on transition metal oxide surfaces described in the section "Lattice O atoms for OER". Furthermore, the electron accumulation on the ZnO surfaces is associated with the shift of O 2p band to a higher energy relative to the Fermi level, as revealed by Fig. 6f, g. A linear relationship was established between the CO$_2$ adsorption strength and the p band center (ε_p as defined in Eq. (6)) of the surface O atoms in 2D ZnO. As ε_p is a measure of metal−O covalency, increasing the number of layers leads to higher ε_p and greater covalency of Zn−O bonds, and thus induces higher activity for the O atoms to bind with CO$_2$ molecule.

Sculpturing ZnO into 0D nanoclusters can also trigger activity for the O atoms[193]. Zn$_{12}$O$_{12}$ cage cluster was predicted to be able to adsorb and reduce CO$_2$ molecule. Similar to the aforementioned 2D ZnO, the C and O atoms of CO$_2$ are bonded with the O and metal atoms in the Zn$_{12}$O$_{12}$ cluster, respectively, with an adsorption energy of −0.37 eV. By substitutional doping of a Zn

atom with transition metal, the electron density on the adjacent O atoms can be modified, which enables the tuning of both activity and selectivity of the ZnO clusters for CO_2 reduction.

MgO is another kind of earth-abundant and environmentally friendly metal oxide. To date, MgO ultrathin films down to few layers and monolayer with different facets have been epitaxially grown on Ag, Au, Mo, and Ni substrates[194–198]. Bulk MgO has the FCC structure, such that cleaving MgO from the <100> and <111> directions results in MgO monolayer with square and graphene-like lattice, respectively. Experimental and theoretical studies have shown that supporting MgO ultrathin film on metal substrates not only stabilizes the MgO sheet, but also induces high reactivity for MgO to interact with O_2, H_2O, CO, and CO_2 molecules[199–201].

Early experiment based on the high-resolution electron energy loss spectroscopy (EELS) and X-ray photoelectron spectroscopy (XPS) probed the interaction of H_2O with the ultrathin MgO films grown on Ag(100) substrate[202]. Molecular adsorption is found to be dominant on the MgO sheet at low temperature, while only OH groups are observed on the MgO surface at 310 K. For the single-layer and submonolayer MgO, the reactivity can be enhanced by a factor of 6 at room temperature. The authors attributed such high activity to the low-coordinated sites at the borders of MgO islands and important role of the Ag substrate. Using low-temperature scanning tunneling microscopy (STM), Shin et al. achieved state-selective dissociation of a single H_2O molecule on the ultrathin MgO film[203]. They prepared few-layer MgO with (100) facet on the Ag(100) substrate. Two types of H_2O dissociation were realized by injecting tunneling electrons from the STM tip, i.e., dissociation into hydroxyl groups by excitation of the vibrational state and dissociation into atomic oxygen by excitation of the electronic state. The MgO sheet is responsible for the unique state-selectivity by enhancing the lifetime of tunneling electrons in molecules, which signifies the great potential of MgO ultrathin film as a platform for chemical reactions.

On the theoretical side, the H_2O dissociation behavior on supported MgO sheets has been explored. DFT calculations showed that monolayer and bilayer MgO(100) sheets on the Ag(100) substrate can decompose H_2O molecule into H and OH species bonded with the surface O and Mg atoms, respectively[204]. The activity is tunable by doping 3d transition metal atoms into the Ag substrate. Ti doping of the Ag surface yields the highest activity for the supported MgO sheet, with stronger adsorption of H_2O molecule and lower kinetic barrier for H_2O dissociation than those of the undoped system. The chemical reactivity of the ultrathin MgO film is related to the adhesion energy, which reflects the amount of local hybridization between the electronic states of the transition metal dopant and oxide film. The extent of d state splitting in the dopant induced by the ligand field of oxide film fully correlates with the variation trend of activity. The MgO (100) film deposited on the Mo(100) substrate was also predicted to have the capability for water splitting[205]. The in-plane strain caused by the lattice mismatch between MgO film and the underlying substrate greatly affects the activity, and a 4% expansion of the MgO lattice is beneficial for H_2O dissociation.

Besides 2D MgO, (MgO)$_n$ clusters supported on g-C$_3$N$_4$ were theoretically proposed for photocatalysis of overall water splitting[206]. The subnanometer (MgO)$_n$ clusters ($n = 6$–15) with tubular geometry exhibit high activity for water splitting in the aqueous environment regardless of cluster size, leading to formation of OH and H species adsorbed on the Mg and O atoms of the cluster, respectively. The synergistic effect between the (MgO)$_n$ clusters and g-C$_3$N$_4$ substrate contributes to high absorbance of visible light, excited carriers with long lifetime and large reduction/oxidation powers, as well as bifunctional activity for OER and HER with the active sites from (MgO)$_n$ clusters and g-C$_3$N$_4$, respectively.

The MgO ultrathin films have also been demonstrated to enable CO_2 activation[207,208]. Liu et al. explored the electrocatalytic behavior of CO_2 reduction on MgO overlayers supported by different metal substrates[209]. They considered monolayer and bilayer MgO with (100) and (111) facets, deposited on the (100) and (111) surfaces of on Ag and Au substrates, respectively, as displayed in Fig. 7a. According to their DFT calculations, these MgO overlayers have outstanding stability in the aqueous environment and keep their planar structures well upon CO_2 chemisorption, while freestanding MgO monolayer and bilayer have poor stability and suffer from severe deformation upon CO_2 adsorption. Similar to 2D ZnO, the MgO overlayers on metal substrate can activate CO_2 molecule with the O and Mg atoms bonding to the C and O atoms of CO_2, respectively. The adsorption energies vary from −0.47 to −0.86 eV, depending on the facet and thickness of MgO sheet as well as the type of metal substrate. Reduction of CO_2 on the MgO overlayers is energetically favorable, with the main products CO and HCOOH formed through the COOH* and HCOO* pathways, respectively. Both O and Mg atoms provide the active sites for binding with COOH* and HCOO*, respectively. In particular, the (111) facet of MgO overlayer provides stronger binding strength than that of the (100) facet, leading to distinct selectivity, i.e., the former favors CO formation while the latter prefers HCOOH when the MgO overlayer is deposited on the Ag substrate (Fig. 7b). Interestingly, the reverse situation occurs for the Au substrate. Overall speaking, 2D MgO on Au substrate exhibits higher activity for CO_2 reduction, with more proper binding strength with COOH* and HCOO* intermediates. As MgO is a p-block insulator and both Mg and O atoms in the MgO overlayers act as the active sites, herein, their p states are directly related to the binding strength with the reaction molecules and intermediates. Band structure analysis showed that the MgO overlayer with a higher p band center (ε_p, as defined by Eq. 6) would interact more favorably with 2π* antibonding orbital of CO_2 molecule, thereby providing stronger binding with CO_2 (Fig. 7c, e). The p band center of the supported MgO sheet is actually governed by the interfacial charge transfer. The MgO overlayer donates electrons to the metal substrate, because of the lower lying of the Fermi level of metal substrate than the VBM of freestanding MgO sheet. More pronounced electron transfer leads to the lower shifting of p bands of the MgO overlayer relative to the Fermi level of the whole system (Fig. 7d). Therefore, by choosing proper metal substrate, the electronic structures and adsorption properties of MgO overlayer can be finely tuned to optimize the catalytic performance.

The 2D structures of other alkaline-earth metal oxides have also been exploited for CO_2 reduction[210]. According to DFT calculations, the (100) surface of alkaline-earth metal oxides can chemisorb CO_2 molecule, with the binding strength in the order of MgO < CaO < SrO < BaO. The surface O atoms of metal oxides form chemical bond with the C atom of CO_2 in the bent configuration. Placing SrO monolayer on the anatase TiO$_2$(001) surface leads to dramatic enhancement in CO_2 adsorption and activation compared to the bare TiO$_2$ surface. Meanwhile, desorption of CO from the SrO overlayer is easier, making CO_2 reduction to CO more efficiently than that on the bare TiO$_2$.

According to the above results, 2D metal oxides can possess balanced stability and activity. Their catalytic properties are highly tunable by the facet, number of layers, and substrate interaction. The lattice O atoms can serve as the reaction centers for CO_2 activation, water splitting, and so on, with activity governed by the O 2p states. Certainly, more experimental and theoretical studies are desired to elucidate the fundamental principles for steering the lattice O activity in various 2D metal oxides for energy conversion applications.

BORON-BASED CATALYSTS
Compared to carbon, boron is electron deficient and can carry both empty and occupied orbitals. Meanwhile, resembling transition metal elements, boron holds the capability to
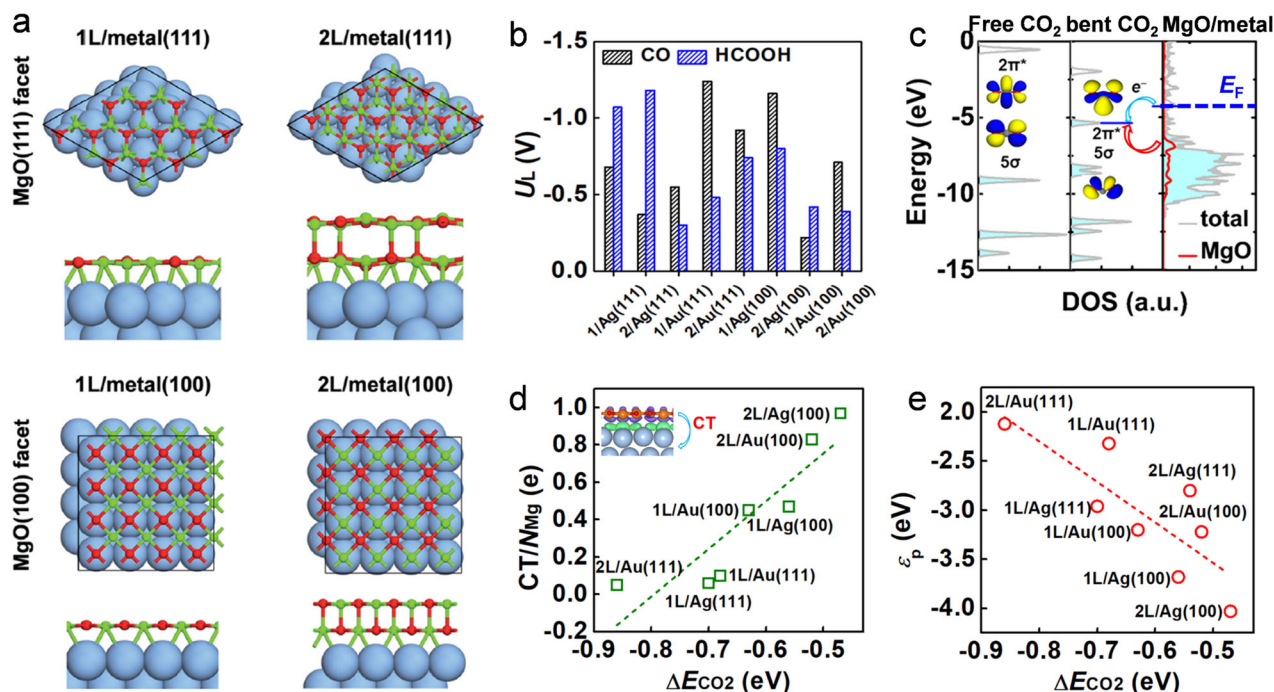
Fig. 7 CO₂ reduction on metal-supported MgO. a Top- and side-view structures of 1L and 2L MgO on the (111) and (100) surfaces of Ag and Au substrates, respectively. **b** Limiting potentials (U_L) of CO₂ reduction to produce CO and HCOOH for various metal-supported MgO overlayers. **c** DOS of a free CO₂ molecule, a bent CO₂ molecule, and MgO/metal heterostructure, respectively. **d, e** Charge transfer per Mg atom from MgO sheet to the substrate (CT/N_{Mg}) and *p*-band center (ε_p) vs. CO₂ adsorption energy (ΔE_{CO_2}) (images are adapted from ref. [209], Copyright© The Royal Society of Chemistry 2020).

participate in both electron-withdrawing ("pull") and electron-donating ("push") types of interaction, and thus exhibits unique activity for the reactions such as N₂ fixation. Therefore, boron plays a special role in catalysis and has attracted tremendous interests[3]. For instance, borylene and borylene compound molecules have been proven to be highly active for N₂ reduction for ammonia synthesis[211,212]. In this section, we will focus on the low-dimensional boron-based catalysts, including dispersed B atoms anchored on 2D materials, elementary 2D boron sheets, boron compounds (2D boron nitride and phosphide, 1D nanotubes, and 0D cages of boron nitride), and transition metal borides for energy conversion. The mechanisms and strategies for activating the B atoms in various coordination environments, and the principles for manipulating their catalytic behavior will be addressed.
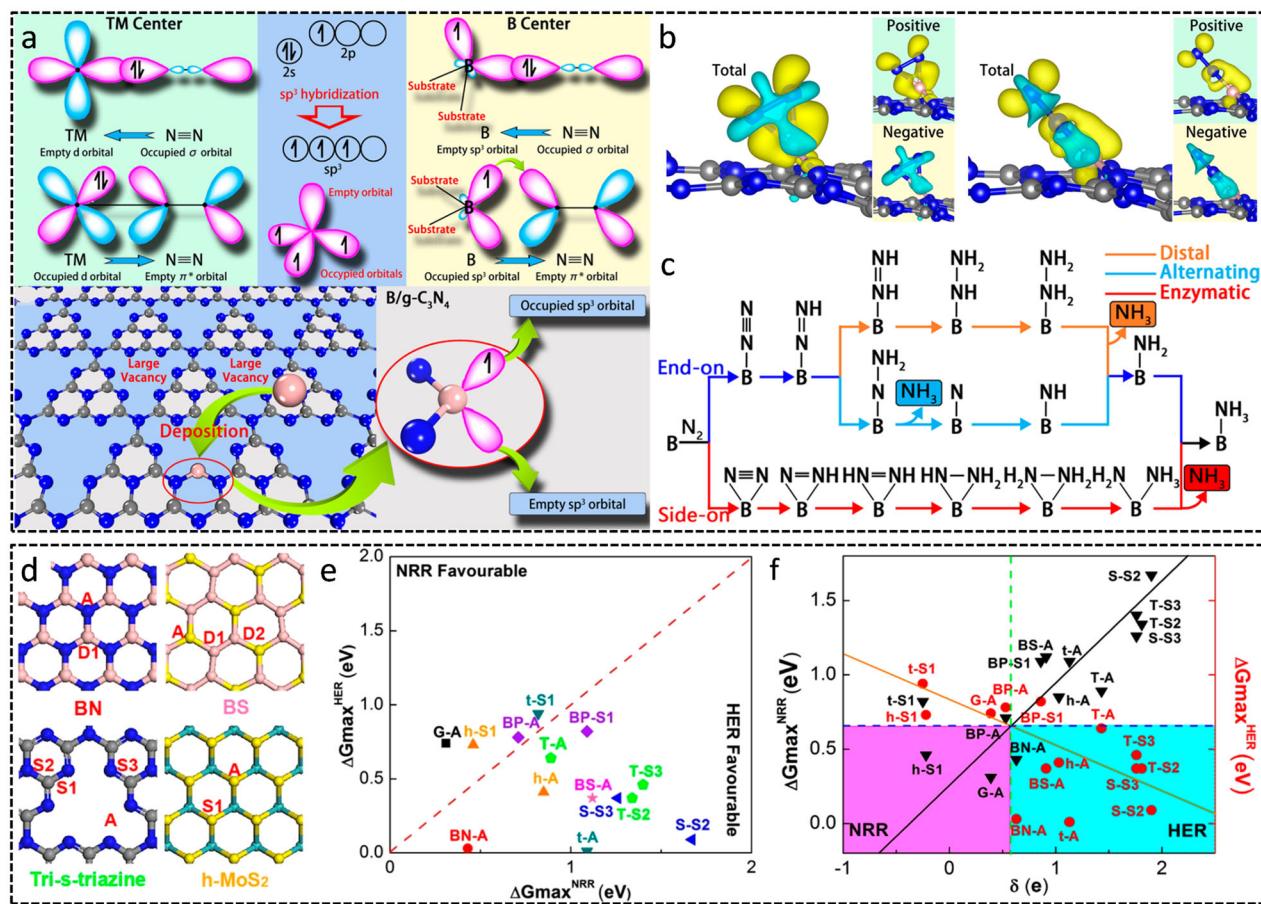
B-decorated 2D materials

The success of single-atom catalysts based on various transition metal elements stimulates the exploration of non-metal atoms as alternative catalysts for energy conversion. Among *p*-block elements, boron with the electron-deficiency character resembles transition metal elements most, and hence has aroused tremendous attention from both experimental and theoretical aspects. A pioneering theoretical study on B single-atom catalyst has been done by Ling and co-workers[213]. They proposed that a B atom in sp^3 hybridization, which simultaneously carries occupied and empty orbitals, can bind N₂ molecule through a side-on pattern due to the compatibility of orbital symmetry, and thus holds the potential for N₂ fixation. They decorated 2D g-C₃N₄ semiconductor with B single atoms for photocatalysis of NRR. According to the DFT calculations, the B atom is located in-between two 2-fold-coordinated N atoms, forming two N–B bonds (Fig. 8a). The high thermal stability of such nanostructure was assessed by AIMD at 1000 K. The decorated B atom forming sp^3 bonds with two adjacent N atoms provides one occupied and one empty sp^3 orbital to enable the "acceptance–donation" charge transfer with

N₂ molecule. As a result, it interacts strongly with N₂ having the adsorption energy of −1.04 and −1.28 eV for side-on and end-on adsorption configuration, respectively (Fig. 8b). Efficient NRR proceeds on the B atom anchored on g-C₃N₄ through the enzymatic mechanism (Fig. 8c), involving a low onset potential of 0.20 V. Moreover, B decoration notably enhances the visible light absorption of g-C₃N₄ owing to the reduction of band gap to 1.12 eV from 2.98 eV for pristine g-C₃N₄ calculated by the HSE06 functional. Therefore, the dispersed B atoms not only provide active sites for NRR, but also boost solar energy harvesting for the semiconductor substrate.

Following the above prediction, the NRR electro- or photo-activity of B atom dispersed on other 2D porous carbon nitrides has also been explored in theory[214–219]. For instance, Lv et al. showed that B single atom can stably adsorb at the hole edge of g-CN monolayer, which promotes NRR under the enzymatic pathway involving a low overpotential of 0.15 V and a small kinetic barrier of 0.61 eV, along with prohibited HER side reaction and enhanced visible light absorption[220]. Remarkably, decoration of B single atom on g-CN reduces the exciton binding energy to 0.62 eV compared with 1.08 eV for pristine g-CN, which may prevent the recombination of photoexcited carriers due to the weakened electron-hole Coulomb interaction. Moreover, the carrier effective mass of g-CN is much reduced, indicating the faster migration of photogenerated carriers to the surface to participate in NRR, which would in turn benefit efficient photocatalysis. Single B atom anchored on C₂N monolayer has also been proposed to have high activity for N₂ photoreduction, with the same reaction mechanism and similar overpotential as that of B atom on 2D g-C₃N₄ and CN[215]. The B atom staying in-between two neighboring N atoms at the hole edge of C₂N monolayer induces a magnetic moment of 1 μ_B, which is mainly localized on the B atom and plays an important role in N₂ activation. In another study, Yin et al. showed that the B atom on C₂N monolayer may also stay in-between two C atoms at the hole

Fig. 8 B-decorated 2D materials for NRR. a Simplified schematic of orbitals of N_2 bonding to transition metals and the design concept of B/g-C_3N_4 as a photocatalyst for N_2 fixation. **b** Difference charge density of B/g-C_3N_4 with the adsorption of N_2 via side-on and end-on patterns. **c** Schematic depiction of distal, alternating, and enzymatic mechanisms for N_2 reduction to NH_3 (**a**–**c** are reproduced with permission from ref. [213], Copyright© American Chemical Society 2018). **d** Proposed 2D materials and potential B-sites. **e** Computational screening of 14 catalyst combinations by the selectivity (ΔG_{max}^{HER} vs. ΔG_{max}^{NRR}). **f** ΔG_{max}^{HER} and ΔG_{max}^{NRR} vs. Bader charge (δ) for single B atom in or on a 2D substrate (**d**–**f** are adapted from ref. [226], Copyright© American Chemical Society 2019).

edge, which is sp^2 hybridized and can effectively suppress the competing HER process[221].

Encouragingly, Wang et al. fabricated B-doped g-C_3N_4 by a facile thermal treatment approach in laboratory and verified its outstanding photocatalytic performance for NRR[222]. The successful incorporation of B atoms in g-C_3N_4 nanosheets was confirmed by the FTIR and XPS characterizations, and a B doping content of 13.8 wt% was achieved. Enhanced visible light absorption and suppressed recombination of photogenerated carriers were observed in the B-doped g-C_3N_4. The measured NH_3 yield rate is 313.9 μmol g^{-1} h^{-1}, nearly 10 times of that for pristine g-C_3N_4.

Besides 2D carbon nitrides, B single atom anchored on other 2D materials such as phosphorene, group III monochalcogenides, and transition metal dichalcogenides (TMDs) for NRR electrocatalysis has also been theoretically proposed[223–225]. Liu et al. systematically investigated the catalytic behavior B atom on various 2D materials[226]. Eight kinds of 2D materials have been considered, including graphene, boron nitride (BN), boron sulfide (BS), boron phosphide (BP), black phosphorus, S-stiazine based and tri-s-triazine based g-C_3N_4, H-MoS_2, and T-MoS_2 monolayers, which provide a total of 21 possible configurations for B doping (Fig. 8d). DFT calculations suggested that the B atom substituted into H-MoS_2 and B atom adsorbed on graphene exhibit high NRR activity through the distal pathway, with low overpotentials and small kinetic barriers of 0.31 and 0.46 eV, respectively, as well as suppressed HER side reaction (Fig. 8e). Bader charge analysis

indicated that the supported B atoms carrying small or even negative charge density tend to have both high activity and selectivity for NRR (Fig. 8f).

On the experimental aspect, electrochemical NRR in the aqueous solution has been achieved in B-doped carbon materials at ambient conditions[227–230]. Yu et al. synthesized B-doped graphene by thermal annealing of graphene oxide and boric acid[227]. Compared with the pristine graphene, B doping at a concentration of 6.2% leads to significantly enhanced NRR performance with a high NH_3 production rate of 9.8 μg h^{-1} cm^{-2} and a faradic efficiency of 10.8% at −0.5 V. Later, co-doping of B and N in carbon materials has been demonstrated to further improve the NRR activity compared with the singly doped systems. Kong et al. prepared B and N co-doped porous carbon nanofiber by an electrospinning and calcination strategy[228]. The sample exhibits superior electrocatalytic performance for NRR in an alkaline electrolyte with a high faradic efficiency of 13.2% at −0.5 V and a NH_3 yield rate of 32.5 μg h^{-1} mg$_{cat.}^{-1}$ at −0.7 V. Comparison between co-doped and B/N singly doped systems suggested that B atoms efficiently enhance N_2 adsorption, and N atoms promote the electron conductivity and charge transfer kinetics.

The B-doped 2D TMDs for electrochemical NRR has also been realized in the experiment. Guo et al. synthesized B-doped MoS_2 nanosheets for NRR, which yield an excellent NH_3 production rate of 44.09 μg h^{-1} cm^{-2} at −0.2 V and a Faradaic efficiency of 21.72%

in acidic aqueous electrolyte[231]. Their DFT calculations proposed that the B atom occupying the S vacancy and the adjacent Mo atoms form a strong-weak electron polarization pair due to their different electron accepting and back-donating capacities, which facilitates N_2 chemisorption via N≡N bond polarization and drives the first protonation step. High NRR activity has also been observed in VS_2 nanoflowers comprising both B dopants and S vacancies in the basal plane, which exhibit a NH_3 yield of 55.7 µg h^{-1} mg^{-1} at −0.4 V and a Faradaic efficiency of 16.4% at −0.2 V[232].

Apart from 2D materials as substrates, B doping in nanodiamonds has also been reported to yield high activity for electrochemical N_2 and CO_2 reductions. Liu et al. fabricated B-doped diamond nanocones for NRR and achieved a high NH_3 yield rate of 19.1 µg h^{-1} cm^{-2} and a Faradaic efficiency of 21.1%[233]. Their DFT calculations suggested that the accumulation of surface charges on the nanotips contributes to the high activity, which can reduce the reaction free energy for N_2 dissociation on the B active sites on the (111) and (110) surfaces of diamond. B and N co-doped nanodiamonds have also been exploited for CO_2 electroreduction, showing unique selectivity for ethanol (C_2H_5OH)[234]. The B dopants enhance CO_2 capture, while the N atoms adsorb and transfer H atom during the hydrogenation process, thereby resulting in the synergistic effect.

The dispersed B atoms have also been proposed to have unique activity and selectivity for other challenging reactions, such as CO hydrogenation. Using DFT calculations, Chen et al. predicted high activity of B-decorated C_2N monolayer for CO hydrogenation to ethylene (C_2H_4) and propylene (C_3H_6) with a free energy increase of only 0.22 eV[235]. They showed that the B dopant and the host N atoms can form frustrated Lewis pairs to facilitate C–C coupling toward the formation of multi-carbon products. The B site acts as a Lewis acid to strongly capture one CO molecule, while the N site serves as a Lewis base to push another CO molecule to couple with the first CO. In another study, Chen et al. predicted that B doping in phosphorene can also endow unique selectivity for CO hydrogenation to yield value-added chemicals, such as CH_4, CH_3OH, and C_2H_4[236]. Under compressive strains, the unoccupied p-orbital level of B-dopant is shifted, leading to the modulation of activity and product selectivity. All these extensive experimental and theoretical studies suggest the feasibility and great promise of B single atom catalysts. Choosing appropriate substrate offers a large degree of freedom to modulate the catalytic property of dispersed B atoms for various energy conversion processes.

Elementary 2D materials of boron
The 2D elemental form of boron, namely borophene, has received great research attentions owing to their diverse structures and rich physical properties[237]. Different from graphene with a honeycomb lattice, borophene typically comprises triangular and hexagonal holes due to the electron-deficiency nature of boron. A variety of stable phases of borophene have been predicted in theory, most of which exhibit metallic behavior[238–242]. On the experimental side, several phases of borophene have been grown on Cu, Ag, Au, Ir, and Al substrates[243–249]. Benefited from its unique holey structures, borophene has been proposed to anchor various transition metal and non-metal single atoms, which are able to catalyze several energy conversion processes[250–253].

Moreover, borophene sheets in several phases have been predicted to possess intrinsic activity[254]. Shi et al. theoretically investigated the HER electrochemical activity of β12, χ3, and trigonal phases of borophene, which have been synthesized in the laboratory[255]. DFT calculations showed that all these phases of borophene can provide active sites for HER with ΔG_{H*} close to zero. Placing borophene on Ag(111) substrate can even enhance the HER performance due to the competitive effect of mismatch strain and charge transfer. The partial density of states (PDOS) of B

p_z orbital revealed that the occupancy of valence band gradually decreases as the H* binding strength at the B site increases, due to the less occupancy of the antibonding orbital with H* adsorbate and subsequently weaker H–B bond strength. In another study, Liu et al. predicted that the α phase of borophene, which is the most stable phase in theory, has high NRR electrocatalytic activity than the experimentally synthesized $β_{12}$ sheet[256]. The hexagonal triangular B atoms are identified as the active site, with the first protonation step as the rate-determining step requiring an energy of 0.77 eV. Depositing on Cu and Ag substrates can further improve the NRR activity due to the electron injection from the substrate to borophene sheet. Besides, the β12 and χ3 borophene have been proposed as electrocatalysts for CO_2 reduction to selectively produce CH_4, with a limiting potential of −0.27 V and the largest kinetic barrier of 0.98 eV[257].

Experimentally, electrochemical NRR in 2D boron-based nanosheets has been realized by several groups. Qiu et al. prepared B_4C nanosheets by liquid exfoliation of bulk B_4C, whose structure is built up of boron clusters connected by C atoms[258]. The TEM images confirmed the formation of few-layer B_4C nanosheets. An average NH_3 yield rate of 26.57 µg h^{-1} $mg_{cat.}^{-1}$ was achieved with a high Faradaic efficiency of 15.95% at 0.75 V (vs. RHE) in the acidic electrolyte. According to the DFT calculations, N_2 molecule can be chemisorbed in both end-on and side-on configurations on the B_4C(110) surface, with the vertical B atoms on the boron clusters serving as the active sites. The rate-limiting step of NRR is the protonation of NH_2* to form NH_3, requiring an energy of 0.34 eV

Few-layer nanosheets of β-boron stably dispersed in six organic solvents have been obtained by Fan et al. for N_2 electroreduction[259]. They achieved a low onset overpotential (<0.15 V), a high NH_3 yield rate of 3.12 µg h^{-1} $mg_{cat.}^{-1}$, and a Faradaic efficiency of 4.84% under −0.14 V, nearly twice higher than that of bulk boron. STEM revealed that the exfoliated boron nanosheets well preserve the crystalline structure of bulk boron with uniform arrangement of boron icosahedra. DFT calculations suggested that the icosahedron B atoms on (104) and (021) surfaces, which are the two most dominant facets observed in the experiment, serve as the active sites for NRR by providing strong binding with N_2 molecule and promoting the reduction reaction with small energy cost (below 0.39 eV). The enhancement of NRR activity in the boron nanosheets relative to the bulk counterpart has also been observed by Zhang and co-workers[260]. The XPS measurement indicated the presence of oxidized B atoms in the nanosheets. According to the DFT calculations, the B atoms on (104) surface in both oxidized and H-deactivated forms have higher NRR activity than that on the clean surface.

More theoretical insights into the NRR activity of boron nanosheet have been provided by Jiang and co-workers[261]. They examined the (001) surface of rhombohedral α-boron, which is a layered structure composed of B_{12} units and has the common σ bonds and three-center two-electron bonds. Bader charge analysis showed that the charge distribution in α-B_{12} is amphoteric, with the surface B atoms carrying negative charges and the B atoms beneath the surface carrying positive charges. As a result, the surface B atoms strongly bind with N_2 molecule, and electrochemical NRR proceeds through the enzymatic mechanism with a low limiting potential of 0.36 V. The above experimental and theoretical results manifest that the elemental boron nanostructures are potential metal-free catalysts with special activity for NH_3 synthesis.

Boron nitride nanostructures
Boron nitride, as an important compound form of boron, exists in diverse structures, such as bulk BN of cubic and hexagonal phases, 2D h-BN, 1D BN nanotubes (BNNTs), and 0D BN nanocages. They usually possess excellent stability against oxidation, heat, and

corrosion, which are great merits for industrial applications. Hence, activation of BN-based materials for catalytic reactions is highly desirable. Many experimental and theoretical efforts have been devoted to inducing activity in various BN nanostructures by strategies such as introducing defects and edges, heteroatom doping, chemical functionalization, and hybrid with transition metals.

Uosaki et al. performed a proof-of-concept study to show that the inert h-BN monolayer can be activated by depositing on Au (111) substrate[262]. Their DFT calculations disclosed a metastable adsorption state of O_2 molecule on Au(111)-supported h-BN monolayer with an adsorption energy of −0.05 eV, where O_2 binds to two B atoms nearest to the N atom sitting on top of Au atom in the first metal layer. This metastable configuration for O_2 adsorption serves as the precursor for ORR electrocatalysis, making the reduction reaction possible via the two-electron pathway to form H_2O_2 or via the four-electron pathway to generate H_2O. Then, the ORR electrochemical activity of a gold electrode modified by mono- and few-layer h-BN was examined by experiment. It was shown that the overpotential for ORR is reduced upon modification by ca. 0.27 V, which verifies the theoretical prediction.

Later, the ORR activity of 2D h-BN supported on various transition metal substrates was theoretically investigated by Koitz and co-workers[263]. Their calculations suggested significant influence of metal substrate on the reaction energetics for the supported h-BN monolayer. Monolayer h-BN on Cu(111) surface has high activity for ORR electrocatalysis with an overpotential of 0.34 V, comparable to that on Pt(111). For Co(0001) and Ni(111) substrates, binding of OH* species on the supported h-BN monolayer is over-strong, which impedes efficient ORR.

Boron nitride nanotubes encapsulating transition metals provide another kind of model systems for investigating the effects of both metal filling and curvature of BN surface on the activity. Actually, BNNTs stuffed with guest molecules, clusters, and nanowires of transition metals (Fe, Co, Ni, Cu), noble metals (Ag, Au, Pt, Pd), and post-transition metals (Al, In) have been widely synthesized in laboratory[264–267]. By DFT calculations, Zhou et al. predicted that encapsulating early transition metal (such as Ti, Zr, V, Cr, and Sc) nanowires into single-wall BNNTs can induce activity of the surface B atoms for N_2 fixation (Fig. 9a)[268]. The activity originates from the strong electronic coupling between BNNT and the metal filler. The metal nanowires donate electrons to BNNT, which destructs the π conjugation of BN network and liberate the p_z orbitals of B atoms. The partial occupancy of B p_z orbitals enables donation and back-donation of electrons with N_2 molecule (Fig. 9b), such that N_2 can chemisorb on the two neighboring B atoms in the side-on configuration (Fig. 9c). The adsorption strength of N_2 is related to the energy level and occupancy of B p_z orbitals, which can be controlled by the type of metal filler and the diameter of nanotube. By microkinetic modeling, the Ti encapsulated BNNT with a diameter about 1 nm was predicted to have the maximal turnover frequency for NH_3 production, with the energy diagrams and reaction pathways of N_2 hydrogenation on Ti/BNNTs presented in Fig. 9g. The electronic structure-activity relationship of the metal-encapsulated BNNTs can be described by their work function (Fig. 9d, e), which reflects the p_z orbital level of B atoms, as the DOS emerging at the Fermi level upon metal encapsulation are mainly from the B p_z states (Fig. 9f). The encapsulated BNNTs with smaller work function have the Fermi level closer to the π* state of N_2, and thus donate electrons to N_2 more readily and provide stronger binding with N_2. Such correlation can be regarded as another form of the "p band model" proposed for the carbon-based hybrid catalysts described in the section "Hybrid catalysts of graphitic carbon and transition metal-based materials", suggesting a general rule for regulating the activity of non-metal materials by steering their p orbitals.

Embedding transition metal atom or cluster into BN nanocage can also activate the surface B atoms. Yang et al. proposed to encapsulate a $B_{36}N_{36}$ nanocage with a transition metal tetramer (M_4) for solar-driven N_2 fixation and considered a series of early and middle transition metal elements, including Sc, Ti, V, Cr, Y, Zr, Nb, Mo, Hf, Ta, and W[269]. Similar to the metal-filled BNNTs, the electron transfer from the M_4 cluster to the $B_{36}N_{36}$ nanocage leads to partial filling of B p orbitals, and endows the B atoms with strong binding capability with N_2 molecule. $Mo_4@B_{36}N_{36}$ was found to have the highest activity for N_2 reduction, with an onset potential of −0.19 V. In addition, metal encapsulation of $B_{36}N_{36}$ nanocage leads to broad-band light absorption in the ultraviolet, visible and infrared regimes, owing to the large number of excitation states induced by the metal filler. Therefore, the encapsulated $B_{36}N_{36}$ nanocages may harvest a large portion of sunlight to further promote the NRR catalysis.

Besides mixing with transition metals, the edges and defects of BN nanostructures were created to trigger activity in laboratory. Zhang et al. synthesized h-BN nanosheets by liquid exfoliation of bulk h-BN powders[270]. In the acidic solution, the h-BN nanosheets were able to electrocatalyze NRR at ambient condition attaining a high NH_3 formation rate of 22.4 μg h^{-1} mg$_{cat.}^{-1}$ and a high Faradaic efficiency of 4.7% at −0.75 V, with excellent stability and durability. The HRTEM image showed that the (100) surface of h-BN nanosheets is exposed, which corresponds to the zigzag edge of the layered structure. According to DFT calculations, the unsaturated B atoms at the zigzag edge of h-BN sheet can strongly adsorb N_2 molecule, and promote NRR under the distal and enzymatic dissociative pathways involving an energy step of 0.60 eV. Mesoporous BN and defective BN nanosheets have also been reported to exhibit strong long-term electrochemical durability and excellent electrocatalytic activity for NRR owing to the more abundant exposed active sites[271,272].

The catalytic mechanism of 2D h-BN edges for NRR has been further addressed by Lee et al. from the theoretical point of view[273]. They showed that the zigzag edge of h-BN monolayer, when the exposed B atoms at the edge are hydrogenated, can promote N_2 hydrogenation for NH_3 production. The H functional group induces local conversion between sp^2 B and sp^3 B sites at the edge, which facilitates the hydrogenation of N_2. By microkinetic modeling, the NH_3 yield at a temperature of 1500 K was estimated to be 6.6 μg h^{-1} mg$_{hBN}^{-1}$ for h-BN nanoribbons with a width of 2 nm. Decoration of h-BN edge with single B atom can also induce activity for NRR. Mao et al. showed that a single B atom anchored at both zigzag and armchair edges can act as the reaction center for NRR electrocatalysis, with an overpotential of only 0.13 V under the distal pathway[274]. As a unique advantage, the zigzag edge decorated by B atoms provides strong binding with N_2 but weak binding with NH_3, with the adsorption energy of −1.25 and −0.35 eV, respectively. As a result, the NH_3 product can be readily released from the catalyst, which would be beneficial for the durability and stability of the electrocatalysts.

Inspired by the promising catalytic performance of BN-based materials, the electrochemical activities of BP and boron arsenide (BAs) have also been explored. Using DFT calculations, Chen et al. investigated different surfaces of cubic BP and BAs for NRR, including (100), (110), and (111) facets[275]. They showed that B-terminated (111) polar surfaces of BP and BAs exhibit prominent electronic states near the Fermi level. Each surface B atom forms three covalent bonds with the neighboring P or As atoms, leaving one empty orbital and thus enabling the donation and back-donation with N_2 molecule. As a result, the (111) surface of BP and BAs provides strong binding with N_2 and can effectively reduce it to NH_3 via the enzymatic pathway with low limiting potentials of −0.12 and −0.31 V, respectively. Meanwhile, the undesired HER side reaction is inhibited on these B-rich surfaces.

On the experimental aspect, boron phosphide has been indeed exploited for energy conversion. Mou et al. fabricated BP
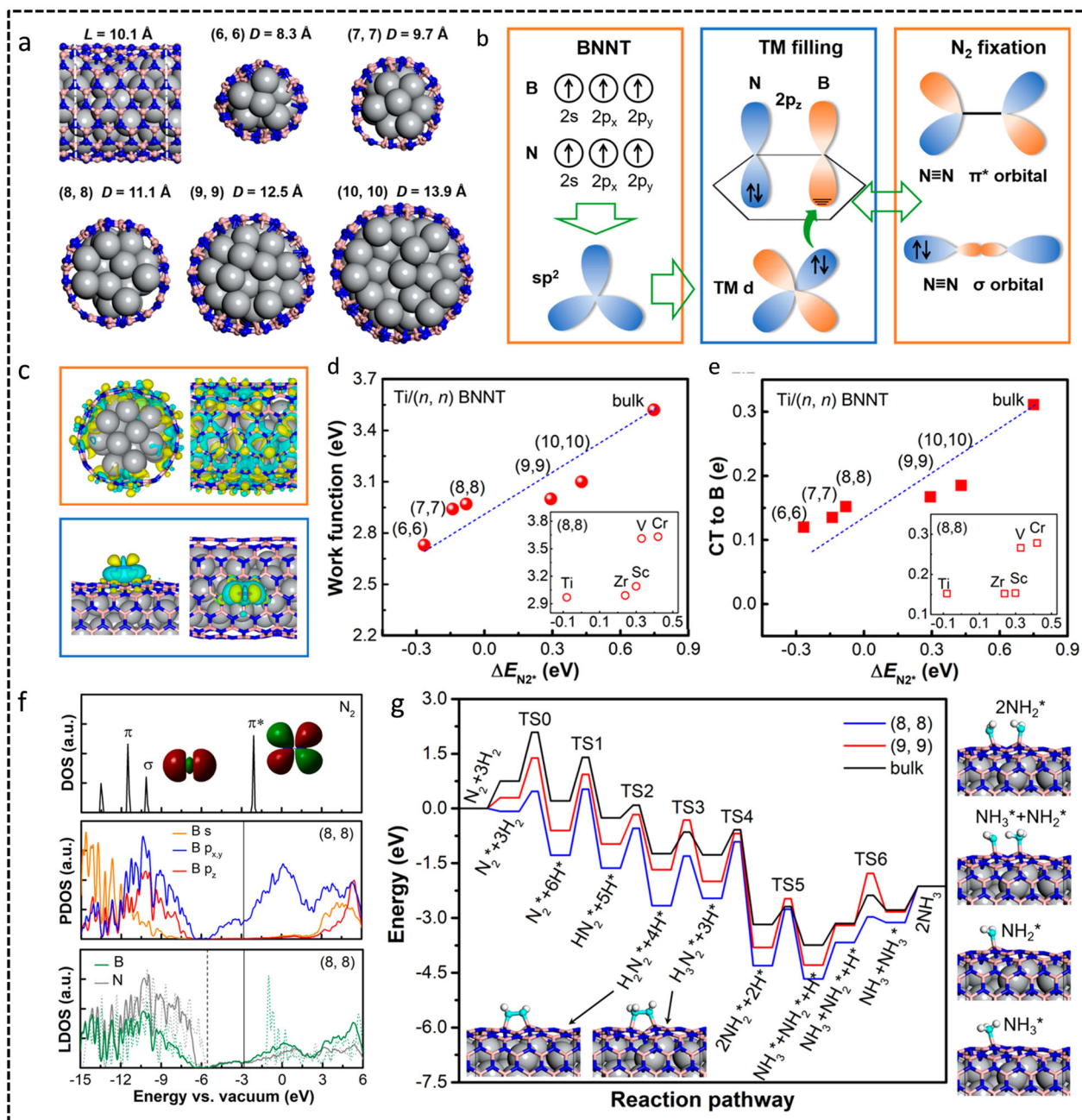
Fig. 9 Metal-encapsulated boron nitrogen nanotubes for NRR. a Side-view and top-view structures of Ti encapsulated BNNTs with various tube diameters. **b** Mechanism of activation of BNNTs by metal encapsulation for N_2 fixation. **c** Differential charge density distributions of Ti/(8, 8) BNNT and a N_2 molecule chemisorbed on it. **d** Work function and **e** charge transfer (CT) from metal nanowire to each B atom in BNNTs as a function of N_2 adsorption energy (ΔE_{N2^*}) for Ti/(n, n) BNNT as well as bulk Ti/h-BN heterostructure. **f** DOS of a free N_2 molecule (top panel), PDOS of B atoms in Ti/(8, 8) BNNT (middle panel), and LDOS of B and N atoms in Ti/(8, 8) BNNT (bottom panel). **g** Energy diagram of N_2-to-NH_3 conversion on Ti/(8, 8) BNNT, Ti/(9, 9) BNNT, and bulk Ti/h-BN heterostructure (imaged are reproduced with permission from ref. [268], Copyright© American Chemical Society 2019).

nanoparticles of cubic phase, which exhibit high activity and selectivity for electro-reduction of CO_2 to CH_3OH, with a Faradaic efficiency of 92.0% at −0.5 V and a CH_3OH yield rate of 127.5 μg h^{-1} mg$_{cat.}$$^{-1}$ at −0.6 V[276]. Their DFT calculations revealed that CO_2 molecule is strongly adsorbed on the exposed B atoms on BP(111) surface, with an adsorption free energy of −1.38 eV. The rate-determining step for CO_2 reduction to CH_3OH is the protonation of OH* to form adsorbed H_2O* species, involving an energy step of 1.36 eV in the free energy diagram. Charge analysis suggested that the interior P atoms donate electrons to the surface B atoms,

thereby synergistically promoting the CO_2 activation and reduction.

Apart from BN and BP nanostructures, 2D boron carbonitride (BCN) and 2D COFs are also possible forms of boron-containing materials with certain activity. Liu et al. prepared B-rich COFs and achieved high NRR activity with a Faradaic efficiency of 45.43% through electrochemical excitation[277]. Combining experimental characterization and DFT simulations, they disclosed that the B atoms in COFs serve as the active sites for N_2 fixation. In particular, the COFs undergo an evident transformation from the crystalline

to amorphous phase under the electrochemical process. Such reconstruction further facilitates N_2 diffusion and adsorption in the catalyst. Taking advantage of the "Lewis acid" character of boron, a series of BCN materials were designed and synthesized by Chang and co-workers[278]. Their DFT calculations indicated that the B atoms in BCN are more likely to lose electrons to the adjacent N and C atoms, forming local electron-deficient environment and thus offering a strong binding site for a Lewis base (N_2). Therefore, by adjusting the B:N ratio, the "Lewis acid catalysis" sites can be tuned, and a high-performance B-enriched BCN electrocatalyst was obtained with a high NH_3 yield of -41.9 μg h^{-1} mg$_{cat.}^{-1}$ and a Faradaic efficiency of 9.87%. All these experimental and theoretical studies shed light on utilizing the abundant and inexpensive boron compound nanomaterials for electro-, photo-, and thermal catalysis, and provide essential physical insights for precisely tailoring their activities by band structure engineering.

Transition metal borides nanostructures

Transition metal borides remain exotic for scientists due to their relatively difficult synthesis compared with other transition metal compounds, such as transition metal oxides, carbides, and chalcogenides. The unique bonding nature between metal and B atoms renders transition metal borides a huge compositional and structural diversity[279]. With recent progress in synthesis technology, rich forms of transition metal boride nanomaterials have been obtained, showing great promise for energy conversion, such as electrochemical NRR and water splitting[280,281]. By choosing proper transition metal elements in metal borides or adjusting the atomic ratio of bimetal borides, the activity can be optimized, indicating the key role of metal species in the catalysis[282,283]. Intriguingly, the presence of B atoms also notably affects the electrochemical performance of these transition metal compounds. For instance, the HER activity of different phases of molybdenum borides (Mo_2B, α-MoB, β-MoB, and MoB_2) have been compared in the experiment, showing strong dependency on the B content[284]. The B-rich MoB_2 and β-MoB were found to have the highest activity in the acidic solution, while Mo-rich Mo_2B showed the lowest activity for HER. Nickel borides and cobalt borides with different B contents have also been considered for HER electrocatalysis[285]. The NiB and $CoB_{0.71}$ with high B content were found to exhibit the lowest HER overpotential in the alkaline medium. These experimental observations signify the intrinsic activity for both metal and B atoms, and thus have attracted many theoretical efforts for mechanistic understanding.

Liu et al. performed a mechanistic study on the activity of a series transition metal borides for NRR electrocatalysis[286]. Using DFT calculations, they examined B-terminated (001) surfaces of Mo_2B, α-MoB, and MoB_2, and confirmed the stability of these B exposed surfaces (Fig. 10a). Mo_2B was found to have a unique surface structure with isolated B atoms embedded in the lattice without bonding with the neighboring B atoms on the surface (Fig. 10b). The isolated B site endows Mo_2B the highest NRR activity among different molybdenum borides, with a limiting potential of -0.82 V. This concept of isolated B sites can be extended to the other transition metal borides (M_2B, M = Ti, Cr, Mn, Fe, Co, Ni, Ta, and W), among which Fe_2B and Co_2B with the same surface structures were also screened with relatively low limiting potential of -0.75 and -0.84 V for NRR, respectively (Fig. 10d). Electronic structure analysis revealed that the filling degree of p_z-orbital of B active sites in the transition metal borides governs the N_2 adsorption strength (Fig. 10c). When B p_z orbital is less filled (as in the case of Mo_2B), N_2 binding is stronger and N≡N triple bonding is weaker.

In another theoretical study, Qin et al. proposed that transition metal diborides, such as TiB_2, VB_2, and NbB_2, have superior activity and selectivity for N_2 electro-reduction[287]. The reduction process occurs via the associative or dissociative Heyrovsky mechanism.

VB_2 was predicted to be the most efficient electrocatalyst with a low limiting reaction energy of 0.28 eV. Then, ZrB_2 nanocubes with layered structures have been synthesized in the experiment, which achieve attractive NRR performance with a NH_3 yield of 37.7 μg h^{-1} mg^{-1} and a Faradaic efficiency 18.2% at -0.3 V[282]. Their DFT calculations revealed that the surface Zr centers enable effective activation of N_2 molecule via a unique tetranuclear side-on mode, which lowers the reaction energy barrier and concurrently impedes the undesired HER by restricting H* adsorption. Besides, amorphous FeB_2 and NiFeB nanosheets have been reported to exhibit outstanding performance for electrocatalysis of NRR[283,288]. The activity can be effectively modulated by adjusting the morphology and chemical composition of the metal borides.

The 2D form of transition metal borides, namely MBenes, provide an excellent platform for understanding the fundamental rule for activity tuning of boride materials, owing to their outstanding electrical conductivity, high stability, and well-defined surface structures without termination by functional groups as indicated by experimental characterization[289]. So far, a variety of stable phases of MBenes with different chemical compositions and structural patterns have been predicted, and some of them have been realized in laboratory. Both metal and B atoms can be exposed on the MBene surfaces, thus offering the opportunity for clarifying the impacts of metal and B sites on the catalytic performance. Yang et al. systematically explored the NRR electrochemical activity of ten kinds of MBenes by DFT calculations (Fig. 10e)[290]. The outstanding stability of MBenes in the aqueous solution at room temperature was confirmed by AIMD simulations. Both metal and B exposed surfaces of MBenes provide strong binding with N_2 molecule and can effectively suppress the HER side reaction. In particular, OsB_2, FeB_2, and RuB_2 with B exposed surfaces exhibit superior NRR activity compared to the metal active sites, having much lower onset potentials of -0.03 to -0.26 V. The co-existed B and metal atoms both carrying occupied and unoccupied p/d states cooperatively serve as electron reservoirs with large adaptability to interact with the reaction intermediates. The total number of empty p orbitals of B atoms and empty d orbitals of metal atoms in MBenes follow a volcano relation with the NRR onset potential. In addition, the N_2 binding strength and onset potential show an approximately linear relationship with the work function of MBenes (Fig. 10f), which actually reflects the frontier orbital levels of the surface atoms of MBenes as they dominate the DOS near the Fermi level. Overall, MBene with larger work function exhibits weaker binding capability with N_2 and lower NRR onset potential. Therefore, these established electronic structure-activity relations provide an important clue for optimizing the NRR activity of MBenes by choosing appropriate chemical composition and work function.

The electrocatalytic properties of MBenes for NRR have also been theoretically investigated by Guo et al.[291]. The advantages of high NRR activity and unique selectivity against HER were also confirmed for 16 kinds of MBenes, which mainly have the metal exposed surfaces as the active sites. Moreover, the surface Pourbaix diagram suggested that these MBene surfaces, once covered by O* and OH* oxygenated species, can be reduced to H_2O under the reaction conditions. Thus, MBenes with the antioxidation nature may hold great promise for pH-universal electrocatalysis of NRR for NH_3 production.

To summarize this section, boron is of great interest for catalysis owing to its electron-deficiency nature and thus the capability to carry both filled and empty orbitals that can mimic transition metal d orbitals. Boron in the forms of dispersed atoms, elemental 2D sheets, and compound nanostructures possess superior activity for various energy conversion processes. Even the intrinsically inert boron nitride sheets and nanotubes can be effectively activated by mixing with transition metals. In particular, the presence of empty or partially filled p orbital of B atom endows it
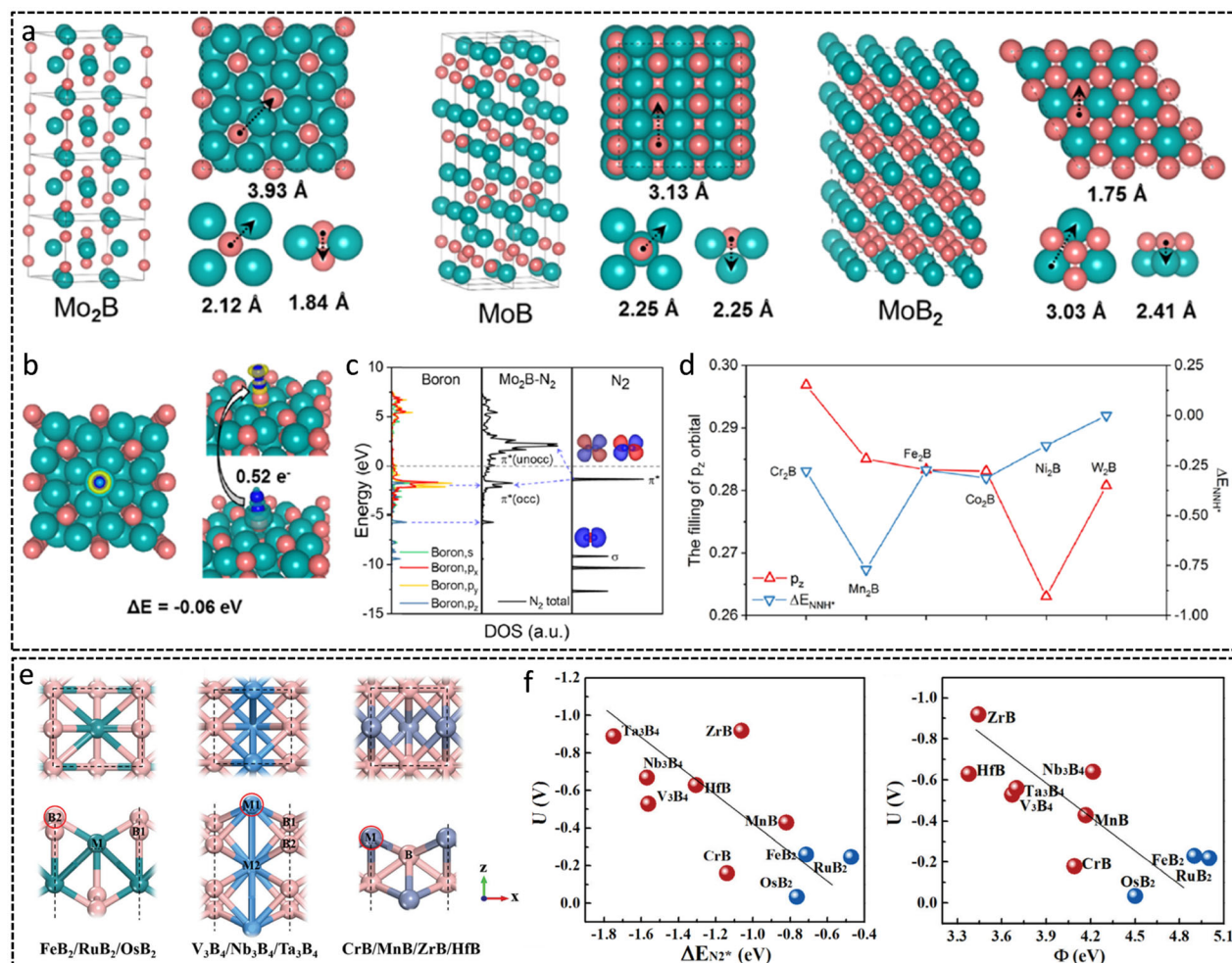
Fig. 10 Transition metal borides for NRR. a Crystal structures of Mo$_2$B, α-MoB, and MoB$_2$. **b** Charge density difference of end-on N$_2$ adsorption on Mo$_2$B. **c** PDOS and schematic illustrations of B orbitals of molybdenum borides, π*-orbitals of the N$_2$ gas molecule, and their interactions with Mo$_2$B. **d** Relationship between the filling of B p_z-orbital and the adsorption energy of *NNH (**a–d** are reproduced with permission from ref. [286], Copyright© American Chemical Society 2020). **e** Structural prototypes of MBenes. **f** NRR onset potential vs. N$_2$ adsorption energy and work function on MBenes (**e, f** are reproduced with permission from ref. [290], Copyright© The Royal Society of Chemistry 2020).

the specialty for electron donation and back-donation with N$_2$ molecule and hence unique activity for N$_2$ fixation. The orbital energy level and filling degree of B p orbitals generally determine the activity, such that some relevant descriptors can be identified to guide the experimental optimization of the performance of these non-metal catalysts.

PHOSPHORUS-BASED CATALYSTS

Phosphorus, an abundant element in earth crust, has also attracted interest for heterogenous catalysis. Phosphorus in the form of ligands, molecules, elementary, and compound materials have been widely adopted for various chemical reactions[292–294]. Doping or alloying P into some known catalysts can effectively improve the performance, signifying the intrinsic activity of P atoms in certain valence states and coordination environments[295–297]. In this session, we will focus on 2D black phosphorus and transition metal phosphides, as they have been demonstrated as promising electro- and photo-catalysts for energy conversion. Their well-defined geometries and surface structures provide the opportunity for understanding the active sites and catalytic mechanism in the P-containing materials, and disclosing the governing rule of the

activity of P atoms in various elementary and compound nanostructures.

2D black phosphorus-based catalysts

Monolayer black phosphorus, namely phosphorene, is an easily accessible 2D semiconductor with moderate band gap, high carrier mobility, and strong visible light absorption, all of which are precious merits for photocatalysis. However, the band edge position of VBM of phosphorene is higher than the redox potential of H$_2$O/O$_2$ for water splitting, and thus the photoexcited hole carriers do not have sufficient oxidation power for OER. As a result, phosphorene can only be used as the photocathode for HER in solar water splitting cell. Meanwhile, the basal plane of pristine phosphorene lacks the activity to interact with the environmental gas molecules such as H$_2$, N$_2$, and CO$_2$, although phosphorene usually suffers from oxidation in the ambient condition. Therefore, modification of phosphorene to tailor both electronic band structure and surface reactivity is desired to achieve high photo (electro)catalytic performance.

Numerous strategies for manipulating the electronic band structure of phosphorene have been proposed in theory, including heteroatom doping, strain engineering, creation of defects and edges, chemical functionalization, and construction of

heterojunctions, such that its band gap and band edge positions can be effectively modulated to the desired ranges suitable for photocatalysis[298–302]. On the experimental aspect, high-efficiency photocatalysis of HER and NRR based on phosphorene nanosheets have been realized, with an H_2 evolution rate of 512 μmol h^{-1} g^{-1}, and a NH_3 yield rate of 102.4 μg h^{-1} $mg_{cat.}^{-1}$ and a Faradaic efficiency of 23.3% at -0.4 V, respectively[303,304]. Partial oxidation and incorporation of edges of crystalline domains in phosphorene were adopted to enhance the photocatalytic efficiency for HER and NRR, respectively[305,306]. Moreover, phosphorene can act as a co-catalyst to boost the photogenerated carrier separation and transfer at the heterojunction. A series of hybrid materials of phosphorene with CdS, ZnS, CoP, and g-C_3N_4 have been synthesized and exhibit outstanding performance for photocatalysis of HER and NRR[307–310].

Electrocatalysis of OER based on phosphorene has also been widely achieved[311]. It was shown that few-layer phosphorene nanosheets prepared by liquid exfoliation exhibit preferable electrocatalytic OER activity and structural robustness with onset potential and Tafel slope of 1.45 V and 88 mV dec^{-1}, respectively. Interestingly, reduction in the thickness of phosphorene nanosheets compliments to the OER activity, which may be ascribed to extra active sites and enlarged specific surface area[312]. Furthermore, Prasannachandran et al. synthesized phosphorene quantum dots with in situ surface functionalization by N-containing groups, and they obtained efficient and stable electrocatalytic activity for OER with an overpotential of 1.66 V at 10 mA cm^{-2} and a low Tafel slope of 48 mV dec^{-1}. They attributed the improved OER performance to the charge separation induced by the N-containing functional groups, which in turn is resulted from the electronegativity difference between P and N atoms, leading to the enhanced adsorption of OH species on the P atoms[313].

The mechanism for creating active sites in phosphorene has been explored from the theoretical point of view. Zhang et al. disclosed the role of vacancies and edges in phosphorene on the HER activity[314]. According to their DFT calculations, the odd-sized vacancies like monovacancy and trivacancy provide enhanced and optimized H* binding strength for HER electrocatalysis with $\Delta G_{H*} = -0.02$–0.14 eV and 0.07–0.11 eV, respectively. The active sites are the nearest neighbors of the dangling atom. In contrast, the divacancy in phosphorene is fully passivated with all atoms having a coordination number of three, and thus the defective phosphorene has weak H* binding with $\Delta G_{H*} = 0.69$–1.45 eV, similar to that of perfect phosphorene ($\Delta G_{H*} = 1.25$ eV). Electronic structure analysis showed that the monovacancy induces spin splitting and gives rise to a singly occupied defect level, which is responsible for the HER activity, while for the case of divacancy, there is no dangling state in the band gap. Moreover, the phosphorene edge also exhibits HER activity owing to the empty edge states highly localized at the unpassivated edge atoms. Along the ribbon width direction, the ΔG_{H*} value decreases gradually as the H* adsorption site gets closer to the phosphorene edge, and it reaches -0.02 eV when the H* species is adsorbed on the edge P atom. The authors suggested that the unique HER activity of phosphorene is attributed to the favored H–P hybridization associated with local bond distortions around the defects and partial compensation of the localized defect states by the H* species, while similar atomic vacancies in some other isostructural layered semiconducting materials are inactive.

The effect of oxygen functionalization on the OER and ORR activity of phosphorene has been theoretically explored by Feng et al.[315]. They showed that the pristine phosphorene provides too strong binding with the oxygenated intermediates involved in OER and ORR, while by oxidation functionalization, the binding capability of phosphorene can be effectively tuned to improve the electrocatalytic performance for OER and ORR. Specifically, the authors examined the phosphorene structures with different oxidation degrees and configurations, and disclosed the variation behavior of OER/ORR overpotential as a function of the local oxidation degree of phosphorene ($D_{O\,local}$). With the increase of $D_{O\,local}$, the activity first decreases and then increases, with the lowest ORR overpotential of 0.69 V achieved at a partially oxidized state ($D_{O\,local} = 3.4$), while the highest oxidation state with a chemical composition of P_2O_5 yields the lowest OER overpotential of 0.70 V.

Hybridization of phosphorene with other 2D materials such as MXene, N-doped graphene, and MoS_2 can effectively enhance the electrocatalytic activity for water splitting[316]. Zhu et al. fabricated black phosphorus quantum dots on Ti_3C_2 MXene nanosheets, which exhibit remarkable bifunctional activity for HER and OER in the alkaline media[317]. The overpotential is 360 mV with a Tafel slope of 64.3 mV dec^{-1} for OER, and the overpotential is 190 mV for HER with a Tafel slope of 83.0 mV dec^{-1} for HER, significantly lower than those of their individual components and competitive to the commercialized RuO_2 or Pt/C electrocatalysts. It was suggested that the role of MXene substrate lies in the confinement of the black phosphorus quantum dots to prevent them from aggregation, and to provide excellent electrical conductivity. Moreover, their DFT model calculations revealed that the coupling between MXene and black phosphorus quantum dot endows the interfacial P atoms with HER activity ($\Delta G_{H*} = -0.17$ eV) and strong adsorption with H_2O molecule (adsorption energy of -1.01 eV) that benefits OER. Yuan et al. coupled ultrathin black phosphorus with N-doped graphene for water electrolysis[318]. Due to the lower Fermi level of black phosphorus relative to N-doped graphene, their electronic interaction induces directional interfacial electron transfer, leading to enriched electron density on the black phosphorus sheet and positive charge density on the graphitic layer. DFT calculations showed that such electron redistribution results in enhanced H* binding on black phosphorus with $\Delta G_{H*} = 0.1$ eV. Meanwhile, the positively charged C sites on N-doped graphene promote the formation of OOH* intermediate with a reduced energy step of 0.43 eV for OER, compared with 0.51 eV for standalone N-doped graphene. This synergistic effect leads to a low cell voltage of 1.54 V at 10 mA cm^{-2} by using such non-metal nanohybrids as anode and cathode, which is even smaller than that of the costly integrated Pt/C@RuO_2 system (1.60 V).

Since P atom is isoelectronic to N atom with three electrons in the valence p orbitals, the synthetic phosphorene nanosheets, which inevitably present large number of defects during the exfoliation process, should be a potential electrocatalyst for NRR. As a proof of concept, Zhang et al. prepared few-layer black phosphorus nanosheets and achieved a Faradaic efficiency and a production rate for NRR in the acidic aqueous solution as high as 5.07% and 31.37 μg h^{-1} $mg_{cat.}^{-1}$ at -0.7 V, respectively[319]. By DFT calculations, the authors unveiled that the zigzag edge of phosphorene has a non-localized and asymmetric electron distribution, which are beneficial for N_2 adsorption. An alternating hydrogenation pathway in the association mechanism is most efficient for NRR at the zigzag sites, involving a limiting potential of 0.85 V.

The photocatalytic behavior of defective phosphorene has been investigated by Pei et al.[320] in terms of chemical reactivity, optical absorption, and photocarrier dynamics using DFT calculations and time-dependent ab initio nonadiabatic molecular dynamics (NAMD) simulations[321]. The effects of various point defects in phosphorene were examined, and the double vacancy consisting of pentagon and octagon rings denoted as the (5|8|5) defect exhibits the best photocatalytic performance (Fig. 11a). In particular, chemisorption of N_2 molecule on the phosphorene defects is endothermic, with positive adsorption energies of 0.25–1.86 eV. Nevertheless, the defects provide a metastable state for N_2 adsorption, in which the N≡N triple bond is considerably weakened as indicated by the elongated N–N bond length to 1.25–1.46 Å from 1.11 Å in the free N_2 molecule. Further
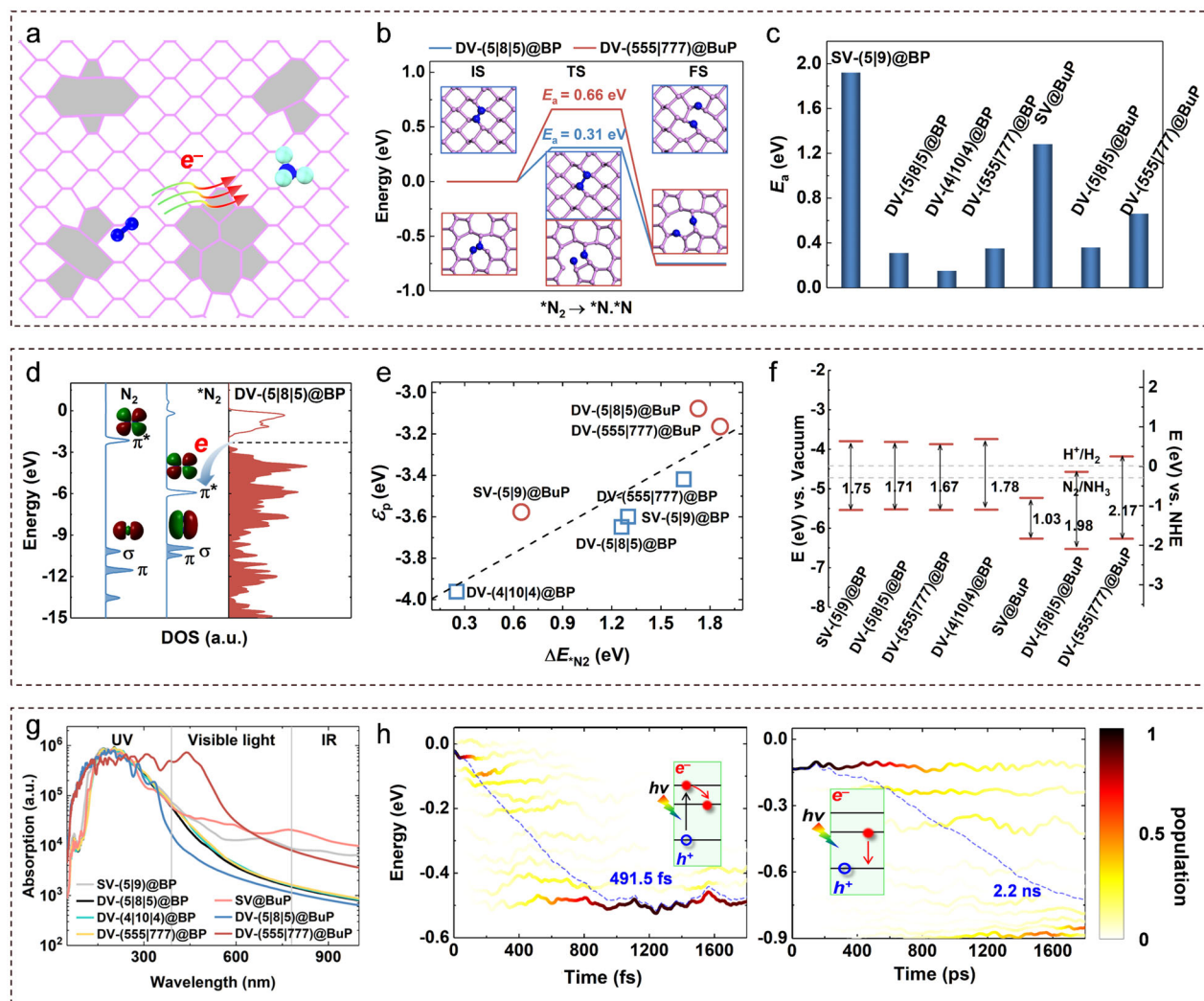
Fig. 11 Mechanism and carrier dynamics of N₂ fixation on defective black phosphorene. a Schematic illustration of N₂ fixation on the defective black phosphorene. **b** Transition states and **c** kinetic barriers of N₂ dissociation on defective phosphorene. **d** Orbital interaction between absorbed N₂ molecule and DV-(5 | 8 | 5) of black phosphorene. **e** The p orbital centers of defective phosphorene as a function of the adsorption energy of N₂. **f** Band edge positions with respect to the redox potentials of NRR and **g** optical absorption spectra of various defective phosphorene. **h** Time-dependent averaged energy evolution (blue dashed lines) of hot electron relaxation and recombination in DV-(5|8|5) of black phosphorene calculated by using the fewest switches surface hopping and decoherence induced surface hopping methods, respectively (images are adapted from ref. [320], Copyright© The Royal Society of Chemistry 2020).

dissociation of N₂ molecule on the phosphorene defects has to overcome kinetic barriers of 0.15–1.92 eV (Fig. 11c). The (5|8|5) double vacancy is most reactive to bind and dissociate N₂ molecule (Fig. 11b), and the following hydrogenation reaction toward NH₃ production is energetically favorable with a limiting potential of only 0.28 V under the distal pathway. Similar to the other non-metal catalysts discussed in the previous sections, the distinct activity of various defects in phosphorene is determined by the frontier orbital level of P atoms at the defective region, which dominates the charge donation and back-donation with N₂ (Fig. 11d). Again, the aforementioned "p band model" in the section "Hybrid catalysts of graphitic carbon and transition metal-based materials" is applicable for defective phosphorene, i.e., the N₂ adsorption energy shows an approximate linear relationship with the p-band center of P atoms (calculated by Eq. (6)). As the π* antibonding orbital of N₂ locates below the Fermi level of defective phosphorene, a deeper p-band center of P atoms leads to stronger interaction with N₂ (Fig. 11e). Meanwhile, the presence of vacancy defects not only retains the semiconducting character of phosphorene, but also widens the band gap by 0.1–0.2 eV, such

that the band edge positions of defective phosphorene straddle the NRR redox potentials to endow the photoexcited carriers with sufficient reduction and oxidation power (Fig. 11f). The light absorption in the visible regime is also notably enhanced by the defects (Fig. 11g). In addition, NAMD simulations revealed that the relaxation of photoexcited electrons to the bottom conduction band at the defective region occurs rapidly in a characteristic time of 491 fs, while the electron-hole recombination is much slower and retarded compared with perfect phosphorene due to the increase of band gap (Fig. 11h). These theoretical results provide essential knowledge for activating the basal plane of phosphorene and optimizing both photocarrier dynamics and catalytic activity for high-efficiency solar energy conversion.

Transition metal phosphides

As an important category of transition metal compounds, transition metal phosphides have been demonstrated to be promising electrocatalysts to replace Pt for hydrogen fuel production via water splitting, owing to their easy synthesis, low
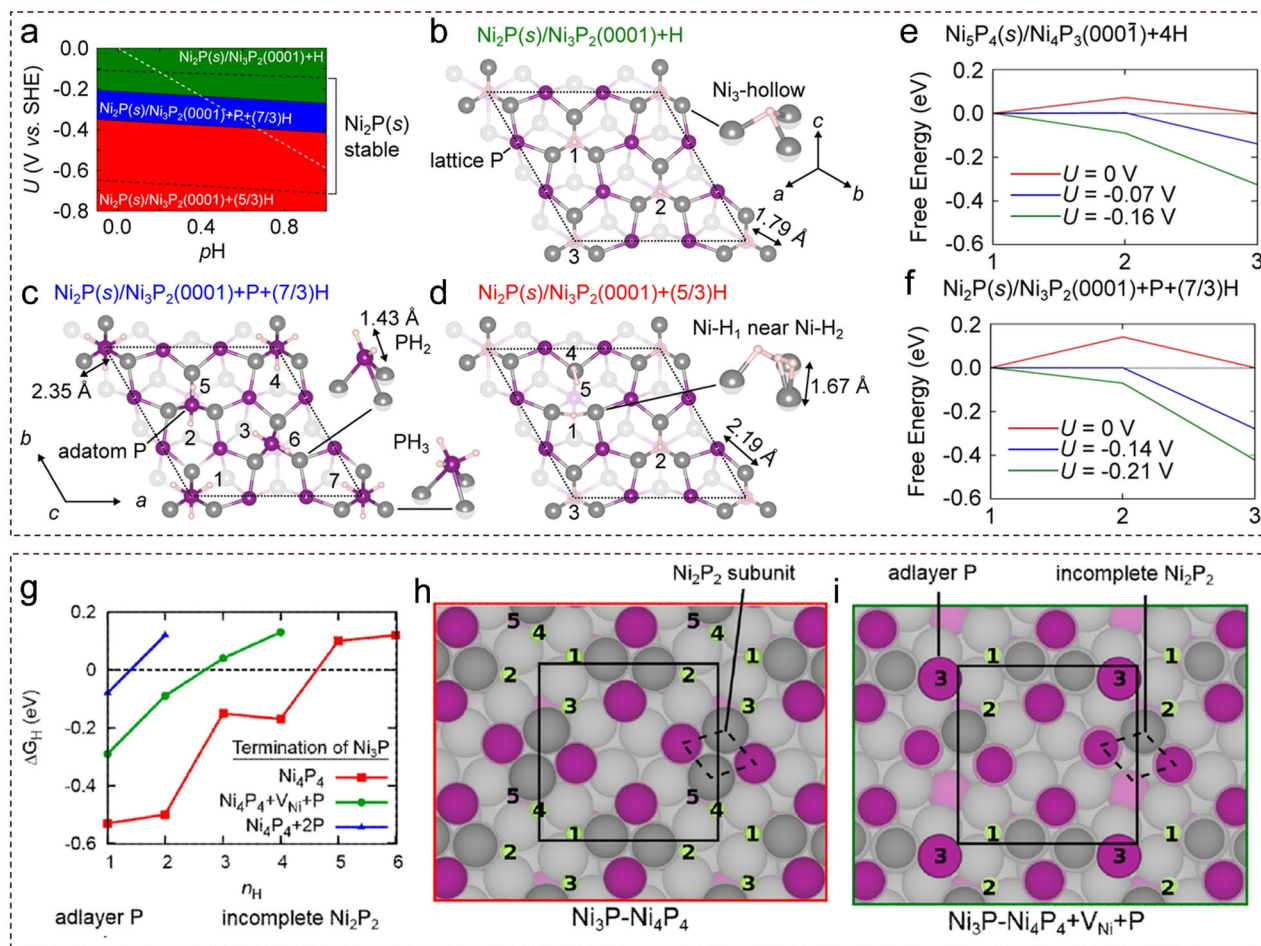
Fig. 12 HER on transition metal phosphides. a Surface phase diagram of $Ni_2P(0001)$. **b–d** The evolution of the surface through adsorption −desorption equilibrium of P. P dissolves off the surface as phosphates. **e, f** Free energy of intermediates in the HER for $Ni_2P(0001)$ and $Ni_5P_4(000\bar{1})$, respectively (**a–f** are reproduced with permission from ref. [342], Copyright© American Chemical Society 2017). **g** The H* adsorption free energy as a function of H* coverage (n_H) for the three stable $Ni_3P(001)$ surfaces on **h** $Ni_3P(s)/Ni_4P_4$ (left) and **i** $Ni_3P(s)/Ni_4P_4+V_{Ni}+P$ (right) (reproduced with permission from ref. [351], Copyright© American Chemical Society 2018).

cost, and excellent activity. Transition metal phosphides exhibit a vast range of chemical compositions[322]. The mostly adopted ones for HER electrocatalysis include molybdenum phosphides (e.g., MoP, Mo_3P, MoP_2)[323–327], nickel phosphides (e.g., NiP_2, Ni_5P_4, Ni_2P, Ni_3P)[328–332], cobalt and iron phosphides (e.g., CoP, FeP, Co_2P, Fe_2P)[333–336], and their alloys[337–340]. In these compounds, the surface exposed metal atoms are typically considered as the reaction centers, while the high stability of P-terminated surface and the role of P atoms on the electrocatalytic process are drawing great attentions.

Kibsgaard et al. combined DFT calculations and experimental characterization to design transition metal phosphides with optimal H* binding strength for HER electrocatalysis[341]. They examined various phosphides with different exposed surfaces, and considered possible binding sites for H* species such as the metal site, P site, and the bridge site between metal and P atoms. Several phosphide surfaces with high HER activity were computationally screened, including MoP(001), FeP(011), Fe_2P(100), CoP (101), Co_2P(101), and Ni_2P(001). Different reaction sites of these systems all occupy a narrow range at the top of the volcano plot, signifying their excellent intrinsic activity, although there is no clear trend of activity with respect to the material constituents. Based on the volcano plot, in which CoP and FeP lie almost equally far apart on the opposite legs of the volcano, iron cobalt alloy phosphide was predicted to have optimal HER performance.

By calculating ΔG_{H^*} for the alloyed phosphides with different Fe: Co ratios, the $Fe_{0.5}Co_{0.5}P$(101) surface was identified to have the highest activity with $\Delta G_{H^*} = 0.004$ eV, which was then verified by the experimental measurement.

The surface termination and reconstruction of nickel phosphides as well as the active role of P atoms during the electrochemical processes have been thoroughly investigated using DFT calculations by Wexler et al.[342] They found that the surface P content on Ni_2P(0001) depends on the external electrode potential, i.e., at $-0.21\,V \geq U \geq -0.36\,V$ versus the standard hydrogen electrode and pH = 0, and a PH_x-enriched Ni_3P_2 termination is most stable for Ni_2P(0001), while beyond this potential range, the Ni_3P_2 surface is passivated by H at the Ni_3-hollow sites. In contrast, $Ni_5P_4(000\bar{1})$ does not favor the P adlayer on the surface; instead a Ni_4P_3 bulk termination passivated by H at both Ni_3 and P_3-hollow sites is most stable (Fig. 12a–d). As a result, the $Ni_5P_4(000\bar{1})$ surface with Ni_4P_3 termination has the lowest overpotential of -0.16 V for HER electrocatalysis (Fig. 12e), owing to the abundant P_3-hollow sites that provide optimal H* binding. Ni_2P(0001) with Ni_3P_2 termination and a P adlayer has a higher overpotential of -0.21 V (Fig. 12f), with the P adatoms serving as the reaction centers. These theoretical results explained the trend of activity between Ni_5P_4 and Ni_2P observed in the experiment. The authors emphasized that the structural flexibility of P, i.e., the capability to form either adlayer or in-plane clusters (P_3-hollow

site) on the surface of transition metal phosphides, plays a key role in the outstanding activity of these compound materials for HER electrocatalysis.

Experimental evidence for P atoms as the active sites in the transition metal phosphide electrocatalysts was provided by Laursen et al.[331]. They synthesized single-phase Ni$_3$P crystallites, which exhibit high HER activity (only slightly lower than that of Ni$_5$P$_4$ and Pt) and high corrosion tolerance in both acid and alkali despite its low P content. Electrochemical studies revealed that poisoning of surface Ni sites does not block HER catalysis in the Ni$_3$P crystallites, indicating that the surface P atoms are the active sites (Fig. 12g, h). Their DFT calculations suggested that the Ni$_3$P (001) surface, which is the dominantly exposed surface observed in the experiment, undergoes reconstruction that strongly favors P enrichment to form the Ni$_4$P$_4$ termination. Such P-enriched (001) surface of Ni$_3$P is highly active for HER electrocatalysis, providing nearly thermoneutral H* binding ($\Delta G_{H*} = 0.04$ eV). The P adatoms on such reconstructed surface are the active sites, and they show lower overpotentials than any of the possible sites on other terminations of the Ni$_3$P(001) surface.

As chemical doping of nickel phosphides has been widely demonstrated in the experiment to improve their activity for HER electrocatalysis[343–346], the underlying mechanism of doping effect has been explored by Partanen et al. from the theoretical point of view[347]. By examining Ni$_2$P doped by Mg, Mo, Fe, Co, V, and Cu, their DFT calculations showed that for Ni$_2$P(0001) with Ni$_3$P$_2$ termination, heteroatom doping would weaken the H* binding at the Ni$_3$-hollow sites and improve the HER activity. The Co and Fe doping may be more readily than the other transition metal elements, while Cu doping is rather unlikely according to their formation energies. The P-rich surface of Ni$_2$P(0001) with Ni$_3$P$_2$ termination and P adlayer has inherently high activity for HER, irrespective of the type of doping or the absence of doping. Each surface P adatom can adsorb several H atoms, which can then evolve into H$_2$ spontaneously during structural optimization, suggesting the high activity of the surface P atoms.

The P-rich surface and the associated high activity have also been observed in the Rh$_2$P electrocatalyst by Duan et al.[348]. They fabricated Rh$_2$P nanocubes dispersed on the carbon material with high surface area, and obtained remarkable performance for both HER and OER comparable to Pt/C and Rh/C electrocatalysts, respectively. The annular dark-field scanning transmission electron microscopy revealed a P-rich outermost atomic layer on the Rh$_2$P nanocubes, consistent with their DFT results on the surface energies of P-terminated and Rh-terminated surfaces. Moreover, their calculations showed that the Rh atoms on the Rh-terminated surface exhibit too strong binding with H* species under all H coverage. On the P-terminated surface, ΔG_{H*} approaches zero as the H coverage increases from 25 to 50%, demonstrating the vital role of P atoms on the HER activity. On the other hand, the OER activity is attributed to the instability of P-terminated surface in the OER potential range in the acidic electrolyte, such that dissolution of P atoms may promote the formation of oxidized surface suitable for OER.

The HER activities of other transition metal phosphides have also been examined in theory. Wang et al. investigated a series of transition metal phosphides (MP) (M = Cr, Mn, Fe, Co, and Ni) with the orthorhombic MnP-type structure (space group *Pnma*), having the low surface-energy (101) facet exposed for electrocatalysis[349]. The top sites of P atoms and the bridge sites between metal and P atoms exhibit high activity, particularly for FeP, CoP, and NiP, having |ΔG_{H*}| below 0.2 eV and fast reaction kinetics with small Tafel barriers. The magnetic properties can actually affect the chemical activities, as spin polarization results in prominent electronic states from the spin up channel in the vicinity of the Fermi level, which mainly interact with H* species. Moreover, creating metal defects on the MP surface can activate the P sites, and the presence of P defects can also boost the HER activity at the metal involved sites. In particular, M-deficit CrP, MnP, and NiP would be more reactive than their pristine counterparts, while P-deficit FeP, CoP, and NiP were found to have enhanced HER performance due to either better catalytic activities or more active sites.

It is also proposed the high valence transition metals can spread their activity to the non-metal elements in the compound materials. Wang et al. considered binary vanadium phosphorus oxides (VPO) as a model catalyst for activation of *n*-butane[350]. Their DFT calculations suggest that the V^{5+} species serve as electron acceptors, while the V = O and P = O species can act as proton acceptors to oxidize *n*-butane. The activity of P = O is favored over V = O and depends on the separation of −OP− chains from the V^{5+} species. Interestingly, the activities of different P = O sites can be quantitatively related to the centers of P = O lone-pair bands (ε_{lp}), which directly interact with H proton. The non-metal oxides, even far away from the reducible transition metal center, can have the ability to activate the C−H bond in *n*-butane, suggesting the long-range interaction between metal and non-metal sites.

In short, the above experimental and theoretical explorations demonstrate the unique activity of P atoms in the transition metal phosphides, and reveal their highly tunable electrocatalytic properties by controlling the chemical compositions, exposed facet, surface termination, doping, and defect engineering. Future studies are necessary not only to unveil the explicit electronic structure-activity relationships for various transition metal phosphides, but also to explore the interaction mechanism between P and transition metal atoms to synergize different kinds of active sites to meet the requirements of complex energy conversion processes.

FUTURE AND OUTLOOK

The ever-growing demands in energy and alerts for global warming have impelled the exploration of advanced strategies to invent a green energy economy. This relies indispensably on the development of high-performance and cost-effective catalysts to replace the rare and precious metals for energy conversion. During the past decade, numerous kinds of non-metal nanostructures have been designed and synthesized in laboratory, in which the *p*-block elements exhibit the transition-metal-like reactivity. Remarkable performance has been widely achieved in the graphitic carbon-based materials for electrocatalysis of ORR, OER, and HER, silicon-based nanostructures for CO$_2$ photoreduction, boron nanosheets, and dispersed atoms as well as black phosphorus nanosheets and heterostructures for water splitting and NRR, and so on. Transition metal oxides, borides, and phosphides have also been demonstrated as promising substitutes for noble metal catalysts, with the surface O, B, and P atoms playing an important role in the catalysis. First-principles calculations help disclose the mechanisms for activating the *p* orbitals of non-metal materials and illuminate the structure-activity relationships. Remarkably, the occupancy and energy level of the *p* orbitals have been found to govern the binding properties of many non-metal systems. Analogous to the *d* band theory for transition metals, a "*p* band model" has been proposed to successfully explain the reactivity of C, Si, O, B, and P elements in various low-dimensional forms. Nowadays, commercial utilization of these new catalysts is still facing many challenges, and requires future efforts from both theoretical and experimental aspects, which should focus on the following directions:

(1) Stability is the most important quality to be considered for catalysts design. Especially for the unprecedented non-metal nanomaterials, their stability under the realistic reaction conditions has to be comprehensively assessed

before exploration for chemical reactions. Exposure of catalysts in the air, humidity, solvent solution, illumination, and reaction adsorbates may induce surface oxidation, reconstruction, irreversible structural deformation, and activity degradation, which should not be overlooked during the computational design. Meanwhile, advanced techniques and strategies are required to fabricate the predicted non-metal catalysts in laboratory and stabilize them for practical uses.

(2) The temperature and pressure for thermal-driven reactions, as well as the solvent effect and pH values for electro-chemical processes greatly impact the catalysts' performance and have to be properly simulated in the computational studies. Cooperation of in situ and/or operando experimental techniques and theoretical modeling at relevant reaction conditions is necessary to understand the nature of active sites and catalytic mechanisms for non-metal elements, as well as to determine the optimal reaction conditions to achieve the best catalytic performance.

(3) Non-metal materials constitute a vast space for designing photocatalysts for solar energy conversion. It is imperative to elucidate the exact influence of different factors (such as chemical reactivity and photo-electronic properties) on the photocatalytic efficiency from both experimental and theoretical aspects. Encouragingly, time-dependent ab initio non-adiabatic molecular dynamics simulation offers a powerful tool for modeling the dynamic properties of excited carriers on a time scale up to nanoseconds. Multiscale simulation of the photocarriers transport in microseconds is necessary to access the photocatalytic process occurring in the experimental characteristic time.

(4) Due to the different natures of p and d orbitals, the p-block-based catalysis encounters unprecedented challenges, requiring abundant research efforts to rise to. In contrast to transition metals with incompletely filled d orbitals, the catalytic activity of p-block elements usually arises from the partial occupancy of p orbitals, which may not be described by a definite oxidation state and hence is difficult to control in the experiment. Moreover, the p band often extends to a wide energy range compared to the localized d band. The energy and profile of p bands may exhibit large discrepancies among different p-block materials, such that they can hardly obey a simple and universal model like the d band theory for transition metals. It would be necessary to exploit machine learning techniques to decode the recessive structure-activity relationships for different kinds of p-block materials.

(5) In many transition metal compounds and hybrid materials, both transition metal atoms and p-block elements play important roles in the catalysis. They either act together as the reaction centers whose activity are governed by the p-d orbital hybridization, or provide individual active sites to cooperatively realize a bifunctional or multifunctional catalytic process. Future work is desired to explore the interaction between d-block and p-block elements during energy conversion, and synergize them to design new catalysts with more efficient reaction pathways and breakthrough performance.

To conclude, non-metal materials for energy conversion still present their own challenges. Nevertheless, the press need of inexpensive and eco-friendly catalysts will motivate perpetual exploration of p-block-element-mediated reactions, toward the goal of using renewable energy to produce clean fuels and chemicals, and ultimately to build a sustainable future.

REFERENCES
1. Seh, Z. W. et al. Combining theory and experiment in electrocatalysis: insights into materials design. *Science* **355**, eaad4998 (2017).
2. Hammer, B. & Nørskov, J. K. Why gold is the noblest of all the metals. *Nature* **376**, 238–240 (1995).
3. Legare, M. A., Pranckevicius, C. & Braunschweig, H. Metallomimetic chemistry of boron. *Chem. Rev.* **119**, 8231–8261 (2019).
4. List, B., Lerner, R. A. & Barbas, C. F. Proline-catalyzed direct asymmetric aldol reactions. *J. Am. Chem. Soc.* **122**, 2395–2396 (2000).
5. Ahrendt, K. A., Borths, C. J. & MacMillan, D. W. C. New strategies for organic catalysis: the first highly enantioselective organocatalytic Diels–Alder reaction. *J. Am. Chem. Soc.* **122**, 4243–4244 (2000).
6. Leitao, E. M., Jurca, T. & Manners, I. Catalysis in service of main group chemistry offers a versatile approach to p-block molecules and materials. *Nat. Chem.* **5**, 817–829 (2013).
7. Luo, F. et al. P-block single-metal-site tin/nitrogen-doped carbon fuel cell cathode catalyst for oxygen reduction reaction. *Nat. Mater.* **19**, 1215–1223 (2020).
8. Liu, X. & Dai, L. M. Carbon-based metal-free catalysts. *Nat. Rev. Mater.* **1**, 16064 (2016).
9. Molle, A. et al. Buckled two-dimensional Xene sheets. *Nat. Mater.* **16**, 163–169 (2017).
10. Mannix, A. J., Kiraly, B., Hersam, M. C. & Guisinger, N. P. Synthesis and chemistry of elemental 2D materials. *Nat. Rev. Chem.* **1**, 0014 (2017).
11. Zhao, J. J., Du, Q. Y., Zhou, S. & Kumar, V. Endohedrally doped cage clusters. *Chem. Rev.* **120**, 9021–9163 (2020).
12. Han, W. Q., Mickelson, W., Cumings, J. & Zettl, A. Transformation of $B_xC_yN_z$ nanotubes to pure BN nanotubes. *Appl. Phys. Lett.* **81**, 1110–1112 (2002).
13. Wen, J. Q., Xie, J., Chen, X. B. & Li, X. A review on g-C_3N_4-based photocatalysts. *Appl. Surf. Sci.* **391**, 72–123 (2017).
14. Tian, J. et al. Synergistic modulation of metal-free photocatalysts by the composition ratio change and heteroatom doping for overall water splitting. *J. Mater. Chem. A* **9**, 11753–11761 (2021).
15. Niu, X., Bai, X., Zhou, Z. & Wang, J. Rational design and characterization of direct Z-scheme photocatalyst for overall water splitting from excited state dynamics simulations. *ACS Catal.* **10**, 1976–1983 (2020).
16. Yu, X. M. et al. Boron-doped graphene for electrocatalytic N_2 reduction. *Joule* **2**, 1610–1622 (2018).
17. Wang, M., Zhang, L., He, Y. & Zhu, H. Recent advances in transition-metal-sulfide-based bifunctional electrocatalysts for overall water splitting. *J. Mater. Chem. A* **9**, 5320–5363 (2021).
18. Ouyang, Y. et al. Activating inert basal planes of MoS_2 for hydrogen evolution reaction through the formation of different intrinsic defects. *Chem. Mater.* **28**, 4390–4396 (2016).
19. Ling, C. et al. Template-grown MoS_2 nanowires catalyze the hydrogen evolution reaction: ultralow kinetic barriers with high active site density. *ACS Catal.* **7**, 5097–5102 (2017).
20. Luo, F. et al. P-block single-metal-site tin/nitrogen-doped carbon fuel cell cathode catalyst for oxygen reduction reaction. *Nat. Mater.* **19**, 1215–1223 (2020).
21. Yang, Z., Oropeza, F. E. & Zhang, K. H. L. P-block metal-based (Sn, In, Bi, Pb) electrocatalysts for selective reduction of CO_2 to formate. *APL Mater.* **8**, 060901 (2020).
22. Nørskov, J. K., Bligaard, T., Rossmeisl, J. & Christensen, C. H. Towards the computational design of solid catalysts. *Nat. Chem.* **1**, 37–46 (2009).
23. Nørskov, J. K., Abild-Pedersen, F., Studt, F. & Bligaard, T. Density functional theory in surface chemistry and catalysis. *Proc. Natl Acad. Sci. USA* **108**, 937–943 (2011).
24. Hammer, B. & Nørskov, J. K. Theoretical surface science and catalysis-calculations and concepts. *Adv. Catal.* **45**, 71–129 (2000).
25. Xu, Y., Kraft, M. & Xu, R. Metal-free carbonaceous electrocatalysts and photocatalysts for water splitting. *Chem. Soc. Rev.* **45**, 3039–3052 (2016).
26. Nie, Y., Li, L. & Wei, Z. D. Recent advancements in Pt and Pt-free catalysts for oxygen reduction reaction. *Chem. Soc. Rev.* **44**, 2168–2201 (2015).

27. Peterson, A. A., Abild-Pedersen, F., Studt, F., Rossmeisl, J. & Nørskov, J. K. How copper catalyzes the electroreduction of carbon dioxide into hydrocarbon fuels. *Energy Environ. Sci.* **3**, 1311–1315 (2010).

28. Nørskov, J. K. et al. Origin of the overpotential for oxygen reduction at a fuel-cell cathode. *J. Phys. Chem. B* **108**, 17886–17892 (2004).

29. Viswanathan, V., Hansen, H. A., Rossmeisl, J. & Nørskov, J. K. Universality in oxygen reduction electrocatalysis on metal surfaces. *ACS Catal.* **2**, 1654–1660 (2012).

30. Skulason, E. et al. A theoretical evaluation of possible transition metal electro-catalysts for N_2 reduction. *Phys. Chem. Chem. Phys.* **14**, 1235–1245 (2012).

31. Ye, R.-P. et al. CO_2 hydrogenation to high-value products via heterogeneous catalysis. *Nat. Commun.* **10**, 5698 (2019).

32. Humphreys, J., Lan, R. & Tao, S. Development and recent progress on ammonia synthesis catalysts for Haber–Bosch process. *Adv. Energy Sustain. Res.* **2**, 2000043 (2021).

33. Zhang, J. T., Xia, Z. H. & Dai, L. M. Carbon-based electrocatalysts for advanced energy conversion and storage. *Sci. Adv.* **1**, e1500564 (2015).

34. Nitopi, S. et al. Progress and perspectives of electrochemical CO_2 reduction on copper in aqueous electrolyte. *Chem. Rev.* **119**, 7610–7672 (2019).

35. Kattel, S., Ramírez, P. J., Chen, J. G., Rodriguez, J. A. & Liu, P. Active sites for CO_2 hydrogenation to methanol on Cu/ZnO catalysts. *Science* **355**, 1296–1299 (2017).

36. Hu, C., Dai, Q. & Dai, L. Multifunctional carbon-based metal-free catalysts for advanced energy conversion and storage. *Cell Rep. Phys. Sci.* **2**, 100328 (2021).

37. Pang, J. et al. Applications of phosphorene and black phosphorus in energy conversion and storage devices. *Adv. Energy Mater.* **8**, 1702093 (2018).

38. Han, R. et al. Functionalised hexagonal boron nitride for energy conversion and storage. *J. Mater. Chem. A* **8**, 14384–14399 (2020).

39. Zhu, C. R., Gao, D., Ding, J., Chao, D. & Wang, J. TMD-based highly efficient electrocatalysts developed by combined computational and experimental approaches. *Chem. Soc. Rev.* **47**, 4332–4356 (2018).

40. Guo, Y. et al. Nanoarchitectonics for transition-metal-sulfide-based electro-catalysts for water splitting. *Adv. Mater.* **31**, 1807134 (2019).

41. Pang, J. et al. Applications of 2D MXenes in energy conversion and storage systems. *Chem. Soc. Rev.* **48**, 72–133 (2019).

42. Ling, C., Shi, L., Ouyang, Y. & Wang, J. Searching for highly active catalysts for hydrogen evolution reaction based on O-terminated MXenes through a simple descriptor. *Chem. Mater.* **28**, 9026–9032 (2016).

43. Ling, C., Shi, L., Ouyang, Y., Chen, Q. & Wang, J. Transition metal-promoted V_2CO_2 (MXenes): a new and highly active catalyst for hydrogen evolution reaction. *Adv. Sci.* **3**, 1600180 (2016).

44. Liu, X. & Dai, L. Carbon-based metal-free catalysts. *Nat. Rev. Mater.* **1**, 16064 (2016).

45. Yang, L. et al. Carbon-based metal-free ORR electrocatalysts for fuel cells: past, present, and future. *Adv. Mater.* **31**, 1804799 (2019).

46. Paul, S. et al. Influence of the metal center in M-N-C catalysts on the CO_2 reduction reaction on gas diffusion electrodes. *ACS Catal.* **11**, 5850–5864 (2021).

47. Trickett, C. A. et al. The chemistry of metal-organic frameworks for CO_2 capture, regeneration and conversion. *Nat. Rev. Mater.* **2**, 17045 (2017).

48. Wang, J. et al. Photo-assisted high performance single atom electrocatalysis of N_2 reduction reaction by Mo-embedded covalent organic framework. *J. Mater. Chem. A* **9**, 19949–19957 (2021).

49. Delafontaine, L., Asset, T. & Atanassov, P. Metal-nitrogen-carbon electrocatalysts for CO_2 reduction towards syngas generation. *ChemSusChem* **13**, 1688–1698 (2020).

50. Melen, R. L. Frontiers in molecular p-block chemistry: from structure to reactivity. *Science* **363**, 479–484 (2019).

51. Gong, K., Du, F., Xia, Z., Durstock, M. & Dai, L. Nitrogen-doped carbon nanotube arrays with high electrocatalytic activity for oxygen reduction. *Science* **323**, 760–764 (2009).

52. Shui, J., Wang, M., Du, F. & Dai, L. N-doped carbon nanomaterials are durable catalysts for oxygen reduction reaction in acidic fuel cells. *Sci. Adv.* **1**, e1400129 (2015).

53. Qu, L., Liu, Y., Baek, J.-B. & Dai, L. Nitrogen-doped graphene as efficient metal-free electrocatalyst for oxygen reduction in fuel cells. *ACS Nano* **4**, 1321–1326 (2010).

54. Zhang, L. & Xia, Z. Mechanisms of oxygen reduction reaction on nitrogen-doped graphene for fuel cells. *J. Phys. Chem. C.* **115**, 11170–11176 (2011).

55. Yu, L., Pan, X., Cao, X., Hu, P. & Bao, X. Oxygen reduction reaction mechanism on nitrogen-doped graphene: a density functional theory study. *J. Catal.* **282**, 183–190 (2011).

56. Del Cueto, M., Ocón, P. & Poyato, J. M. L. Comparative study of oxygen reduction reaction mechanism on nitrogen-, phosphorus-, and boron-doped graphene surfaces for fuel cell applications. *J. Phys. Chem. C.* **119**, 2004–2009 (2015).

57. Zhang, J., Zhao, Z., Xia, Z. & Dai, L. A metal-free bifunctional electrocatalyst for oxygen reduction and oxygen evolution reactions. *Nat. Nanotechnol.* **10**, 444–452 (2015).

58. Li, M., Zhang, L., Xu, Q., Niu, J. & Xia, Z. N-doped graphene as catalysts for oxygen reduction and oxygen evolution reactions: Theoretical considerations. *J. Catal.* **314**, 66–72 (2014).

59. Zheng, Y., Jiao, Y., Ge, L., Jaroniec, M. & Qiao, S. Z. Two-step boron and nitrogen doping in graphene for enhanced synergistic catalysis. *Angew. Chem. Int. Ed.* **125**, 3192–3198 (2013).

60. Guo, D. et al. Active sites of nitrogen-doped carbon materials for oxygen reduction reaction clarified using model catalysts. *Science* **351**, 361–365 (2016).

61. Jiao, Y., Zheng, Y., Jaroniec, M. & Qiao, S. Z. Origin of the electrocatalytic oxygen reduction activity of graphene-based catalysts: a roadmap to achieve the best performance. *J. Am. Chem. Soc.* **136**, 4394–4403 (2014).

62. Zheng, Y. et al. Toward design of synergistically active carbon-based catalysts for electrocatalytic hydrogen evolution. *ACS Nano* **8**, 5290–5296 (2014).

63. Jiao, Y., Zheng, Y., Davey, K. & Qiao, S.-Z. Activity origin and catalyst design principles for electrocatalytic hydrogen evolution on heteroatom-doped graphene. *Nat. Energy* **1**, 577 (2016).

64. Zhao, H. et al. Carbon for the oxygen reduction reaction: a defect mechanism. *J. Mater. Chem. A* **3**, 11736–11739 (2015).

65. Zhang, L., Xu, Q., Niu, J. & Xia, Z. Role of lattice defects in catalytic activities of graphene clusters for fuel cells. *Phys. Chem. Chem. Phys.* **17**, 16733–16743 (2015).

66. Jiang, Y. et al. Significant contribution of intrinsic carbon defects to oxygen reduction activity. *ACS Catal.* **5**, 6707–6712 (2015).

67. Tang, C. et al. Topological defects in metal-free nanocarbon for oxygen electrocatalysis. *Adv. Mater.* **28**, 6845–6851 (2016).

68. Jia, Y. et al. Defect graphene as a trifunctional catalyst for electrochemical reactions. *Adv. Mater.* **28**, 9532–9538 (2016).

69. Jia, Y. et al. Identification of active sites for acidic oxygen reduction on carbon catalysts with and without nitrogen doping. *Nat. Catal.* **2**, 688–695 (2019).

70. Zhu, J. et al. Effects of intrinsic pentagon defects on electrochemical reactivity of carbon nanomaterials. *Angew. Chem. Int. Ed.* **58**, 3859–3864 (2019).

71. Tao, L. et al. Bridging the surface charge and catalytic activity of a defective carbon electrocatalyst. *Angew. Chem. Int. Ed.* **58**, 1019–1024 (2019).

72. Lin, Y. et al. Chromium-ruthenium oxide solid solution electrocatalyst for highly efficient oxygen evolution reaction in acidic media. *Nat. Commun.* **10**, 162 (2019).

73. Huang, J. et al. Modifying redox properties and local bonding of Co_3O_4 by CeO_2 enhances oxygen evolution catalysis in acid. *Nat. Commun.* **12**, 3036 (2021).

74. Deng, D. et al. Iron encapsulated within pod-like carbon nanotubes for oxygen reduction reaction. *Angew. Chem. Int. Ed.* **125**, 389–393 (2013).

75. Deng, J., Deng, D. & Bao, X. Robust catalysis on 2D materials encapsulating metals: concept, application, and perspective. *Adv. Mater.* **29**, 1606967 (2017).

76. Deng, D. et al. Catalysis with two-dimensional materials and their hetero-structures. *Nat. Nanotechnol.* **11**, 218–230 (2016).

77. Deng, J. et al. Highly active and durable non-precious-metal catalysts encap-sulated in carbon nanotubes for hydrogen evolution reaction. *Energy Environ. Sci.* **7**, 1919–1923 (2014).

78. Deng, J., Ren, P., Deng, D. & Bao, X. Enhanced electron penetration through an ultrathin graphene layer for highly efficient catalysis of the hydrogen evolution reaction. *Angew. Chem. Int. Ed.* **54**, 2100–2104 (2015).

79. Cui, X., Ren, P., Deng, D., Deng, J. & Bao, X. Single layer graphene encapsulating non-precious metals as high-performance electrocatalysts for water oxidation. *Energy Environ. Sci.* **9**, 123–129 (2016).

80. Zhou, W. et al. N-doped carbon-wrapped cobalt nanoparticles on N-doped graphene nanosheets for high-efficiency hydrogen production. *Chem. Mater.* **27**, 2026–2032 (2015).

81. Chen, Z. et al. Ultrafine Co nanoparticles encapsulated in carbon-nanotubes-grafted graphene sheets as advanced electrocatalysts for the hydrogen evolution reaction. *Adv. Mater.* **30**, 1802011 (2018).

82. Shen, Y. et al. Nickel–copper alloy encapsulated in graphitic carbon shells as electrocatalysts for hydrogen evolution reaction. *Adv. Energy Mater.* **8**, 1701759 (2018).

83. Yang, F., Chen, Y., Cheng, G., Chen, S. & Luo, W. Ultrathin nitrogen-doped carbon coated with CoP for efficient hydrogen evolution. *ACS Catal.* **7**, 3824–3831 (2017).

84. Wang, M.-Q. et al. Engineering the nanostructure of molybdenum nitride nanodot embedded N-doped porous hollow carbon nanochains for rapid all pH hydrogen evolution. *J. Mater. Chem. A* **6**, 14734–14741 (2018).

85. Miao, M. et al. Chainmail catalyst of ultrathin P-doped carbon shell-encapsulated nickel phosphides on graphene towards robust and efficient hydrogen generation. *J. Mater. Chem. A* **6**, 24107–24113 (2018).

86. Huang, X. et al. Carbon nanotube-encapsulated noble metal nanoparticle hybrid as a cathode material for Li-oxygen batteries. *Adv. Funct. Mater.* **24**, 6516–6523 (2014).

87. Hou, Y. et al. Metal–organic framework-derived nitrogen-doped core-shell-structured porous Fe/Fe$_3$C@C nanoboxes supported on graphene sheets for efficient oxygen reduction reactions. *Adv. Energy Mater.* **4**, 1400337 (2014).

88. Yang, C. C., Zai, S. F., Zhou, Y. T., Du, L. & Jiang, Q. Fe$_3$C-Co nanoparticles encapsulated in a hierarchical structure of N-doped carbon as a multifunctional electrocatalyst for ORR, OER, and HER. *Adv. Funct. Mater.* **29**, 1901949 (2019).

89. Yang, Y. et al. Tuning electronic structures of nonprecious ternary alloys encapsulated in graphene layers for optimizing overall water splitting activity. *ACS Catal.* **7**, 469–479 (2017).

90. Zhou, S., Liu, N., Wang, Z. & Zhao, J. Nitrogen-doped graphene on transition metal substrates as efficient bifunctional catalysts for oxygen reduction and oxygen evolution reactions. *ACS Appl. Mater. Inter.* **9**, 22578–22587 (2017).

91. Liu, S. et al. Metal-organic-framework-derived hybrid carbon nanocages as a bifunctional electrocatalyst for oxygen reduction and evolution. *Adv. Mater.* **29**, 1700874 (2017).

92. Yu, M. et al. Long life rechargeable Li-O$_2$ batteries enabled by enhanced charge transfer in nanocable-like Fe@N-doped carbon nanotube catalyst. *Sci. China Mater.* **60**, 415–426 (2017).

93. Pei, W., Zhou, S., Bai, Y. & Zhao, J. N-doped graphitic carbon materials hybridized with transition metals (compounds) for hydrogen evolution reaction: understanding the synergistic effect from atomistic level. *Carbon* **133**, 260–266 (2018).

94. Hoffmann, R. An extended Hückel theory. I. Hydrocarbons. *J. Chem. Phys.* **39**, 1397–1412 (1963).

95. Zhou, S., Yang, X., Pei, W., Liu, N. & Zhao, J. Heterostructures of MXenes and N-doped graphene as highly active bifunctional electrocatalysts. *Nanoscale* **10**, 10876–10883 (2018).

96. Wu, X. et al. Engineering multifunctional collaborative catalytic interface enabling efficient hydrogen evolution in all pH range and seawater. *Adv. Energy Mater.* **9**, 1901333 (2019).

97. Luo, Z., Wang, T. & Gong, J. Single-crystal silicon-based electrodes for unbiased solar water splitting: current status and prospects. *Chem. Soc. Rev.* **48**, 2158–2181 (2019).

98. Steven, Y. Reece et al. Wireless solar water splitting using silicon-based semiconductors and earth-abundant catalysts. *Science* **334**, 645–648 (2011).

99. Qu, Y., Zhou, H. & Duan, X. Porous silicon nanowires. *Nanoscale* **3**, 4060–4068 (2011).

100. Chen, Y. W. et al. Atomic layer-deposited tunnel oxide stabilizes silicon photoanodes for water oxidation. *Nat. Mater.* **10**, 539–544 (2011).

101. Oh, I., Kye, J. & Hwang, S. Enhanced photoelectrochemical hydrogen production from silicon nanowire array photocathode. *Nano Lett.* **12**, 298–302 (2012).

102. Liu, R. et al. Silicon nanowires as photoelectrodes for carbon dioxide fixation. *Angew. Chem. Int. Ed.* **51**, 6709–6712 (2012).

103. Yuan, G. et al. Understanding the origin of the low performance of chemically grown silicon nanowires for solar energy conversion. *Angew. Chem. Int. Ed.* **50**, 2334–2338 (2011).

104. Li, X. et al. Photoelectrochemical hydrogen evolution of tapered silicon nanowires. *Phys. Chem. Chem. Phys.* **17**, 800–804 (2015).

105. Boettcher, S. W. et al. Photoelectrochemical hydrogen evolution using Si microwire arrays. *J. Am. Chem. Soc.* **133**, 1216–1219 (2011).

106. Hou, Y. et al. Bioinspired molecular co-catalysts bonded to a silicon photocathode for solar hydrogen evolution. *Nat. Mater.* **10**, 434–438 (2011).

107. Jang, J. W. et al. Enabling unassisted solar water splitting by iron oxide and silicon. *Nat. Commun.* **6**, 7447 (2015).

108. Jin, T. et al. CO$_2$ reduction with Re(i)-NHC compounds: driving selective catalysis with a silicon nanowire photoelectrode. *Chem. Commun.* **52**, 14258–14261 (2016).

109. Shan, B. et al. A silicon-based heterojunction integrated with a molecular excited state in a water-splitting tandem cell. *J. Am. Chem. Soc.* **141**, 10390–10398 (2019).

110. Zhang, R. Q., Liu, X. M., Wen, Z. & Jiang, Q. Prediction of silicon nanowires as photocatalysts for water splitting: band structures calculated using density functional theory. *J. Phys. Chem. C* **115**, 3425–3428 (2011).

111. Liu, D. et al. The nature of photocatalytic "water splitting" on silicon nanowires. *Angew. Chem. Int. Ed.* **54**, 2980–2985 (2015).

112. Oh, J., Deutsch, T. G., Yuan, H.-C. & Branz, H. M. Nanoporous black silicon photocathode for H$_2$ production by photoelectrochemical water splitting. *Energy Environ. Sci.* **4**, 1690–1694 (2011).

113. Dai, F. et al. Bottom-up synthesis of high surface area mesoporous crystalline silicon and evaluation of its hydrogen evolution performance. *Nat. Commun.* **5**, 3605 (2014).

114. Ryu, J. et al. All-in-one synthesis of mesoporous silicon nanosheets from natural clay and their applicability to hydrogen evolution. *NPG Asia Mater.* **8**, e248 (2016).

115. Jang, Y. J., Ryu, J., Hong, D., Park, S. & Lee, J. S. A multi-stacked hyperporous silicon flake for highly active solar hydrogen production. *Chem. Commun.* **52**, 10221–10224 (2016).

116. Song, H. et al. Highly crystalline mesoporous silicon spheres for efficient visible photocatalytic hydrogen evolution. *ChemNanoMat* **3**, 22–26 (2017).

117. Martell, S. A., Werner-Zwanziger, U. & Dasog, M. The influence of hydrofluoric acid etching processes on the photocatalytic hydrogen evolution reaction using mesoporous silicon nanoparticles. *Faraday Discuss.* **222**, 176–189 (2020).

118. Sun, W. et al. The next big thing for silicon nanostructures-CO$_2$ photocatalysis. *Faraday Discuss.* **222**, 424–432 (2020).

119. Sun, W. et al. Heterogeneous reduction of carbon dioxide by hydride-terminated silicon nanocrystals. *Nat. Commun.* **7**, 12553 (2016).

120. Dasog, M., Kraus, S., Sinelnikov, R., Veinot, J. G. & Rieger, B. CO$_2$ to methanol conversion using hydride terminated porous silicon nanoparticles. *Chem. Commun.* **53**, 3114–3117 (2017).

121. Wong, A. P. Y. et al. Tailoring CO$_2$ reduction with doped silicon nanocrystals. *Adv. Sustain. Syst.* **1**, 1700118 (2017).

122. Qian, C. et al. Catalytic CO$_2$ reduction by palladium-decorated silicon–hydride nanosheets. *Nat. Catal.* **2**, 46–54 (2019).

123. Ji, Y., Wang, G., Fan, T. & Luo, Y. First-principles study on the molecular mechanism of solar-driven CO$_2$ reduction on H-terminated Si. *ChemSusChem* **13**, 3524–3529 (2020).

124. Peng, Y. et al. Molecular-level insight into how hydroxyl groups boost catalytic activity in CO$_2$ hydrogenation into methanol. *Chem* **4**, 613–625 (2018).

125. Zhao, J. et al. Rise of silicene: a competitive 2D material. *Prog. Mater. Sci.* **83**, 24–151 (2016).

126. Fleurence, A. et al. Experimental evidence for epitaxial silicene on diboride thin films. *Phys. Rev. Lett.* **108**, 245501 (2012).

127. Krishnamoorthy, K., Pazhamalai, P. & Kim, S. J. Two-dimensional siloxene nanosheets: novel high-performance supercapacitor electrode materials. *Energy Environ. Sci.* **11**, 1595–1602 (2018).

128. Lin, S. S. et al. Quasi-two-dimensional SiC and SiC$_2$: interaction of silicon and carbon at atomic thin lattice plane. *J. Phys. Chem. C* **119**, 19772–19779 (2015).

129. Chen, J. W. et al. 2D silicon-based semiconductor Si$_2$Te$_3$ toward broadband photodetection. *Small* **17**, 2006496 (2021).

130. Feng, J.-W. et al. Gas adsorption on silicene: a theoretical study. *Comput. Mater. Sci.* **87**, 218–226 (2014).

131. Xu, X. et al. Removal of NO with silicene: a DFT investigation. *RSC Adv.* **5**, 22135–22147 (2015).

132. Xiao, Y., Lu, X., Ng, S. P. & Wu, C.-M. L. Trivacancy and stone-wales defected silicene for adsorption of small gas molecules. *Comput. Mater. Sci.* **154**, 276–283 (2018).

133. Morrissey, C. & He, H. Silicene catalyzed reduction of nitrobenzene to aniline: a mechanistic study. *Chem. Phys. Lett.* **695**, 228–234 (2018).

134. Jiang, Q., Zhang, J., Huang, H., Wu, Y. & Ao, Z. Strain effect on the dissociation of water molecules on silicene: density functional theory study. *J. Phys. Chem. C* **123**, 11591–11601 (2019).

135. Guerrero-Sánchez, J., Munoz-Pizza, D. M. & Takeuchi, N. Silicene as an efficient way to fully inactivate the SO$_2$ pollutant. *Appl. Surf. Sci.* **479**, 847–851 (2019).

136. Hu, W., Li, Z. & Yang, J. Water on silicene: a hydrogen bond-autocatalyzed physisorption–chemisorption–dissociation transition. *Nano Res.* **10**, 2223–2233 (2017).

137. Zhou, S., Pei, W., Zhao, J. & Du, A. Silicene catalysts for CO$_2$ hydrogenation: the number of layers controls selectivity. *Nanoscale* **11**, 7734–7743 (2019).

138. Mitas, L., Grossman, J. C., Stich, I. & Tobik, J. Silicon clusters of intermediate size: energetics, dynamics, and thermal effects. *Phys. Rev. Lett.* **84**, 1479–1482 (2000).

139. Zhao, J., Du, Q., Zhou, S. & Kumar, V. Endohedrally doped cage clusters. *Chem. Rev.* **120**, 9021–9163 (2020).

140. Zhou, S., Yang, X., Pei, W., Zhao, J. & Du, A. Silicon nanocages for selective carbon dioxide conversion under visible light. *J. Phys. Chem. C* **123**, 9973–9980 (2019).

141. Pei, W., Zhou, S. & Bai, Y. Solar driven CO$_2$ hydrogenation on Ti-doped silicon nanocages. *J. Clust. Sci.* **31**, 627–635 (2019).

142. Wang, S., Wang, C., Pan, W., Sun, W. & Yang, D. Two-dimensional silicon for (photo)catalysis. *Sol. RRL* **5**, 2000392 (2020).

143. Li, S. et al. Siloxene nanosheets: a metal-free semiconductor for water splitting. *J. Mater. Chem. A* **4**, 15841–15844 (2016).

144. Rosli, N. F. et al. Siloxene, germanane, and methylgermanane: functionalized 2D materials of group 14 for electrochemical applications. *Adv. Funct. Mater.* **30**, 1910186 (2020).

145. Imagawa, H. et al. Photocatalytic NO removal over calcium-bridged siloxenes under ultraviolet and visible light irradiation. *Dalton Trans.* **47**, 7070–7076 (2018).

146. Mishra, A. K., Belgamwar, R., Jana, R., Datta, A. & Polshettiwar, V. Defects in nanosilica catalytically convert CO₂ to methane without any metal and ligand. *Proc. Natl Acad. Sci. USA* **117**, 6383–6390 (2020).

147. Zhang, W. X. et al. Tunable electronic and optical properties of a planar hydrogenated AsSi hybrid nanosheet: a potential wide water-splitting photocatalyst. *J. Phys. Chem. C* **123**, 14999–15008 (2019).

148. Ma, Z., Zhuang, J., Zhang, X. & Zhou, Z. SiP monolayers: new 2D structures of group IV–V compounds for visible-light photohydrolytic catalysts. *Front. Phys.* **13**, 138104 (2018).

149. Shojaei, F., Mortazavi, B., Zhuang, X. & Azizi, M. Silicon diphosphide (SiP₂) and silicon diarsenide (SiAs₂): novel stable 2D semiconductors with high carrier mobilities, promising for water splitting photocatalysts. *Mater. Today Energy* **16**, 100377 (2020).

150. Matta, S. K., Zhang, C., Jiao, Y., O'Mullane, A. & Du, A. Versatile two-dimensional silicon diphosphide (SiP₂) for photocatalytic water splitting. *Nanoscale* **10**, 6369–6374 (2018).

151. Kattel, S., Liu, P. & Chen, J. G. G. Tuning selectivity of CO₂ hydrogenation reactions at the metal/oxide interface. *J. Am. Chem. Soc.* **139**, 9739–9754 (2017).

152. Wang, Y., Li, J. & Wei, Z. D. Transition-metal-oxide-based catalysts for the oxygen reduction reaction. *J. Mater. Chem. A* **6**, 8194–8209 (2018).

153. Li, Y. F. & Liu, Z. P. Structure and water oxidation activity of 3D metal oxides. *WIREs Comput. Mol. Sci.* **6**, 47–64 (2016).

154. Wu, J. H., Huang, Y., Ye, W. & Li, Y. G. CO₂ reduction: from the electrochemical to photochemical approach. *Adv. Sci.* **4**, 1700194 (2017).

155. Browne, M. P., Sofer, Z. & Pumera, M. Layered and two dimensional metal oxides for electrochemical energy conversion. *Energy Environ. Sci.* **12**, 41–58 (2019).

156. Jia, J. et al. Heterogeneous catalytic hydrogenation of CO₂ by metal oxides: defect engineering-perfecting imperfection. *Chem. Soc. Rev.* **46**, 4631–4644 (2017).

157. Graciani, J. et al. Highly active copper-ceria and copper-ceria-titania catalysts for methanol synthesis from CO₂. *Science* **345**, 546–550 (2014).

158. Wu, C. et al. Inverse ZrO₂/Cu as a highly efficient methanol synthesis catalyst from CO₂ hydrogenation. *Nat. Commun.* **11**, 5767 (2020).

159. Rodriguez, J. A. et al. Inverse oxide/metal catalysts in fundamental studies and practical applications: a perspective of recent developments. *J. Phys. Chem. Lett.* **7**, 2627–2639 (2016).

160. Kattel, S., Liu, P. & Chen, J. G. Tuning selectivity of CO₂ hydrogenation reactions at the metal/oxide interface. *J. Am. Chem. Soc.* **139**, 9739–9754 (2017).

161. Kattel, S. et al. CO₂ hydrogenation over oxide-supported PtCo catalysts: the role of the oxide support in determining the product selectivity. *Angew. Chem. Int. Ed.* **55**, 7968–7973 (2016).

162. Zhao, Y. X., Wu, X. N., Ma, J. B., He, S. G. & Ding, X. L. Characterization and reactivity of oxygen-centred radicals over transition metal oxide clusters. *Phys. Chem. Chem. Phys.* **13**, 1925–1938 (2011).

163. Ding, X. L., Wu, X. N., Zhao, Y. X. & He, S. G. C-H bond activation by oxygen-centered radicals over atomic clusters. *Acc. Chem. Res.* **45**, 382–390 (2012).

164. Man, I. C. et al. Universality in oxygen evolution electrocatalysis on oxide surfaces. *ChemCatChem* **3**, 1159–1165 (2011).

165. Mueller, D. N., Machala, M. L., Bluhm, H. & Chueh, W. C. Redox activity of surface oxygen anions in oxygen-deficient perovskite oxides during electrochemical reactions. *Nat. Commun.* **6**, 6097 (2015).

166. Rong, X., Parolin, J. & Kolpak, A. M. A fundamental relationship between reaction mechanism and stability in metal oxide catalysts for oxygen evolution. *ACS Catal.* **6**, 1153–1158 (2016).

167. Yoo, J. S., Liu, Y. S., Rong, X. & Kolpak, A. M. Electronic origin and kinetic feasibility of the lattice oxygen participation during the oxygen evolution reaction on perovskites. *J. Phys. Chem. Lett.* **9**, 1473–1479 (2018).

168. Yoo, J. S., Rong, X., Liu, Y. S. & Kolpak, A. M. Role of lattice oxygen participation in understanding trends in the oxygen evolution reaction on perovskites. *ACS Catal.* **8**, 4628–4636 (2018).

169. Agyeman, D. A. et al. Synergistic catalysis of the lattice oxygen and transition Metal facilitating ORR and OER in perovskite catalysts for Li–O₂ batteries. *ACS Catal.* **11**, 424–434 (2020).

170. Pan, Y. L. et al. Direct evidence of boosted oxygen evolution over perovskite by enhanced lattice oxygen participation. *Nat. Commun.* **11**, 2002 (2020).

171. Wang, X. Y. et al. Atomic-scale insights into surface lattice oxygen activation at the spinel/perovskite interface of Co₃O₄/La₀.₃Sr₀.₇CoO₃. *Angew. Chem. Int. Ed.* **58**, 11720–11725 (2019).

172. Grimaud, A. et al. Activating lattice oxygen redox reactions in metal oxides to catalyse oxygen evolution. *Nat. Chem.* **9**, 457–465 (2017).

173. Schweinar, K., Gault, B., Mouton, I. & Kasian, O. Lattice oxygen exchange in rutile IrO₂ during the oxygen evolution reaction. *J. Phys. Chem. Lett.* **11**, 5008–5014 (2020).

174. Zagalskaya, A. & Alexandrov, V. Role of defects in the interplay between adsorbate evolving and lattice oxygen mechanisms of the oxygen evolution reaction in RuO₂ and IrO₂. *ACS Catal.* **10**, 3650–3657 (2020).

175. Zagalskaya, A., Evazzade, I. & Alexandrov, V. Ab Initio thermodynamics and kinetics of the lattice oxygen evolution reaction in iridium oxides. *ACS Energy Lett.* **6**, 1124–1133 (2021).

176. Grimaud, A. et al. Activation of surface oxygen sites on an iridium-based model catalyst for the oxygen evolution reaction. *Nat. Energy* **2**, 16189 (2017).

177. Zhang, L. S. et al. Boosting neutral water oxidation through surface oxygen modulation. *Adv. Mater.* **32**, 2002297 (2020).

178. Huang, Z. F. et al. Chemical and structural origin of lattice oxygen oxidation in Co-Zn oxyhydroxide oxygen evolution electrocatalysts. *Nat. Energy* **4**, 329–338 (2019).

179. Zhang, N. et al. Lattice oxygen activation enabled by high-valence metal sites for enhanced water oxidation. *Nat. Commun.* **11**, 4066 (2020).

180. Zhao, J. W., Li, C. F., Shi, Z. X., Guan, J. L. & Li, G. R. Boosting lattice oxygen oxidation of perovskite to efficiently catalyze oxygen evolution reaction by FEOOH decoration. *Research* **2020**, 6961578 (2020).

181. Dickens, C. F., Montoya, J. H., Kulkarni, A. R., Bajdich, M. & Nørskov, J. K. An electronic structure descriptor for oxygen reactivity at metal and metal-oxide surfaces. *Surf. Sci.* **681**, 122–129 (2019).

182. Kumbhakar, P. et al. Emerging 2D metal oxides and their applications. *Mater. Today* **45**, 142–168 (2021).

183. Kalantar-zadeh, K. et al. Two dimensional and layered transition metal oxides. *Appl. Mater. Today* **5**, 73–89 (2016).

184. Mei, J., Liao, T., Kou, L. Z. & Sun, Z. Q. Two-dimensional metal oxide nanomaterials for next-generation rechargeable batteries. *Adv. Mater.* **29**, 1700176 (2017).

185. Fu, Q. et al. Interface-confined ferrous centers for catalytic oxidation. *Science* **328**, 1141–1144 (2010).

186. Wu, D. X., Lagally, M. G. & Liu, F. Stabilizing graphitic thin films of wurtzite materials by epitaxial strain. *Phys. Rev. Lett.* **107**, 236101 (2011).

187. Song, Y. H. et al. Electronic structure tuning of 2D metal (hydr)oxides nanosheets for electrocatalysis. *Small* **17**, 2002240 (2021).

188. Geng, Z. G. et al. Oxygen vacancies in ZnO nanosheets enhance CO₂ electrochemical reduction to CO. *Angew. Chem. Int. Ed.* **57**, 6054–6059 (2018).

189. Wu, H. et al. Controlled growth of uniform two-dimensional ZnO overlayers on Au(111) and surface hydroxylation. *Nano Res.* **12**, 2348–2354 (2019).

190. Kumbhakar, P. et al. Confinement aided simultaneous water cleaning and energy harvesting using atomically thin wurtzite (wurtzene). *Adv. Sustain. Syst.* **5**, 2000189 (2021).

191. Ma, D. W. et al. CO catalytic oxidation on Al-doped graphene-like ZnO monolayer sheets: a first-principles study. *J. Mater. Chem. C* **3**, 9964–9972 (2015).

192. Zhao, Y. Y., Liu, N. S., Zhou, S. & Zhao, J. J. Two-dimensional ZnO for the selective photoreduction of CO₂. *J. Mater. Chem. A* **7**, 16294–16303 (2019).

193. Liu, N. S., Zhou, S. & Zhao, J. J. Solar driven CO₂ hydrogenation on transition metal doped Zn₁₂O₁₂ cluster. *J. Chem. Phys.* **153**, 164306 (2020).

194. Pal, J. et al. Morphology of monolayer MgO films on Ag(100): switching from corrugated islands to extended flat terraces. *Phys. Rev. Lett.* **112**, 126102 (2014).

195. Benedetti, S. et al. Structure and morphology of thin MgO films on Mo(001). *Phys. Rev. B* **78**, 195411 (2008).

196. Arita, R. et al. Polar surface engineering in ultrathin MgO(111)/Ag(111): possibility of a metal-insulator transition and magnetism. *Phys. Rev. B* **69**, 235423 (2004).

197. Nilius, N. et al. Electronic and electrostatic properties of polar oxide nanostructures: MgO(111) islands on Au(111). *Phys. Rev. B* **86**, 205410 (2012).

198. Sarpi, B., Putero, M., Hemeryck, A. & Vizzini, S. MgO monolayer epitaxy on Ni (100). *Appl. Phys. Lett.* **111**, 211604 (2017).

199. Hellman, A., Klacar, S. & Gronbeck, H. Low temperature CO oxidation over supported ultrathin MgO films. *J. Am. Chem. Soc.* **131**, 16636–16637 (2009).

200. Gonchar, A. et al. Activation of oxygen on MgO: O₂⁻ radical ion formation on thin, metal-supported MgO(001) films. *Angew. Chem. Int. Ed.* **50**, 2635–2638 (2011).

201. Song, Z. J., Fan, J., Shan, Y. Y., Ng, A. M. C. & Xu, H. Generation of highly reactive oxygen species on metal-supported MgO(100) thin films. *Phys. Chem. Chem. Phys.* **18**, 25373–25379 (2016).

202. Savio, L., Celasco, E., Vattuone, L. & Rocca, M. Enhanced reactivity at metal-oxide interface: water interaction with MgO ultrathin films. *J. Phys. Chem. B* **108**, 7771–7778 (2004).

203. Shin, H. J. et al. State-selective dissociation of a single water molecule on an ultrathin MgO film. *Nat. Mater.* **9**, 442–447 (2010).

204. Jung, J., Shin, H. J., Kim, Y. & Kawai, M. Ligand field effect at oxide-metal interface on the chemical reactivity of ultrathin oxide film surface. *J. Am. Chem. Soc.* **134**, 10554–10561 (2012).

205. Song, Z. J., Fan, J. & Xu, H. Strain-induced water dissociation on supported ultrathin oxide films. *Sci. Rep.* **6**, 22853 (2016).

206. Liu, N., Zhou, S. & Zhao, J. Visible-light overall water splitting on g-C₃N₄ decorated by subnanometer oxide clusters. *Mater. Today Phys.* **16**, 100312 (2021).

207. Tosoni, S., Spinnato, D. & Pacchioni, G. DFT study of CO₂ activation on doped and ultrathin MgO films. *J. Phys. Chem. C* **119**, 27594–27602 (2015).

208. Calaza, F. et al. Carbon dioxide activation and reaction induced by electron transfer at an oxide-metal interface. *Angew. Chem. Int. Ed.* **54**, 12484–12487 (2015).

209. Liu, N. S., Zhao, Y. Y., Zhou, S. & Zhao, J. J. CO₂ reduction on p-block metal oxide overlayers on metal substrates-2D MgO as a prototype. *J. Mater. Chem. A* **8**, 5688–5698 (2020).

210. Kwon, S., Liao, P. L., Stair, P. C. & Snurr, R. Q. Alkaline-earth metal-oxide overlayers on TiO₂: application toward CO₂ photoreduction. *Catal. Sci. Technol.* **6**, 7885–7895 (2016).

211. Marc-André, L. égaré et al. Nitrogen fixation and reduction at boron. *Science* **359**, 896–900 (2018).

212. Marc-André, L. égaré et al. The reductive coupling of dinitrogen. *Science* **363**, 1329–1332 (2019).

213. Ling, C., Niu, X., Li, Q., Du, A. & Wang, J. Metal-free single atom catalyst for N₂ fixation driven by visible light. *J. Am. Chem. Soc.* **140**, 14161–14168 (2018).

214. Bhattacharyya, K. & Datta, A. Visible light driven efficient metal free single atom catalyst supported on nanoporous carbon nitride for nitrogen fixation. *Phys. Chem. Chem. Phys.* **21**, 12346–12352 (2019).

215. Ji, S., Wang, Z. & Zhao, J. A boron-interstitial doped C₂N layer as a metal-free electrocatalyst for N₂ fixation: a computational study. *J. Mater. Chem. A* **7**, 2392–2399 (2019).

216. Cao, Y. et al. Single and double boron atoms doped nanoporous C₂N-h2D electrocatalysts for highly efficient N₂ reduction reaction: a density functional theory study. *Nanotechnol* **30**, 335403 (2019).

217. Cao, X., Shen, J., Li, X. F. & Luo, Y. Spin polarization-induced facile dioxygen activation in boron-doped graphitic carbon nitride. *ACS Appl. Mater. Inter.* **12**, 52741–52748 (2020).

218. Zheng, M. et al. A boron-decorated melon-based carbon nitride as a metal-free photocatalyst for N₂ fixation: a DFT study. *Phys. Chem. Chem. Phys.* **22**, 21872–21880 (2020).

219. Nong, W., Liang, H., Qin, S., Li, Y. & Wang, C. Computational design of two-dimensional boron-containing compounds as efficient metal-free electrocatalysts toward nitrogen reduction independent of heteroatom doping. *ACS Appl. Mater. Inter.* **12**, 50505–50515 (2020).

220. Lv, X., Wei, W., Li, F., Huang, B. & Dai, Y. Metal-free B@g-CN: visible/infrared light-driven single atom photocatalyst enables spontaneous dinitrogen reduction to ammonia. *Nano Lett.* **19**, 6391–6399 (2019).

221. Yin, H., Gan, L.-Y. & Wang, P. The identification of optimal active boron sites for N₂ reduction. *J. Mater. Chem. A* **8**, 3910–3917 (2020).

222. Wang, W. et al. Formation of B–N–C coordination to stabilize the exposed active nitrogen atoms in g-C₃N₄ for dramatically enhanced photocatalytic ammonia synthesis performance. *Small* **16**, 1906880 (2020).

223. Li, F. & Tang, Q. A di-boron pair doped MoS₂ (B₂@MoS₂) single-layer shows superior catalytic performance for electrochemical nitrogen activation and reduction. *Nanoscale* **11**, 18769–18778 (2019).

224. Shi, L. et al. Metal-free electrocatalyst for reducing nitrogen to ammonia using a Lewis acid pair. *J. Mater. Chem. A* **7**, 4865–4871 (2019).

225. Ma, B., Peng, Y., Ma, D., Deng, Z. & Lu, Z. Boron-doped InSe monolayer as a promising electrocatalyst for nitrogen reduction into ammonia at ambient conditions. *Appl. Surf. Sci.* **495**, 143463 (2019).

226. Liu, C. et al. Single-boron catalysts for nitrogen reduction reaction. *J. Am. Chem. Soc.* **141**, 2884–2888 (2019).

227. Yu, X. et al. Boron-doped graphene for electrocatalytic N₂ reduction. *Joule* **2**, 1610–1622 (2018).

228. Kong, Y. et al. Boron and nitrogen co-doped porous carbon nanofibers as metal-free electrocatalysts for highly efficient ammonia electrosynthesis. *J. Mater. Chem. A* **7**, 26272–26278 (2019).

229. Qiu, W. B., Luo, Y. X., Liang, R. P., Qiu, J. D. & Xia, X. H. B₄C nanosheets decorated with in situ-derived boron-doped graphene quantum dots for high-efficiency ambient N₂ fixation. *Chem. Commun.* **55**, 7406–7409 (2019).

230. Xiao, S., Luo, F., Hu, H. & Yang, Z. Boron and nitrogen dual-doped carbon nanospheres for efficient electrochemical reduction of N₂ to NH₃. *Chem. Commun.* **56**, 446–449 (2020).

231. Guo, Y. et al. Molybdenum and boron synergistically boosting efficient electrochemical nitrogen fixation. *Nano Energy* **78**, 105391 (2020).

232. Li, Q., Guo, Y., Tian, Y., Liu, W. & Chu, K. Activating VS₂ basal planes for enhanced NRR electrocatalysis: the synergistic role of S-vacancies and B dopants. *J. Mater. Chem. A* **8**, 16195–16202 (2020).

233. Liu, B. et al. Nanostructured and boron-doped diamond as an electrocatalyst for nitrogen fixation. *ACS Energy Lett.* **5**, 2590–2596 (2020).

234. Liu, Y. et al. Selective electrochemical reduction of carbon dioxide to ethanol on a boron- and nitrogen-co-doped nanodiamond. *Angew. Chem. Int. Ed.* **129**, 15813–15817 (2017).

235. Chen, Z., Zhao, J., Zhao, J., Chen, Z. & Yin, L. Frustrated Lewis pairs photocatalyst for visible light-driven reduction of CO to multi-carbon chemicals. *Nanoscale* **11**, 20777–20784 (2019).

236. Chen, Z., Liu, X., Zhao, J., Jiao, Y. & Yin, L. Strain effect on the catalytic activities of B- and B/N-doped black phosphorene for electrochemical conversion of CO to valuable chemicals. *J. Mater. Chem. A* **8**, 11986–11995 (2020).

237. Wan-Lu, L. et al. From planar boron clusters to borophenes and metalloborophenes. *Nat. Rev. Chem.* **1**, 0071 (2017).

238. Pandey, K. C. L. A. R. Stability and electronic properties of atomistically-engineered 2D boron sheets. *J. Phys. Chem. C* **111**, 2906–2912 (2007).

239. Penev, E. S., Bhowmick, S., Sadrzadeh, A. & Yakobson, B. I. Polymorphism of two-dimensional boron. *Nano Lett.* **12**, 2441–2445 (2012).

240. Xiaojun, W. et al. Two-dimensional boron monolayer sheets. *ACS Nano* **6**, 7443–7453 (2012).

241. Liu, H., Gao, J. & Zhao, J. From boron cluster to two-dimensional boron sheet on Cu(111) surface: growth mechanism and hole formation. *Sci. Rep.* **3**, 3238 (2013).

242. Zhou, X.-F. et al. Semimetallic two-dimensional boron allotrope with massless dirac fermions. *Phys. Rev. Lett.* **112**, 085502 (2014).

243. Mannix, A. J. et al. Synthesis of borophenes: anisotropic, two-dimensional boron polymorphs. *Science* **350**, 1513–1516 (2015).

244. Feng, B. et al. Experimental realization of two-dimensional boron sheets. *Nat. Chem.* **8**, 563–568 (2016).

245. Zhang, Z. et al. Substrate-induced nanoscale undulations of borophene on silver. *Nano Lett.* **16**, 6622–6627 (2016).

246. Wu, R. et al. Large-area single-crystal sheets of borophene on Cu(111) surfaces. *Nat. Nanotechnol.* **14**, 44–49 (2019).

247. Li, W. et al. Experimental realization of honeycomb borophene. *Sci. Bull.* **63**, 282–286 (2018).

248. Kiraly, B. et al. Borophene synthesis on Au(111). *ACS Nano* **13**, 3816–3822 (2019).

249. Omambac, K. M. et al. Segregation-enhanced epitaxy of borophene on Ir(111) by thermal decomposition of borazine. *ACS Nano* **15**, 7421–7429 (2021).

250. Showkat, H. Mir et al. Two-dimensional boron: lightest catalyst for hydrogen and oxygen evolution reaction. *Appl. Phys. Lett.* **109**, 053903 (2016).

251. Ling, C., Shi, L., Ouyang, Y., Zeng, X. C. & Wang, J. Nanosheet supported single-metal atom bifunctional catalyst for overall water splitting. *Nano Lett.* **17**, 5133–5139 (2017).

252. Zhu, C. Y. et al. Elongated heterometal double-sites promote nitrogen reduction on two-dimensional MM′ B₇ monolayers. *J. Mater. Chem. A* **9**, 10855–10868 (2021).

253. Zhu, C. Y. et al. Effective CO migration among multiabsorbed sites achieves the low-barrier and high-selective conversion to C₂ products on the Ni₂B₅ monolayer. *ACS Appl. Mater. Inter.* **13**, 3845–3855 (2021).

254. Liu, C. et al. Two-dimensional boron sheets as metal-free catalysts for hydrogen evolution reaction. *J. Phys. Chem. C* **122**, 19051–19055 (2018).

255. Shi, L., Ling, C., Ouyang, Y. & Wang, J. High intrinsic catalytic activity of two-dimensional boron monolayers for the hydrogen evolution reaction. *Nanoscale* **9**, 533–537 (2017).

256. Liu, C. et al. Theoretical evaluation of possible 2D boron monolayer in N₂ electrochemical conversion into ammonia. *J. Phys. Chem. C* **122**, 25268–25273 (2018).

257. Qin, G., Cui, Q., Du, A. & Sun, Q. Borophene: a metal-free and metallic electro-catalyst for efficient converting CO₂ into CH₄. *ChemCatChem* **12**, 1483–1490 (2020).

258. Qiu, W. et al. High-performance artificial nitrogen fixation at ambient conditions using a metal-free electrocatalyst. *Nat. Commun.* **9**, 3485 (2018).

259. Fan, Q. et al. High-yield production of few-layer boron nanosheets for efficient electrocatalytic N₂ reduction. *Chem. Commun.* **55**, 4246–4249 (2019).

260. Zhang, X. et al. Boron nanosheet: an elemental two-dimensional (2D) material for ambient electrocatalytic N₂ to CH₃ fixation in neutral media. *ACS Catal.* **9**, 4609–4615 (2019).

261. Jiang, Q. et al. The importance of atomic charge distributions of solid boron material in N₂ electrochemical reduction. *Appl. Surf. Sci.* **526**, 146606 (2020).

262. Uosaki, K. et al. Boron nitride nanosheet on gold as an electrocatalyst for oxygen reduction reaction: theoretical suggestion and experimental proof. *J. Am. Chem. Soc.* **136**, 6542–6545 (2014).

263. Koitz, R., Nørskov, J. K. & Studt, F. A systematic study of metal-supported boron nitride materials for the oxygen reduction reaction. *Phys. Chem. Chem. Phys.* **17**, 12722–12727 (2015).

264. Pakdel, A., Zhi, C. Y., Bando, Y. & Golberg, D. Low-dimensional boron nitride nanomaterials. *Mater. Today* **15**, 256–265 (2012).

265. Golberg, D. et al. Boron nitride nanotubes and nanosheets. *ACS Nano* **4**, 2979–2993 (2010).

266. Pham, T. et al. A universal wet-chemistry route to metal filling of boron nitride nanotubes. *Nano Lett.* **16**, 320–325 (2016).

267. Nautiyal, P., Gupta, A., Seal, S., Boesl, B. & Agarwal, A. Reactive wetting and filling of boron nitride nanotubes by molten aluminum during equilibrium solidification. *Acta Mater.* **126**, 124–131 (2017).

268. Zhou, S. et al. Boron nitride nanotubes for ammonia synthesis: activation by filling transition metals. *J. Am. Chem. Soc.* **142**, 308–317 (2020).

269. Yang, X., Zhou, S., Huang, S. & Zhao, J. Metal-encapsulated boron nitride nanocages for solar-driven nitrogen fixation. *J. Phys. Chem. C.* **124**, 23798–23806 (2020).

270. Zhang, Y. et al. Hexagonal boron nitride nanosheet for effective ambient N_2 fixation to NH_3. *Nano Res.* **12**, 919–924 (2019).

271. Zhao, J. et al. High-performance N_2-to-NH_3 fixation by a metal-free electrocatalyst. *Nanoscale* **11**, 4231–4235 (2019).

272. Liu, Z. et al. Defective carbon-doped boron nitride nanosheets for highly efficient electrocatalytic conversion of N_2 to NH_3. *ACS Sustain. Chem. Eng.* **8**, 5278–5286 (2020).

273. Lee, J. & Kang, J. Metal-free N_2-to-NH_3 thermal conversion at the boron-terminated zigzag edges of hexagonal boron nitride: mechanism and kinetics. *J. Catal.* **375**, 68–73 (2019).

274. Mao, X., Zhou, S., Yan, C., Zhu, Z. & Du, A. A single boron atom doped boron nitride edge as a metal-free catalyst for N_2 fixation. *Phys. Chem. Chem. Phys.* **21**, 1110–1116 (2019).

275. Chen, Z., Zhao, J., Yin, L. & Chen, Z. B-terminated (111) polar surfaces of BP and BAs: promising metal-free electrocatalysts with large reaction regions for nitrogen fixation. *J. Mater. Chem. A* **7**, 13284–13292 (2019).

276. Mou, S. et al. Boron phosphide nanoparticles: a nonmetal catalyst for high-selectivity electrochemical reduction of CO_2 to CH_3OH. *Adv. Mater.* **31**, 1903499 (2019).

277. Liu, S. et al. Facilitating nitrogen accessibility to boron-rich covalent organic frameworks via electrochemical excitation for efficient nitrogen fixation. *Nat. Commun.* **10**, 3898 (2019).

278. Chang, B. et al. Metal-free boron carbonitride with tunable boron Lewis acid sites for enhanced nitrogen electroreduction to ammonia. *Appl. Catal. B: Environ.* **283**, 119622 (2021).

279. Carenco, S., Portehault, D., Boissiere, C., Mezailles, N. & Sanchez, C. Nanoscaled metal borides and phosphides: recent developments and perspectives. *Chem. Rev.* **113**, 7981–8065 (2013).

280. Jothi, P. R., Yubuta, K. & Fokwa, B. P. T. A simple, general synthetic route toward nanoscale transition metal borides. *Adv. Mater.* **30**, 1704181 (2018).

281. Gupta, S., Patel, M. K., Miotello, A. & Patel, N. Metal boride-based catalysts for electrochemical water-splitting: a review. *Adv. Funct. Mater.* **30**, 1906481 (2020).

282. Li, Q., Cheng, Y., Li, X., Guo, Y. & Chu, K. ZrB_2 as an earth-abundant metal diboride catalyst for electroreduction of dinitrogen to ammonia. *Chem. Commun.* **56**, 13009–13012 (2020).

283. Wang, Y. et al. Tuning morphology and electronic structure of amorphous NiFeB nanosheets for enhanced electrocatalytic N_2 reduction. *ACS Appl. Energy Mater.* **3**, 9516–9522 (2020).

284. Park, H., Encinas, A., Scheifers, J. P., Zhang, Y. & Fokwa, B. P. T. Boron-dependency of molybdenum boride electrocatalysts for the hydrogen evolution reaction. *Angew. Chem. Int. Ed.* **56**, 5575–5578 (2017).

285. Zhang, R. et al. Electroless plating of transition metal boride with high boron content as superior her electrocatalyst. *ChemCatChem* **12**, 3068–3075 (2020).

286. Liu, X., Jiao, Y., Zheng, Y. & Qiao, S.-Z. Isolated boron sites for electroreduction of dinitrogen to ammonia. *ACS Catal.* **10**, 1847–1854 (2020).

287. Qin, G., Cui, Q., Du, A., Wang, W. & Sun, Q. Transition metal diborides: a new type of high-performance electrocatalysts for nitrogen reduction. *ChemCatChem* **11**, 2624–2633 (2019).

288. Chu, K. et al. Amorphization activated FeB_2 porous nanosheets enable efficient electrocatalytic N_2 fixation. *J. Energy Chem.* **53**, 82–89 (2021).

289. Kota, S., Sokol, M. & Barsoum, M. W. A progress report on the MAB phases: atomically laminated, ternary transition metal borides. *Int. Mater. Rev.* **65**, 226–255 (2019).

290. Yang, X., Shang, C., Zhou, S. & Zhao, J. MBenes: emerging 2D materials as efficient electrocatalysts for the nitrogen reduction reaction. *Nanoscale Horiz.* **5**, 1106–1115 (2020).

291. Guo, X. et al. Establishing a theoretical landscape for identifying basal plane active 2D metal borides (MBenes) toward nitrogen electroreduction. *Adv. Funct. Mater.* **31**, 2008056 (2020).

292. Zhao, H. & Yuan, Z. Y. Insights into transition metal phosphate materials for efficient electrocatalysis. *ChemCatChem* **12**, 3797–3810 (2020).

293. Shi, Y., Pan, B. W., Yu, J. S., Zhou, Y. & Zhou, J. Recent advances in applying carbonyl-stabilized phosphorus ylides for catalysis. *ChemCatChem* **13**, 129–139 (2021).

294. Yan, J. Q., Verma, P., Kuwahara, Y., Mori, K. & Yamashita, H. Recent progress on black phosphorus-based materials for photocatalytic water splitting. *Small Methods* **2**, 1800212 (2018).

295. Liu, W. et al. A highly active and stable hydrogen evolution catalyst based on pyrite-structured cobalt phosphosulfide. *Nat. Commun.* **7**, 10771 (2016).

296. Cabán-Acevedo, M. et al. Efficient hydrogen evolution catalysis using ternary pyrite-type cobalt phosphosulphide. *Nat. Mater.* **14**, 1245–1251 (2015).

297. Zheng, Y.-R. et al. Doping-induced structural phase transition in cobalt dis-elenide enables enhanced hydrogen evolution catalysis. *Nat. Commun.* **9**, 2533 (2018).

298. Sa, B., Li, Y.-L., Qi, J., Ahuja, R. & Sun, Z. Strain engineering for phosphorene: the potential application as a photocatalyst. *J. Phys. Chem. C.* **118**, 26560–26568 (2014).

299. Hu, W., Lin, L., Yang, C., Dai, J. & Yang, J. Edge-modified phosphorene nanoflake heterojunctions as highly efficient solar cells. *Nano Lett.* **16**, 1675–1682 (2016).

300. Zhou, S., Liu, N. & Zhao, J. Phosphorus quantum dots as visible-light photocatalyst for water splitting. *Comput. Mater. Sci.* **130**, 56–63 (2017).

301. Arra, S., Ramya, K. R., Babar, R. & Kabir, M. Photocatalytic activity of phosphorene derivatives: coverage, electronic, optical, and excitonic properties. *J. Phys. Chem. C.* **122**, 7194–7202 (2018).

302. Yang, X. et al. Enhanced photocatalytic performance of black phosphorene by isoelectronic co-dopants. *Inorg. Chem. Front.* **6**, 2369–2378 (2019).

303. Zhu, X. et al. Black phosphorus revisited: a missing metal-free elemental photocatalyst for visible light hydrogen evolution. *Adv. Mater.* **29**, 1605776 (2017).

304. Liu, D. et al. Photoelectrochemical synthesis of ammonia with black phosphorus. *Adv. Funct. Mater.* **30**, 2002731 (2020).

305. Tian, B. et al. Facile bottom-up synthesis of partially oxidized black phosphorus nanosheets as metal-free photocatalyst for hydrogen evolution. *Proc. Natl Acad. Sci. USA* **115**, 4345–4350 (2018).

306. Bian, S. et al. Edge-rich black phosphorus for photocatalytic nitrogen fixation. *J. Phys. Chem. Lett.* **11**, 1052–1058 (2020).

307. Ran, J., Zhu, B. & Qiao, S. Z. Phosphorene co-catalyst advancing highly efficient visible-light photocatalytic hydrogen production. *Angew. Chem. Int. Ed.* **56**, 10373–10377 (2017).

308. Tian, B. et al. Supported black phosphorus nanosheets as hydrogen-evolving photocatalyst achieving 5.4% energy conversion efficiency at 353 K. *Nat. Commun.* **9**, 1397 (2018).

309. Kong, L. et al. g-C_3N_4 loading black phosphorus quantum dot for efficient and stable photocatalytic H_2 generation under visible light. *Adv. Funct. Mater.* **28**, 1800668 (2018).

310. Shen, Z.-K. et al. Few-layer black phosphorus nanosheets: a metal-free cocatalyst for photocatalytic nitrogen fixation. *ACS Appl. Mater. Inter.* **12**, 17343–17352 (2020).

311. Jiang, Q. et al. Facile synthesis of black phosphorus: an efficient electrocatalyst for the oxygen evolving reaction. *Angew. Chem. Int. Ed.* **128**, 14053–14057 (2016).

312. Ren, X. et al. Few-layer black phosphorus nanosheets as electrocatalysts for highly efficient oxygen evolution reaction. *Adv. Energy Mater.* **7**, 1700396 (2017).

313. Prasannachandran, R., Vineesh, T. V., Anil, A., Krishna, B. M. & Shaijumon, M. M. Functionalized phosphorene quantum dots as efficient electrocatalyst for oxygen evolution reaction. *ACS Nano* **12**, 11511–11519 (2018).

314. Cai, Y. et al. Design of phosphorene for hydrogen evolution performance comparable to platinum. *Chem. Mater.* **31**, 8948–8956 (2019).

315. Xue, X.-X. et al. Tuning the catalytic property of phosphorene for oxygen evolution and reduction reactions by changing oxidation degree. *J. Phys. Chem. Lett.* **10**, 3440–3446 (2019).

316. He, R. et al. Molybdenum disulfide–black phosphorus hybrid nanosheets as a superior catalyst for electrochemical hydrogen evolution. *Nano Lett.* **17**, 4311–4316 (2017).

317. Zhu, X.-D., Xie, Y. & Liu, Y.-T. Exploring the synergy of 2D MXene-supported black phosphorus quantum dots in hydrogen and oxygen evolution reactions. *J. Mater. Chem. A* **6**, 21255–21260 (2018).

318. Yuan, Z. et al. Ultrathin black phosphorus-on-nitrogen doped graphene for efficient overall water splitting: dual modulation roles of directional interfacial charge transfer. *J. Am. Chem. Soc.* **141**, 4972–4979 (2019).

319. Zhang, L., Ding, L. X., Chen, G. F., Yang, X. & Wang, H. Ammonia synthesis under ambient conditions: selective electroreduction of dinitrogen to ammonia on black phosphorus nanosheets. *Angew. Chem. Int. Ed.* **58**, 2612–2616 (2019).

320. Pei, W., Zhou, S., Zhao, J., Du, Y. & Dou, S. X. Optimization of photocarrier dynamics and activity in phosphorene with intrinsic defects for nitrogen fixation. *J. Mater. Chem. A* **8**, 20570–20580 (2020).

321. Zheng, Q. et al. Ab initio nonadiabatic molecular dynamics investigations on the excited carriers in condensed matter systems. *WIRES Comput. Mol. Sci.* **9**, e1411 (2019).

322. Zhang, Y. & Song, L. Structural designs and in-situ X-ray characterizations of metal phosphides for electrocatalysis. *ChemCatChem* **12**, 3621–3638 (2020).

323. McEnaney, J. M. et al. Amorphous molybdenum phosphide nanoparticles for electrocatalytic hydrogen evolution. *Chem. Mater.* **26**, 4826–4831 (2014).

324. Xiao, P. et al. Molybdenum phosphide as an efficient electrocatalyst for the hydrogen evolution reaction. *Energy Environ. Sci.* **7**, 2624–2629 (2014).

325. Kibsgaard, J. & Jaramillo, T. F. Molybdenum phosphosulfide: an active, acid-stable, earth-abundant catalyst for the hydrogen evolution reaction. *Angew. Chem. Int. Ed.* **53**, 14433–14437 (2014).

326. Pu, Z., Amiinu, I. S., Wang, M., Yang, Y. & Mu, S. Semimetallic MoP_2: an active and stable hydrogen evolution electrocatalyst over the whole pH range. *Nanoscale* **8**, 8500–8504 (2016).

327. Wu, T., Pi, M., Zhang, D. & Chen, S. Three-dimensional porous structural MoP_2 nanoparticles as a novel and superior catalyst for electrochemical hydrogen evolution. *J. Power Sources* **328**, 551–557 (2016).

328. Popczun, E. J. et al. Nanostructured nickel phosphide as an electrocatalyst for the hydrogen evolution reaction. *J. Am. Chem. Soc.* **135**, 9267–9270 (2013).

329. Jiang, P., Liu, Q. & Sun, X. NiP_2 nanosheet arrays supported on carbon cloth: an efficient 3D hydrogen evolution cathode in both acidic and alkaline solutions. *Nanoscale* **6**, 13440–13445 (2014).

330. Liu, T. et al. Interfacial electron transfer of $Ni_2P–NiP_2$ polymorphs inducing enhanced electrochemical properties. *Adv. Mater.* **30**, 1803590 (2018).

331. Laursen, A. B. et al. Climbing the volcano of electrocatalytic activity while avoiding catalyst corrosion: Ni3P, a hydrogen evolution electrocatalyst stable in both acid and alkali. *ACS Catal.* **8**, 4408–4419 (2018).

332. Chen, W. et al. Nickel phosphide based hydrogen producing catalyst with low overpotential and stability at high current density. *Electrochim. Acta* **299**, 756–761 (2019).

333. Popczun, E. J., Read, C. G., Roske, C. W., Lewis, N. S. & Schaak, R. E. Highly active electrocatalysis of the hydrogen evolution reaction by cobalt phosphide nanoparticles. *Angew. Chem. Int. Ed.* **126**, 5531–5534 (2014).

334. Callejas, J. F. et al. Electrocatalytic and photocatalytic hydrogen production from acidic and neutral-pH aqueous solutions using iron phosphide nanoparticles. *ACS Nano* **8**, 11101–11107 (2014).

335. Huang, Z. et al. Cobalt phosphide nanorods as an efficient electrocatalyst for the hydrogen evolution reaction. *Nano Energy* **9**, 373–382 (2014).

336. Ge, Y. et al. Transforming nickel hydroxide into 3D prussian blue analogue array to obtain Ni_2P/Fe_2P for efficient hydrogen evolution reaction. *Adv. Energy Mater.* **8**, 1800484 (2018).

337. Li, J. et al. Mechanistic insights on ternary $Ni_{2−x}Co_xP$ for hydrogen evolution and their hybrids with graphene as highly efficient and robust catalysts for overall water splitting. *Adv. Funct. Mater.* **26**, 6785–6796 (2016).

338. Liang, H. et al. Plasma-assisted synthesis of NiCoP for efficient overall water splitting. *Nano Lett.* **16**, 7718–7725 (2016).

339. Tang, C. et al. Ternary $Fe_xCo_{1−x}P$ nanowire array as a robust hydrogen evolution reaction electrocatalyst with Pt-like activity: experimental and theoretical insight. *Nano Lett.* **16**, 6617–6621 (2016).

340. Chen, J. et al. Co-Fe-P nanotubes electrocatalysts derived from metal-organic frameworks for efficient hydrogen evolution reaction under wide pH range. *Nano Energy* **56**, 225–233 (2019).

341. Kibsgaard, J. et al. Designing an improved transition metal phosphide catalyst for hydrogen evolution using experimental and theoretical trends. *Energy Environ. Sci.* **8**, 3022–3029 (2015).

342. Wexler, R. B., Martirez, J. M. P. & Rappe, A. M. Active role of phosphorus in the hydrogen evolving activity of nickel phosphide (0001) surfaces. *ACS Catal.* **7**, 7718–7725 (2017).

343. Jin, Z. et al. Three-dimensional amorphous tungsten-doped nickel phosphide microsphere as an efficient electrocatalyst for hydrogen evolution. *J. Mater. Chem. A* **2**, 18593–18599 (2014).

344. Zhang, Y. et al. A Mn-doped Ni_2P nanosheet array: an efficient and durable hydrogen evolution reaction electrocatalyst in alkaline media. *Chem. Commun.* **53**, 11048–11051 (2017).

345. Wang, P. et al. Iron-doped nickel phosphide nanosheet arrays: an efficient bifunctional electrocatalyst for water splitting. *ACS Appl. Mater. Inter.* **9**, 26001–26007 (2017).

346. Li, Y. et al. 3D self-supported Fe-doped Ni_2P nanosheet arrays as bifunctional catalysts for overall water splitting. *Adv. Funct. Mater.* **27**, 1702513 (2017).

347. Partanen, L., Hakala, M. & Laasonen, K. Hydrogen adsorption trends on various metal-doped Ni_2P surfaces for optimal catalyst design. *Phys. Chem. Chem. Phys.* **21**, 184–191 (2019).

348. Duan, H. et al. High-performance Rh_2P electrocatalyst for efficient water splitting. *J. Am. Chem. Soc.* **139**, 5494–5502 (2017).

349. Wang, T.-W., Wang, T.-L., Chou, W.-J., Wu, L.-F. & Lin, S.-H. First-principles investigation of the hydrogen evolution reaction of transition metal phosphides CrP, MnP, FeP, CoP, and NiP. *Phys. Chem. Chem. Phys.* **23**, 2305–2312 (2021).

350. Wang, P., Fu, G. & Wan, H. How high valence transition metal spreads its activity over nonmetal oxoes: a proof-of-concept study. *ACS Catal.* **7**, 5544–5548 (2017).

351. Laursen, A. B. et al. Climbing the volcano of electrocatalytic activity while avoiding catalyst corrosion: Ni3P, a hydrogen evolution electrocatalyst stable in both acid and alkali. *ACS Catal.* **8**, 4408–4419 (2018).

ACKNOWLEDGEMENTS

AUTHOR CONTRIBUTIONS

S.Z. and J.Z. proposed the outline of the review. S.Z. wrote the manuscript. W.P., Y.Z., N.L., and X.Y. wrote the sections "Carbon-based catalysts", "Silicon-based catalysts", "Oxide-based catalysts", and "Boron-based catalysts" of the manuscript, respectively. J.Z. revised and commented on the manuscript.

COMPETING INTERESTS

The authors declare no competing interests.

ADDITIONAL INFORMATION

Correspondence and requests for materials should be addressed to Jijun Zhao.

Reprints and permission information is available at http://www.nature.com/reprints

Publisher's note Springer Nature remains neutral with regard to jurisdictional claims in published maps and institutional affiliations.